

Aspects of information processing by individual neurons and populations of neurons

vorgelegt von
Diplom Informatiker
Thomas Hoch

Von der Fakultät IV - Elektrotechnik und Informatik
der Technischen Universität Berlin
zur Erlangung des akademischen Grades
Doktor der Naturwissenschaften
Dr. rer. nat.

genehmigte Dissertation

Promotionsausschuss:

Vorsitzender: Prof. Dr. Klaus-Robert Müller
Berichter: Prof. Dr. Klaus Obermayer
Berichter: Prof. Dr. Manfred Opper
Berichter: PD Dr. Maxim Volgushev

Tag der wissenschaftlichen Aussprache: 16.4.2007

Berlin 2007

D 83

(C) Thomas Hoch
Berlin, April 2007

Acknowledgment ¹

First of all, I would like to thank Prof. Klaus Obermayer for giving me the opportunity to work in his excellent research group at the Berlin University of Technology. His guidance helped me to learn how to approach a problem scientifically. Without his support and advice this work would never have been completed.

Furthermore, I would like to thank Dr. Maxim Volgushev, with whom I enjoyed a very fruitful collaboration. The focused scientific discussions with him were inspiring and contributed lots of ideas to my work.

I also like to thank my colleagues at the Neural Information Processing Group. They have been a valuable source of scientific ideas, knowledge, and perspective. In particular I would like to thank Gregor Wenning, who introduced me into the field of computational neuroscience, and my roommates Andre Paus and Akhil Garg for fruitful discussions and assistance.

Finally, I would like to thank my parents and Sandra Fejjeri who supported me through the years.

¹During the work on my PhD-thesis I received financial support from the DFG (SFB-618)

Zusammenfassung

Experimente an Zellen aus dem visuellen Kortex offenbarten ein stark fluktuierendes Membranpotential, das im Mittelwert deutlich erhöht war. Eine hohe Variabilität des Membranpotentials hat erhebliche Auswirkungen auf die Art und Weise, wie Informationen in Neuronen verarbeitet werden. Zum einen tragen die starken Fluktuationen zu einer schnellen Übertragung von Signalen bei oder erlauben überhaupt erst die Übertragung von schwachen Signalen. Zum anderen induzieren sie eine hohe Variabilität in der Antwort eines Neurons, was den Informationsgehalt einzelner Aktionspotentiale stark mindern kann. Eine zentrale Frage ist daher, wie die Verarbeitung von Signalen von der Dynamik des Membranpotentials beeinflusst wird. In dieser Dissertation werden die folgenden Aspekte untersucht:

In einer aktuellen Untersuchung fand man heraus, dass die Stärke der Fluktuationen des Membranpotentials im γ -Frequenzbereich (25-70 Hz) mit der langsamen, vom Eingangssignal induzierten Änderung des Membranpotentials gekoppelt ist. Mit Hilfe eines detaillierten Neuronenmodells, welches sorgfältig an experimentelle Daten angepasst wurde, wird in der vorliegenden Arbeit gezeigt, dass sich diese Kopplung positiv auf die Kodierungseigenschaft des Neurons auswirkt. Eine weiterführende Analyse ergab sogar, dass eine Änderung der Amplitude der Fluktuationen im γ -Bereich einen größeren Einfluss auf die Güte der Kodierung hat, als eine vergleichbare Änderung in der Stimulusamplitude. Dies bedeutet, dass die Modulation der Stärke der γ -Fluktuationen ein effizienter Mechanismus ist, um die Kodierung visueller Signale zu verbessern.

Des Weiteren wird untersucht, wie die Fluktuationen des Membranpotentials die Verarbeitung von schwachen Signalen beeinflussen. Aus Studien an Tieren ist bekannt, dass ein stark fluktuierendes Membranpotential meist mit einer Erhöhung des Leitwerts einhergeht, was zu einer Reduzierung der zeitlichen Korrelation führt. Es stellt sich somit die Frage, inwieweit die Güte der Detektion von synchroner Aktivität von der zeitlichen Korrelation des Membranpotentials abhängt. Die hier durchgeführte systematische Untersuchung ergab, dass für viele Kombinationen von Mittelwert und Standardabweichung des Membranpotentials eine Reduzierung der zeitlichen Korrelation zu einer besseren Detektion führt.

Ein weiterer Aspekt, der in dieser Arbeit behandelt wird, befasst sich mit den Kosten der Informationsübertragung. Die Erzeugung von Aktionspotentialen ist energetisch sehr aufwändig und es ist sehr wahrscheinlich, dass im Gehirn Strategien angewandt

werden, die die Kosten der Übertragung verringern. Interessanterweise konnte gezeigt werden, dass eine optimale Informationsübertragung bei Berücksichtigung der Kosten schwache Signale und ein fluktuierendes Membranpotential voraussetzt. Die gemessene Variabilität in der Antwort von Neuronen könnte somit eine Signatur effizienter Informationsverarbeitung sein.

Eine weitere Konsequenz der hohen Irregularität neuronaler Antworten ist, dass Information vermutlich von Gruppen von Neuronen verarbeitet wird. Um festzustellen, wie viel Information durch so ein Ensemble repräsentiert wird, eignet sich z.B. das Summieren der Einzelaktivitäten als Auslesemechanismus. Wenn man nun aber die Information einer solchen aufsummierten Antwort bestimmen möchte, dann zeigt sich, dass lineare Methoden für Signale, die einen starken niederfrequenten Anteil haben, den Informationsgehalt zu niedrig schätzen. Da solche Signale oft bei Experimenten eingesetzt werden, sollten daher nicht-lineare Methoden, wie z.B. Neuronale Netzwerke, für die Bestimmung des Informationsgehaltes bevorzugt werden.

Summary

Visual stimulation often leads in neurons of the visual cortex to a strongly fluctuating membrane potential, which on average is close to the threshold (Pare et al., 1998; Anderson et al., 2000). The consequences of such a fluctuating membrane potential for the processing of weak input signals in cortical neurons are not well understood yet. In this thesis we, therefore, investigate how the encoding of visual signals depends on the statistical properties of the membrane potential fluctuations.

Recently, it has been shown that increased amplitudes of membrane potential fluctuations in the γ -frequency range (25 – 70 Hz) are coupled to the depolarizing peaks of the stimulus-induced, low frequency changes of the membrane potential (Volgushev et al., 2003), and they suggested that this coupling may improve stimulus encoding. Using a single compartment conductance-based neuron model we show that modulation of the γ -range membrane potential fluctuations in phase with the slow membrane depolarization greatly improves stimulus encoding. Moreover, we find that the alteration of modulated γ -activity within the range typically observed in visual cells, leads to a variation in stimulus encoding, which was stronger than corresponding changes of the amplitude of the low frequency signal. Thus, the modulation of the γ -activity is an efficient mechanism to improve the encoding precision of the temporal characteristics of visual signals.

We also investigate the processing of sub-threshold signals in the high noise regime. We show that besides the mean and the standard deviation of the membrane potential, its temporal correlation is an important factor that modulates the detection of synchronous activity. Using a neural population we show that for most combinations of mean and standard deviation of the membrane potential detection performance could be improved by a faster changing membrane potential. Furthermore, we investigate metabolic aspects of information processing. We show that optimal information transmission favors sub-threshold input distributions, if quality of information transmission is traded against its metabolic costs, which indicates that information is likely to be coded using low firing rates and populations of cells.

Finally, we compare a linear with a nonlinear decoder (e.g. neural network) with respect to how well they estimate the information rate from pooled population responses. We find that the feed-forward neural network outperforms the linear decoder substantially, if membrane potential fluctuations are weak and if input stimuli have a strong low frequency components. Because experimentally used stimuli often have

strong low frequency components, our results suggest the use of a nonlinear decoder for the precise quantification of the transmitted information.

Contents

1. Introduction	11
1.1. Research Goals and Outline	14
2. Neuronal Models and Analysis Methods	17
2.1. Biological Background	17
2.2. Neuronal Models	19
2.2.1. Leaky Integrate-and-Fire Neurons	20
2.2.2. The Hodgkin-Huxley Neurons	21
2.3. Synaptic Noise Models	25
2.3.1. Gaussian White Noise	25
2.3.2. Gaussian Colored Noise	26
2.3.3. Conductance Noise Model	27
2.4. Analysis Methods	28
2.4.1. Correlation Function and Spectral Density	29
2.4.2. Information Rate Estimation with Linear Filter	30
3. γ-Band Membrane Potential Fluctuations and Stimulus Encoding	33
3.1. Introduction	33
3.2. Materials and Methods	34
3.2.1. Physiology	34
3.2.2. Single Compartment Model	35
3.2.3. Estimation of the Information Rate	37
3.3. Results	37
3.3.1. Intracellular Recordings from Cat Visual Cortex Neurons	38
3.3.2. Construction and Tuning of Input Conductances	43
3.3.3. γ -Band Membrane Potential Fluctuations and Stimulus Encoding	49
3.4. Discussion	57
4. Neural Information Transmission	63
4.1. Introduction	63
4.2. Materials and Methods	64

Contents

4.3. Results	65
4.3.1. Stochastic Resonance	65
4.3.2. Energy Efficient Information Transmission	68
4.4. Discussion	70
5. Pulse Detection	73
5.1. Introduction	73
5.2. Materials and Methods	74
5.2.1. Single-compartment model	74
5.2.2. Synaptic Noise Model	75
5.2.3. Temporal Correlation of the Membrane Potential	77
5.2.4. Pulse Detection Scenario	79
5.3. Results	79
5.3.1. Effect of the Synaptic Time Constants	83
5.3.2. Effect of the Shape of the Postsynaptic Potential	85
5.3.3. Effect of the Synaptic Conductance	90
5.4. Discussion	91
6. Information Rate Estimation	95
6.1. Introduction	95
6.2. Materials and Methods	96
6.2.1. Population of Leaky Integrate-and-Fire Neurons	96
6.2.2. Population of Hodgkin-Huxley Neurons	97
6.2.3. Estimation of the Information Rate	99
6.3. Results	105
6.3.1. The Single LIF Neuron	105
6.3.2. Population of LIF Neurons	108
6.3.3. Population of Hodgkin-Huxley Neurons	117
6.4. Discussion	118
A. The Hodgkin Huxley Neuron	121
B. Two-state kinetic synapse model	125
C. Adjustment of synaptic background activity	126
References	131

1. Introduction

The nervous system of all higher animals consists of an enormous number of neurons, which are highly connected to each other via synapses. According to Abeles (1991), each cortical neuron receives about 40 000 synapses, where half of the synapses originate from local neurons and the other half from neurons of other brain regions. On top of this high complexity, the signal processing of neurons is highly nonlinear. One example of this is the generation of an action potential. Input signals, not strong enough to drive the membrane potential above a threshold value evoke no response. Slightly stronger signals, however, may generate a train of action potentials of high frequency. It is the combination of this high complexity and the nonlinearity of the brain, which makes the investigation of neural dynamics difficult but challenging. In this thesis we present original research, which may contribute to the understanding of nonlinear dynamics of neural information processing.

An apparent signature of cortical neurons is the high variability of their spiking activity (Softky and Koch, 1993; Stevens and Zador, 1998; Shadlen and Newsome, 1998). It is widely accepted that the irregularity in the neural response arises from strong fluctuations of the membrane potential. Figure 1.1 shows an example trace of the intracellular recorded membrane potential of a cell from cat visual cortex during the presentation of a stimulus. Apart from the strong stimulus driven modulation of the membrane potential, the recording also shows a high variability of the membrane potential around its average value. Recent experimental findings have demonstrated that cells from cat visual cortex show a strongly fluctuating membrane potential even in the absence of a stimulus due to high background activity (Paré et al., 1998; Destexhe and Paré, 1999).

The membrane potential fluctuations arise mainly from synaptic events. Given the high number of synapses a neuron receives and the high spontaneous firing rates of cortical cells (Steriade et al., 2001), the number of impinging synaptic events during an interval in the order of the neurons membrane time constant is enormous. Due to the high irregularity in the neural response, however, the presynaptic activity may change on a short time scale leading to a strongly fluctuating membrane potential. Another source, contributing to the membrane potential variability, arises from the

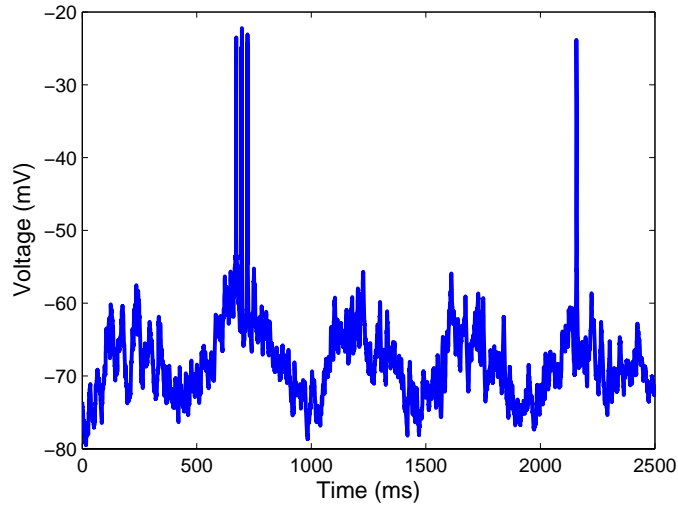


Figure 1.1.: Membrane potential trace of a cell from cat visual cortex during the presentation of a moving grating. The data was generously provided by Dr. Maxim Volgushev.

further processing of the visual signal. It is well known that the generation of a postsynaptic potential is itself a random process (Koch, 1998). An incoming spike does not necessarily lead to a postsynaptic potential, and the release probability at an individual synapse can be highly variable. Besides the synaptic input variability and the probabilistic nature of synaptic transmission, another well recognized source of variability in cortical cells arises from the stochastically opening and closing of the different ion channels (White et al. 2000; Diba et al., 2004). However, it was pointed out that the above mentioned noise sources are not sufficient to explain the high variability of the membrane potential observed *in vivo* (Destexhe and Paré, 1999; Harsch and Robinson, 2000). Natural levels of membrane potential variability could only be achieved if there is substantial synchrony in the synaptic input (Stevens and Zador, 1998). Taken together, visual stimulation evokes correlated presynaptic activity leading to a strongly fluctuating membrane potential, which determines the precision of the encoding of the visual signal.

It is often assumed that the primary function of a neuron is the processing of external events. Cortical cells, however, are also subject to a considerable amount of ongoing synaptic activity, which can also change remarkably during periods of sustained attention (Steinmetz et al., 2000). The level of synaptic (background) activity can dramatically alter the response behavior of a neuron (Destexhe and Paré, 1999). For

instance, the conductance increase due to a higher level of background activity leads to smaller membrane potential fluctuations because of shunting on the one hand, and to a faster changing membrane potential due to a reduction of the membrane time constant on the other (Kuhn et al., 2004). Hence, the statistical properties of the membrane potential fluctuations depend on the actual level of background activity.

To what extent the fluctuations of the membrane potential might be considered unwanted noise, which may reduce the information processing capabilities of a neuron, or play an important role in neural information processing, remains an open question. Since cortical cells respond irregularly and with low firing rates, information is likely coded using populations of cell (Pouget et al., 2000; Averbeck and Lee, 2004). Representing a signal by a population has the advantage that a large part of the variability seen in the cortex could be averaged away as long as the responses of the neurons are only weakly correlated (Zohary et al., 1994). For example, Panzeri et al. (2003) have shown that pooling the responses of neurons in the rat barrel cortex is an efficient strategy for decoding stimulus location. On the other hand it was pointed out that neurons within a population may receive a large part of common synaptic input, which likely limits the fidelity of the stimulus representation because of synchronous firing (Shadlen and Newsome, 1998; Mazurek and Shadlen, 2002). However, using a population of 100 neurons sharing a large fraction of common input, Shadlen and Newsome (1998) have shown that such an ensemble of neurons is able to represent a stimulus by their time-dependent firing rates well. Such an encoding strategy is commonly referred to as a population rate code.

An opposite view on information encoding regards the irregularity of spike trains as a signature of a highly sophisticated code, where the exact timing of a spike conveys important information. For instance, it has been shown in the somatosensory cortex that the relative timing of the first spike provides information about the direction of fingertip force (Johansson and Birznieks, 2004), and that in the primary visual cortex the contrast-related information is encoded in the temporal structure of the neural response (Reich et al., 2001). Moreover, it has been found that highly synchronized inputs are able to produce precisely timed action potentials (Mainen and Sejnowsky; 1995, Nowak et al., 1997) since the spike generating mechanism itself is a remarkably reliable process (Mainen and Sejnowsky; 1995). Given proper synaptic delays, the precise spike timing might evoke strong excitation in the postsynaptic neuron allowing for a reliable information transmission to higher brain areas, as for example in a synfire chain (Abeles, 1991; Diesmann et al., 1999). Indeed, synchronous activity has been found in many regions of the brain (Lampl et al., 1999; Usrey and Reid, 1999) and it remains an open question as to what extent neural spiking variability is a signature of noise or plays an important role in information processing, which we do not understand

yet (Stein et al., 2005).

The fundamental principle by which the brain processes information about a stimulus is still unknown. Recent experimental and theoretical studies have shown ways how noise may facilitate information processing in neural systems. For instance, it has been shown that noise improves the speed with which a population responds to transient inputs (Tsodyks and Sejnowsky, 1995; Silberberg et al., 2004), modulates the responsiveness (gain) of cortical neurons to a driving input current (Chance et al., 2002; Fellous et al., 2003), or even allows for a transmission of weak (subthreshold) signals, as for example in a stochastic resonance setting (Bulsara et al., 1991; Douglass et al., 1993; Longtin, 1993; Wiesenfeld and Moss, 1995; Russell et al., 1999). Although the use of weak signals in a noisy environment seems disadvantageous at first glance, the transmission of weak signals over many parallel channels may use up less energy than the use of a few high intensity ones (Laughlin et al., 1998). Since information processing in the brain is costly in metabolic terms (Attwell and Laughlin, 2001; Lennie 2003), information transmission might be constrained by energy consumption leading to energy efficient codes (Levy and Baxter, 1996; Laughlin et al., 1998; Balasubramanian et al., 2001; de Polavieja, 2002).

1.1. Research Goals and Outline

A principal goal of neuroscience research is to understand how sensory stimuli are represented and processed by neural systems. An essential step in determining the information processing at population level involves the characterization of the functional role of the strong membrane potential fluctuations observed *in vivo*. In separating the membrane potential fluctuations into a stimulus related and a noise component, it is the general goal of this thesis to study the role of the noise component for the information processing capabilities of a single neuron or a neural population. We consider the following four questions:

- Can the modulation of high frequency components of the membrane potential in phase with the stimulus improve information processing in cortical cells?
- Is stochastic resonance a useful mechanism for low cost information processing?
- Is a nonlinear decoding method necessary for the precise quantification of the information rate of neural responses?
- How is the ability of a neural population to detect weak transient inputs influenced by the statistical properties of the membrane potential?

1. Introduction

The thesis is organized as follows: Chapter 2 reviews fundamental concepts of theoretical neuroscience providing the basis for the computational methods and analysis methods used throughout this thesis. Chapters 3 to 6 present the original research. Each single chapter is devoted to one of the above stated questions.

The first question is addressed in chapter 3. There we deal with the observation, that the amplitude of the membrane potential fluctuations in the γ -frequency range ($25 - 70 Hz$) is correlated with the phase of the stimulus induced slow changes of the membrane potential. Thus the question arises as to what extend this modulated γ -activity enables neurons to precisely encode visual information into spike trains. Using a Hodgkin-Huxley model neuron, which was adapted accurately to the experimental data, we find that the efficacy of transforming the stimulus induced depolarizations into trains of action potentials depends greatly on correlation between the amplitude of the γ -range fluctuations and the stimulus phase. Moreover our analysis shows that using parameters typical for *in vivo* intracellular recordings, an alteration of the strength of the modulated γ -range fluctuations is even more effective in expanding the range of encoded signals than corresponding changes of the amplitude of the low frequency signal. The work presented in this chapter is based on Hoch et al. (2006a) and was conducted in close collaboration with Maxim Volgushev at Ruhr-University Bochum, who carried out the experimental work.

In chapter 4, we investigate metabolic aspects of noise-aided information processing. Stochastic resonance is the most prominent scenario, which assigns a functional role to the otherwise unwanted noise. However, stochastic resonance was often claimed to play no significant role for neural information processing since the brain is highly adaptive, and could easily change neural properties to improve information processing beyond that of a stochastic resonance scenario (Tougaard, 2000). Energy consumption, on the other hand, has been suggested by many researchers to constrain information processing (Levy and Baxter, 1996; Laughlin et al., 1998; Balasubramanian et al., 2001; de Polavieja, 2002). Energy efficient codes favor low firing rates and subthreshold input distributions (Laughlin et al., 1998), which suggest that stochastic resonance may be a useful mechanism for low cost information transmission. Using a single leaky integrate-and-fire neuron we show that the inclusion of the metabolic cost for information transmission indeed favors subthreshold input distributions and that noise can improve information transmission. The work presented in this chapter is based on Hoch et al. (2003) and was done in collaboration with Gregor Wenning.

Chapter 5 presents a computational study of the influence of the statistical properties of the membrane potential fluctuations on the ability of a neural population to detect synchronous spiking activity. Synchronous activity has been observed throughout many regions of the brain (Lampl et al., 1999; Usrey and Reid, 1999). However,

the discrimination of the responses of a neural population to synchronous inputs from those that occurred by chance is a difficult task. We show that for a certain mean of the membrane potential, detection performance can be maximized if the variance and the temporal correlation of the membrane potential are adjusted accordingly. The work presented in this chapter was done in collaboration with Gregor Wenning and is a successive study of Wenning et al. (2005).

Finally, in chapter 6 we compare different information rate estimation techniques with respect to how well they estimate the information rate from pooled population responses. Information theory is the most rigorous way to characterize the information encoding capabilities of neural systems. Although many methods have been developed during recent years (Rieke et al., 1997; Borst and Theunissen, 1999), we show that the estimation of the information rate from time-varying responses of a population remains problematic. We find that for aperiodic Gaussian stimuli with a strong low frequency component, the widely used linear decoding method yields information rate estimates that are too low. A simple feed-forward neural network model is able to extract significantly more information from such responses. Since experimentalists often use stimuli with a strong low frequency component, our results suggest the use of nonlinear decoding methods for the quantification of the information in population responses. The work presented in this chapter is based on Hoch et al. (2006b).

2. Neuronal Models and Analysis Methods

2.1. Biological Background

Brains have evolved to process information. The primary information processing units in the brain are the neurons (or nerve cells). The human brain consists of more than 100 billion neurons, which are densely connected among each other. Typically, neurons makes 10 – 40 thousand connections to other neurons (Abeles, 1991). A neuron is composed of a dendritic tree, a cell body (soma) and an axon. In the classical view, the dendritic tree and the some receive and process the inputs from other neurons and the axon transmits the results of these computations via axon collateral's to both nearby neurons and neurons in other brain regions.

Cortical neurons show a high diversity in their morphology. Figure 2.1 shows the structure of a reconstructed layer V pyramidal cell from cat somatosensory cortex (left) and of a thalamic reticular cell from rat ventrobasal nucleus (right). The Fig. shows nicely the elaborate branching structure of dentritic trees, whose main purpose is the integration and transmission of the synaptic input to the soma. The input from other cells is received by the neuron via synapses, which are distributed with high density across the soma and the dentritic membrane surface.

The entire membrane of the neuron contains active and passive ion channels controlling the flow of ions across the membrane, and ionic pumps maintaining a gradient between the ion concentration inside and outside the cell. The difference in the ion concentration results to an electrical potential difference, which is usually referred to as the membrane potential. In the resting state, e.g. without synaptic input, the membrane potential is approximately -70 mV (resting potential). The potential outside the cell is conventionally defined to be 0 mV . The establishment of this potential difference allows neurons to generate short electric pulses, namely action potentials.

Neurons communicate with each other via action potentials. Action potentials are typically generated at the axon hillock, the region between the cell body and the axon. The generation of an action potential is an all or nothing process. Small depolarizations of the membrane potential are usually counterbalanced by the leakage current flowing

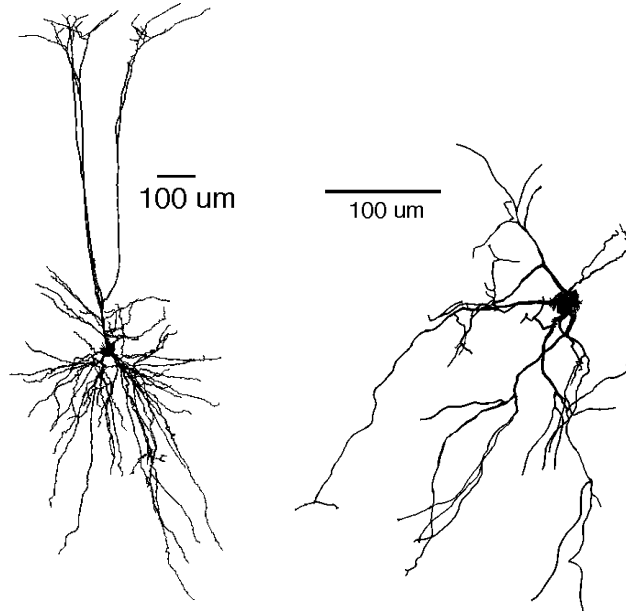


Figure 2.1.: A) Layer V pyramidal cell from cat somatosensory cortex. This cell was stained with neurobiotin (adapted from Contreras et al., 1997). B) Thalamic reticular cell, from the reticular sector of rat ventrobasal nucleus. This cell was stained with biocytin (adapted from Huguenard and Prince, 1992).

through the passive ion channels. If a depolarization raises the membrane potential above a threshold value, however, an action potential is initiated. The threshold crossing triggers the opening of sodium and potassium channels resulting to a strong sodium (inward) and a delayed potassium (outward) current. Both currents lead together to the generation of an action potential [e.g. the membrane potential is raised about $50 - 60\text{ mV}$ for a short duration ($1 - 2\text{ ms}$)].

The action potential is transmitted via the axon to the synapses where it triggers the release of neurotransmitters into the synaptic cleft (e.g. the space between the synapse and the postsynaptic side). The neurotransmitter diffuses to the membrane of the postsynaptic neuron where it binds to receptors, causing ion channels to open. Depending on the type of channel, the in- or outflux of ions lead to a depolarizing (excitatory) or a hyperpolarizing (inhibitory) postsynaptic potential (PSP).

The response behavior of a neuron is determined by its distribution of active and passive ion channels throughout the entire membrane and by its dendritic morphology (Mainen and Sejnowsky, 1996). During the past two decades, neuroscientists have spent a lot of effort characterizing the response behavior of cortical cells. Using intra- and extracellular recordings *in vivo*, the responses of neurons to depolarizing current pulses can be separated into four distinct classes (Connors and Gutnick, 1990; Gray and McCormick, 1996; Steriade, 2001). Regular spiking neurons (RS), which generate action potentials in a tonic fashion when stimulated and show spike frequency adaptation. Fast spiking neurons (FS), which are able to generate action potential of short duration and exhibit no or weak spike frequency adaptation. Chattering cells (CH), which fire periodic bursts of spikes when stimulated. And finally, intrinsic bursting cells (IB), which generate a low frequency burst through intrinsic membrane mechanism followed by a tonic train of action potentials. A prerequisite for the detailed modeling of experimental data (e.g. as for example in chapter 3) is, therefore, the proper choice of the neuronal model, which is able to reproduce the response behavior of the cell under study well. Note that the above mentioned firing patterns are representatives of a continuum of different firing properties.

2.2. Neuronal Models

Most of the findings in this thesis are based on numerical simulations of cortical cells. Until now, various neuronal models have been developed, ranging from very simple ones, which use only one single differential equation to model the membrane potential of a neuron, to complex ones, which consist of thousands of coupled differential equations. Although multi-compartment models can be efficiently simulated with open source software nowadays (e.g. with NEURON or GENESIS), it has been shown that single compartment models are able to reproduce the observed diversity of spiking behavior of cortical cells quite accurately (Wilson, 1999; Izhikevich, 2004). In this thesis we therefore concentrate on single compartment models.

As discussed above, a typical cortical cells of human cortex receives about 10^4 synapses on average (Abeles, 1991). If each synapse receives inputs at a spontaneous firing rate of 1 Hz , the number of simultaneously active synapses is high, which leads to strongly fluctuating membrane potential and a massive increase of the neurons conductance (Destexhe et al., 2003). A conductance increase of the neuron accompanied with a strongly fluctuating membrane potential was also found during visual stimulation (Borg-Graham et al., 1998; Hirsch et al., 1998, Anderson et al., 2000c). Thus, the choice of an appropriate noise model is important for the investigation of

neural information processing. Throughout this thesis we used synaptic noise models, which describe the synaptic integration of random activity at different levels of rigor. The more complex ones include the change in the membrane conductance caused by the synaptic inputs, which may turn out to be important in the context of this thesis. The different models are introduced in Sec. 2.3. But first we will shortly review two neuronal models, which are frequently used in this thesis.

2.2.1. Leaky Integrate-and-Fire Neurons

One of the oldest models is the leaky integrate-and-fire (LIF) model. Originally proposed by Lapicque (1907), the LIF is still widely used because of its simplicity. This model contains only a passive leakage term and ignores all active membrane conductances. When stimulated with a constant current, it can only generate a tonic spike train. Nevertheless, the LIF model has proven useful in many cases because it can be simulated efficiently and - in some cases - its response can be solved analytically. If simulated with an adequate model of synaptic activity, the LIF is able to reproduce some aspects of neural activity (e.g. irregularity of neuronal firing) reasonable well (Rauch et al., 2003).

The leaky integrate-and-fire (LIF) neuron is characterized by its membrane potential V , which changes in time according to the following differential equation:

$$C_m \frac{dV}{dt} = -g_L(V - E_L) + I_s, \quad (2.1)$$

where C_m is the membrane capacitance, g_L is the leak conductance, and E_L is the reversal potential. The term $g_L(V - E_L)$ represents the leakage current, which is mainly the sum of the relatively constant ion currents that maintain the ion concentration gradients. I_s is the synaptic current, which contains both the external signal as well as the synaptic background activity. Equation (2.1) describes the subthreshold dynamics of the membrane potential V . For $I_s = 0$, the membrane potential V decreases exponentially towards E_L with time constant $\tau_m = \frac{C_m}{g_L}$. For $I_s > 0$, the injected current increases the membrane potential towards the spike threshold. If I_s is strong enough, it will drive V across the spike threshold V_{th} leading to a spike event. After a spike, the membrane potential is immediately reset to V_{reset} and usually clamped to this value for an absolute refractory period of T_{ref} .

Under the assumption that the synaptic current, generated by random synaptic inputs (the background activity), can be approximated by a Wiener process and a constant bias current [cf. eq. (2.12) in Sec. 2.3], the LIF model approximates the

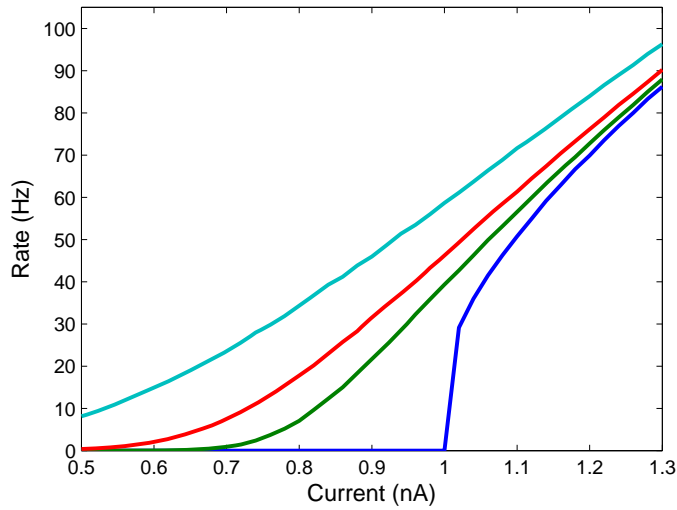


Figure 2.2.: Firing rate of the leaky integrate-and-fire neuron plotted against the bias current $\mu = \text{const}$ for different values of σ_V . Blue line: $\sigma_V = 0 \text{ mV}$ ($D = 0$); green line: $\sigma_V = 2 \text{ mV}$ ($D = 0.9$); red line: $\sigma_V = 3 \text{ mV}$ ($D = 1.34$); cyan line: $\sigma_V = 5 \text{ mV}$ ($D = 2.24$).

membrane potential of a cortical cell reasonable well (Rauch et al., 2003). Fig. 2.2 shows the firing rate of the LIF neuron plotted against the constant bias current (μ) for different noise conditions (see Fig. caption). For the noiseless case (blue line), the LIF neuron shows a highly nonlinear frequency-current (f-I) curve, and for input currents below 1 nA , the membrane potential of the neurons remains subthreshold. An increase of the noise level (because of a higher value of D) leads to a stronger fluctuating membrane potential, which occasionally generates spikes at input currents well below $\mu < 1 \text{ nA}$. Thus, for increasing values of D , the firing rate of the LIF neuron increases substantially in the subthreshold regime, which leads to an effective linearization of the f-I curve, as Fig. 2.2 indicates.

2.2.2. The Hodgkin-Huxley Neurons

The most important model in neuroscience, however, is the Hodgkin-Huxley (HH) model. Although not knowing the structure of ion channels, it was Hodgkin and Huxley (1952) who first developed a deterministic description of the action potential generating ion currents, based on measurements from the giant axon of Atlantic squid. Although their phenomenological description accounted only for the sodium and the

potassium current of the squid axon, it is nowadays used for all sorts of ion currents encountered in neuronal modeling. In cortical cells many distinct ionic currents contribute to the response behavior. By including the corresponding description of the ionic currents in the HH model, a broad range of different response behaviors can be reproduced. For instance, Destexhe et al. (2001) developed a single compartment HH model, which was able to recreate *in vivo*-like activity.

The membrane potential V of the Hodgkin-Huxley neurons changes in time according to the following differential equation:

$$C_m \frac{dV}{dt} = -I_L - I_{Na} - I_K - I_M - I_s, \quad (2.2)$$

where C_m is the membrane capacitance, I_L is the leak current, and I_s represents the synaptic current. In addition to the LIF model, eq. (2.2) contains the spike generating sodium I_{Na} and potassium I_K currents.

The different ion currents describe the flow of ions across the membrane and are assumed to be linearly related to V :

$$I_j = g_j(V - E_j), \quad (2.3)$$

where g_k is the conductance associated with the k -th ion channel, and E_k is the corresponding reversal potential. In general, the different ion currents are separated into three parts. The leakage current I_L , which represent the approximately constant ion currents that maintain the ion concentration gradients, similar as in the LIF model. Second, the synaptic current I_s , which arises from the opening of ion channels, because of synaptic activity. And third, the voltage dependent currents, which arise from the active membrane conductances and provide the neuron with the necessary nonlinearities for the generation of complex spike patterns.

From single channel studies it is known that ion currents consist of different subunits. Only if all subunits are activated, a single channel is in the open state, which allows for an ion current flow through the membrane. The transition between the open and close state is probabilistic and can be modeled at different levels of rigor (Koch, 1998; Dayan and Abbott, 2001). However, a membrane patch of a neuron consists of several hundreds or more ion channels of the same type, which allow for a deterministic representation of the ion currents, because fluctuations average out if channels act independently. Thus, membrane conductances are usually modeled using kinetic equations, which describe the fraction of channels in the activated (open) or inactivated state.

According to the original Hodgkin-Huxley model, the spike generating sodium channels consist of both activating and inactivating subtypes, where as the delayed-rectifier potassium channels have only activating subunits. The total voltage dependent conductance is described as:

$$g_{Na} = \bar{g}_{Na} m^3 h \tag{2.4}$$

$$g_K = \bar{g}_K n^4. \tag{2.5}$$

where \bar{g}_{Na} and \bar{g}_K are the maximal conductance of a particular membrane batch. The activation variables m , n and the inactivation variable h are modeled using first order differential equations of the form:

$$\frac{dm}{dt} = \alpha_m(V) (1 - m) - \beta_m(V) m \tag{2.6}$$

$$\frac{dh}{dt} = \alpha_h(V) (1 - h) - \beta_h(V) h \tag{2.7}$$

$$\frac{dn}{dt} = \alpha_n(V) (1 - n) - \beta_n(V) n, \tag{2.8}$$

where $\alpha_m(V)$, $\alpha_h(V)$, $\alpha_n(V)$ and $\beta_m(V)$, $\beta_h(V)$, $\beta_n(V)$ are voltage dependent opening and closing rate functions.

Near spike threshold, an initial rise of the membrane potential (i.e. because of an EPSP) leads to an increase of m because of the higher value of the opening rate function $\alpha_m(V)$. Since at the beginning of the action potential the inactivation variable h is around 0.6, the increase of m leads to a higher value of the sodium conductance and thus to a larger influx of sodium ions, which in turn results in further increases of the membrane potential. Because of this positive feedback loop, m jumps from nearly zero to a value near one, which causes the membrane potential to rise rapidly towards the sodium reversal potential. However, the strong increase of the membrane potential affects the inactivation variable h in opposite direction driving it toward zero, which leads to a stop of the influx of the sodium ions. Meanwhile, the increase of the membrane potential also leads to a jump of the potassium activation variable towards one, which activates the potassium conductance. The resulting potassium current drives the membrane potential towards its resting value. Because of the delay of the potassium current, the combination of both current allows the generation of action potentials.

Figure 2.3A shows an example trace of the membrane potential of the Hodgkin-Huxley model neuron (detailed description of the model can be found in appendix

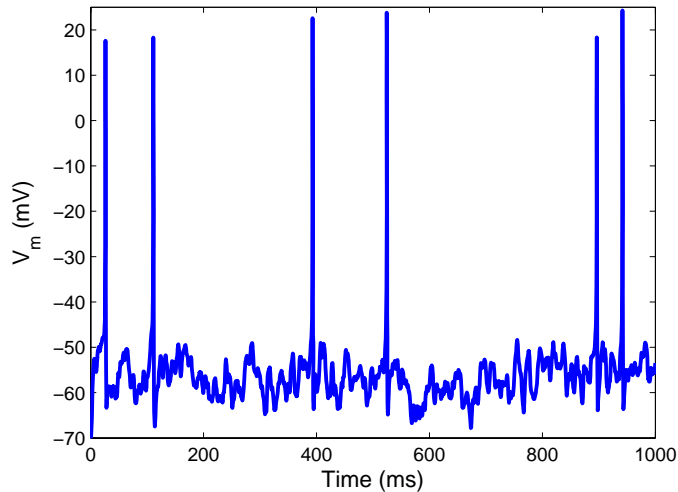


Figure 2.3.: Membrane potential trace of the simulated Hodgkin-Huxley model neuron. The neuron received $N_e = 2000$ excitatory (*AMPA*) and $N_i = 2000$ inhibitory (*GABA_A*) synapses, triggered by independent Poisson processes. The average firing rates were $\lambda_e = 2 \text{ Hz}$ and $\lambda_i = 1.24 \text{ Hz}$, which leads to a mean and standard deviation of V_m of $\langle V_m \rangle = -57 \text{ mV}$ and $\sigma_V = 3.35 \text{ mV}$. The simulation time step was $dt = 0.1 \text{ ms}$.

A). The neuron received $N_e = 2000$ excitatory (*AMPA*) and $N_i = 2000$ inhibitory (*GABA_A*) synapses, triggered by independent Poisson processes with average firing rates of $\lambda_e = 2 \text{ Hz}$ and $\lambda_i = 1.24 \text{ Hz}$ in order to recreate synaptic background activity. The synaptic activity led to a fluctuating membrane potential with mean and standard deviation of $\langle V_m \rangle = -57 \text{ mV}$ and $\sigma_V = 3.35 \text{ mV}$, which occasionally generates action potentials (average firing rate of 6.9 Hz).

In this thesis we used two slightly different Hodgkin-Huxley models. The first, which we have used to derive the results presented in Sec. 6, was proposed by Destexhe et al. (2001). It includes voltage dependent sodium and potassium currents for action potential generation, and a non-inactivating potassium current for spike frequency adaptation. They carefully adapted the kinetic equations of the ion channels in accordance to available experimental data of neocortical pyramidal cells. However, it turned out in a later study that these model equations are not suitable for the modeling of the experimental data presented in chapter 3, because they generate broad action potentials with a strong after hyperpolarization. We therefore used in chapter 3 a second model, which was proposed by Wang and Buzsaki (1996). Although their model was originally developed to describe the action potentials of interneurons, we

found that - after some adaptation - the model generates action potentials which are in good agreement with the experimental data. For a detailed description of the kinetic equations of both models see appendix A.

2.3. Synaptic Noise Models

In recent years different noise models have been developed to approximate synaptic background activity. In general, synaptic noise is modeled either explicitly, considering thousands of synapses, or implicitly, using stochastic processes. Stochastic processes are often considered because their simulation is computationally efficient. In the following we shortly review three noise models, which can reproduce the statistical and spectral properties of the fluctuating membrane potential to certain degrees. The different models are used frequently in this thesis.

2.3.1. Gaussian White Noise

The total synaptic current, which is generated from small PSP (e.g. Dirac delta pulses) of many excitatory and inhibitory synapses driven by Poisson processes, can be described by a white Gaussian noise (Ricciardi, 1977; Tuckwell, 1988). Consider a process defined by:

$$W_a(t) = a(N_e(t) - N_i(t)), \quad t \geq 0 \quad (2.9)$$

where a is a constant and $N_e(t)$ and $N_i(t)$ are independent Poisson processes with mean rates $\lambda_e = \lambda_i = \lambda$. For $a^2 \sim \frac{2}{\lambda}$ and $\lambda \rightarrow \infty$, which means vanishing amplitudes and infinite rates for the Poisson processes, the sequence of random variables $W_a(t)$ approaches (in distribution) to a normal random variable

$$W(t) = \lim_{\lambda \rightarrow \infty} W_a(t) \quad (2.10)$$

with mean zero and standard deviation t . $W(t)$ is also known as Wiener process and its derivative, $\frac{dW}{dt}$, is called white noise. The derivation of eq. (2.10) is based on the diffusion approximation [for a more detailed description see Tuckwell (1988)].

Gerstein and Mandelbrot (1964) proposed the Wiener process with drift as an approximate model for synaptic background activity. Under the assumption that the PSP alter the membrane potential according to the following stochastic process

$$V_a(t) = a_e N_e(t) - a_i N_i(t), \quad t \geq 0, \quad (2.11)$$

the total synaptic current can be approximated by a Wiener process with drift

$$I_s(t) = \mu + D \frac{dW}{dt}, \quad (2.12)$$

where the drift term μ and the diffusion coefficient D equal

$$\mu = a_e \lambda_e - a_i \lambda_i, \quad (2.13)$$

$$D^2 = a_e^2 \lambda_e + a_i^2 \lambda_i. \quad (2.14)$$

Note, that the variance of this process increases linearly with t to infinity in the absence of a threshold.

2.3.2. Gaussian Colored Noise

In the above Gaussian white noise approximation, the individual PSP's are assumed to be Dirac delta pulses $\delta(t)$. The same diffusion approximation can be performed for the biologically more realistic exponential synapses, e.g. synapses with an instantaneous rise a_e or drop a_i followed by an exponential decay at rate τ . This model was proposed first by Stein (1965) and is often referred to as Stein's model in literature. If the synaptic events are triggered by independent Poisson processes $N_e(t)$ and $N_i(t)$, and $a_{e,i} \sim \frac{1}{\lambda_{e,i}}$ with $\lambda \rightarrow \infty$, than it can be demonstrated (Tuckwell, 1988) that the resulting random variable X is well described by an Ornstein-Uhlenbeck process (OUP):

$$\frac{dX(t)}{dt} = -\frac{1}{\tau}(X(t) - \mu) + D \frac{dW}{dt}, \quad (2.15)$$

where τ is the synaptic decay constant, and μ and D are given by:

$$\mu = \tau(a_e \lambda_e - a_i \lambda_i), \quad (2.16)$$

$$D^2 = \frac{\tau}{2}(a_e^2 \lambda_e + a_i^2 \lambda_i). \quad (2.17)$$

For $\tau > 0$, the noise is called "colored noise".

Figure 2.4 shows one realization of the process $X(t)$ for $\tau = 2 \text{ ms}$ in the interval $t \in [0, 100] \text{ ms}$. At time $t = 100 \text{ ms}$, the decay time is raised to $\tau = 10 \text{ ms}$ for the next 100 ms . A smaller value of τ leads to a faster changing noise process, which means that the correlation between two points in time is smaller. In other words, given $X(t)$ until the time t_1 , the value of the process $X(t)$ at $t_2 > t_1$ is less predictable for smaller values of τ . In Chapter 5 we investigate the role of the temporal correlation for the detection of weak transient inputs in detail.

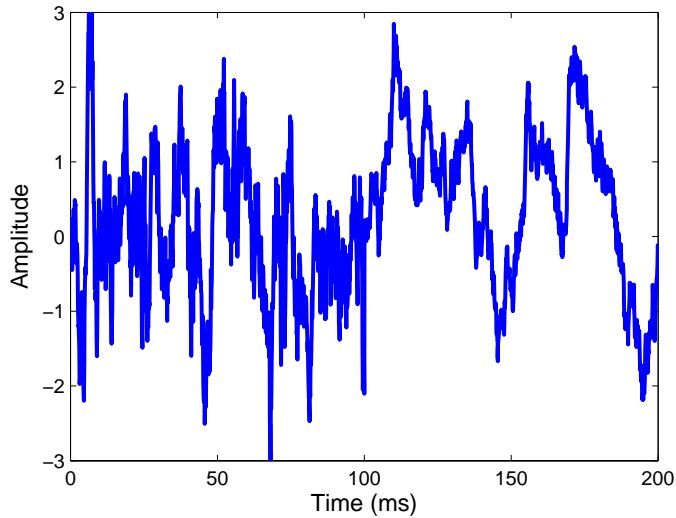


Figure 2.4.: A) Example trace of Gaussian colored noise $X(t)$. The time constant τ changes at $t = 100 \text{ ms}$ from $\tau = 2 \text{ ms}$ to $\tau = 10 \text{ ms}$, leading to a slower fluctuating noise process. Note that D was adjusted such that the standard deviation of the noise process remains the same.

2.3.3. Conductance Noise Model

In the conductance-based noise model, the total synaptic current I_s is described by the following equation:

$$I_s(t) = g_e(t)(V(t) - E_e) + g_i(t)(V(t) - E_i), \quad (2.18)$$

where E_e and E_i are the excitatory and inhibitory reversal potentials, and $g_e(t)$ and $g_i(t)$ are the conductances of the excitatory and inhibitory synapses, respectively.

Destexhe et al. (2001) suggested modeling $g_e(t)$ and $g_i(t)$ as Ornstein-Uhlenbeck processes. However, the OUP processes predict negative conductances if the mean and standard deviation of the OUP are of similar magnitude. In this regime, the diffusion approximation misses essential high-order terms of the membrane potential distribution, as for example its skew (Richardson and Gerstner, 2005). In order to account for the conductance increase due to the synaptic activity, Richardson and Gerstner (2005) suggested either using voltage equations with a current-noise and reduced membrane time constants, or modeling the synaptic noise in single compartment models explicitly, e.g. by considering thousands of synapses. The second approach has

the additional advantage in that it includes the effect of shot noise on the membrane potential dynamics and it can be easily extended in order to introduce correlations between the membrane potential of pairs of neurons.

The total excitatory or inhibitory conductance is given by

$$g_{i,e}(t) = g_{max} \sum_{k=1}^{N_{e,i}} r_k(t), \quad (2.19)$$

where g_{max} is the maximal conductance of the excitatory or inhibitory synapse, and N_e and N_i is the number of occurrence of these synapses, respectively. The variable r_k represents the fraction of receptors in the open state of synapse k and is well described by a two-state kinetic model (Destexhe et al., 1994):

$$\frac{dr_i}{dt} = \alpha[T] (1 - r_i) - \beta r_i, \quad (2.20)$$

where α and β are voltage independent forward and backward state transition rates. The variable $[T]$ represents the transmitter concentration, which is typically set to a value of $1mM$ for the duration of $1ms$ in order to simulate the opening of the ion channels, and is otherwise zero. The duration of the ion channels in the open state determines the length of the rising phase of the postsynaptic potential. It is important to note that the high values of membrane potential fluctuations observed *in vivo*, e.g. $\sigma_V > 4mV$ (Anderson et al., 2000a; Destexhe et al., 2003), can only be achieved in the explicit model, if some of the synapses release simultaneously.

We have used the explicit noise model in chapter 6 to investigate how well the information rate can be estimated from a neural population if the firing of neurons is pair wise correlated.

2.4. Analysis Methods

The study of neural coding requires analysis methods for the characterization of neural responses. Some of them are used throughout of this thesis and, therefore, shortly introduced in the following.

2.4.1. Correlation Function and Spectral Density

In this thesis we deal only with stationary stochastic processes. A process $x(t)$ is called stationary if the processes $x(t)$ and $x(t + \tau)$ have the same statistics for any τ (Papoulis, 1991).

The auto-correlation function of a stationary stochastic process depends only on the time difference τ (Papoulis, 1991) and is by definition the estimate of the correlation between $x(t)$ and $x(t + \tau)$ at every pair of times separated by τ , e.g.

$$R_{xx}(\tau) = \langle x(t + \tau)x^*(t) \rangle, \quad (2.21)$$

where $*$ denotes the complex conjugate. In other words, the auto-correlation characterizes how well the value of $x(t + \tau)$ can be inferred from $x(t)$. If we are given two jointly stationary processes $x(t)$ and $y(t)$, the cross-correlation function of these two processes is given by

$$R_{xy}(\tau) = \langle x(t + \tau)y^*(t) \rangle. \quad (2.22)$$

Another property of interest is the correlation time (or temporal correlation) of a stochastic process. According to Papoulis (1991) we define the correlation time as the ratio

$$\tau_C = \frac{1}{C_{xx}(0)} \int_0^\infty C_{xx}(\tau) d\tau, \quad (2.23)$$

where $C_{xx}(\tau)$ is the auto-covariance function of $x(t)$, e.g.

$$C_{xx}(\tau) = R_{xx}(\tau) - |\mu_x|^2, \quad (2.24)$$

and μ_x is the mean of $x(t)$. In chapter 5 we estimate the temporal correlation of the membrane potential for different noise conditions and investigate how the detection of transient inputs depends on it.

The spectral density describes how the variance of a stochastic process is distributed with frequency. The spectral density (or power spectrum) of a stationary process $x(t)$ is the Fourier transform $P_{XX}(\omega)$ of its auto-correlation function $R_{xx}(\tau)$ (Papoulis, 1991):

$$P_{XX}(\omega) = \int_{-\infty}^\infty R_{xx}(\tau) e^{-j\omega\tau} d\tau. \quad (2.25)$$

The cross-power spectrum (P_{XY}) of two processes is accordingly defined as the Fourier transform of the cross-correlation function $R_{xy}(\tau)$.

The power spectrum (P_{XX}) and the cross power spectrum (P_{XY}) were usually obtained using Welch's method (Papoulis, 1991). This means that the entire stochastic process is separated in to segments of equal duration. Each segment is then transformed to Fourier-space, multiplied by its complex conjugate and averaged at each frequency to yield the estimate of the power spectrum:

$$P_{XY}(\omega) = C_w \langle X(\omega)Y(\omega)^* \rangle, \quad (2.26)$$

where C_w is a normalization coefficient whose value depend on the window function used for the Fourier transform. Power spectra were usually calculated using build-in functions from *matlab*.

2.4.2. Information Rate Estimation with Linear Filter

In recent years, many neuroscientists have used information theory and systems analyzing techniques to characterize information encoding in neural systems (Bialek et al., 1991; Gabbiani, 1996; Rieke et al., 1997; Strong et al., 1998; Borst and Theunissen, 1999; Reinagel and Reid, 2000; Krahe et al., 2002; Hatsopoulos et al., 2004). The linear reconstruction method in particular has been widely used in computational neuroscience studies because it requires less data and is simple to use. Throughout this thesis, we also use the linear reconstruction method to assess information encoding and, therefore, introduced this method in detail.

The Linear Reconstruction Method

The basic idea behind the reconstruction method is to first use systems analysis methods to generate an estimate S_{est} of the stimulus S and then to use this estimate to calculate a lower bound on the true information rate between the stimulus and response. Since the estimate contains no information that was not actually present in the neural response, the information rate between the stimulus and its estimate $I(S, S_{est})$ is a lower bound on the true information rate between the stimulus and the response $I(R, S)$ [Gabbiani, 1996; Rieke et al., 1997; Borst and Theunissen, 1999]:

$$I(R, S) \geq I(S, S_{est}). \quad (2.27)$$

The linear reconstruction method assumes a linear relationship between the stimulus and response (Borst and Theunissen, 1999). The estimate for the input stimulus is then given by the convolution of the neural response $R(t)$ with the filter h

$$S_{est}(t) = \int_{-\infty}^{\infty} h(s)R(t-s) ds, \quad (2.28)$$

where h is a linear, non-causal filter, which minimizes the mean square error $[\epsilon^2(h)]$ between the stimulus S_{stim} and its estimate S_{est} , e.g.

$$\epsilon^2(h) = \frac{1}{T} \int_0^T [S_{stim}(t) - S_{est}(t)]^2 dt. \quad (2.29)$$

The filter h can be obtained from the neural response by solving the condition

$$\frac{d\epsilon^2(h)}{dh} = 0 \quad (2.30)$$

for h (Wiener-Kolmogorov filtering). One obtains

$$\hat{h}(\omega) = \frac{P_{SR}(-\omega)}{P_{RR}(\omega)}, \quad (2.31)$$

where $P_{RR}(\omega)$ is the power spectrum of the spike train and $P_{SR}(\omega)$ denotes the Fourier transform of the cross-correlation of the stimulus and the spike train (further on referred to as cross power spectrum).

We define as *noise* the difference between the stimulus S_{stim} and its estimate S_{est} , $n(t) = S_{stim} - S_{est}$. The power spectrum of the noise $P_{NN}(\omega)$ is then given by (Gabbiani, 1996)

$$P_{NN}(\omega) = P_{SS}(\omega) - \frac{|P_{SR}(\omega)|^2}{P_{RR}(\omega)}. \quad (2.32)$$

If we define the signal to noise ratio (*SNR*) as

$$SNR(\omega) = \frac{P_{SS}(\omega)}{P_{NN}(\omega)} \quad (2.33)$$

$$= \frac{P_{SS}(\omega)}{P_{SS}(\omega) - \frac{|P_{SR}(\omega)|^2}{P_{RR}(\omega)}} \quad (2.34)$$

$$= \frac{1}{1 - \gamma^2(\omega)}, \quad (2.35)$$

where the function

$$\gamma^2(\omega) = \frac{|P_{SR}(\omega)|^2}{P_{SS}(\omega)P_{RR}(\omega)} \leq 1 \quad (2.36)$$

is the coherence between the stimulus and the response.

The lower bound on the information rate is obtained from the signal to noise ratio with the following formula,

$$I_{lin} \geq \frac{1}{2\pi} \int_0^\infty \log_2 [SNR(\omega)] d\omega \quad (2.37)$$

$$= -\frac{1}{2\pi} \int_0^\infty \log_2 [1 - \gamma^2(\omega)] d\omega \quad (2.38)$$

In the case of a Gaussian stimulus, the estimate is close to the true information rate if the noise in the reconstruction is Gaussian distributed. For a more detailed description of the linear decoding approach see Borst and Theunissen (1999) and references within.

3. γ -Band Membrane Potential Fluctuations and Stimulus Encoding

3.1. Introduction

Presentation of visual stimuli induces in cells of the visual cortex strong modulation of the membrane potential at the temporal frequency of stimulation (cf. Sec. 1). In addition to the slow depolarizations, the membrane potential often shows an increased activity in the high frequency range, including the γ -band ($25 - 70 \text{ Hz}$). High frequency, γ -band fluctuations of the membrane potential are typical for visual cortical neurons and are present in cells with both, simple and complex receptive fields (Jagadeesh et al., 1992; Gray and McCormick, 1996; Anderson et al., 2000b; Volgushev et al., 2002, 2003). The high frequency fluctuations in the membrane potential of visual cortical neurons are, most probably, of synaptic origin (Bringuier et al., 1997; Lampl et al., 1999) and their amplitude often changes with spontaneous fluctuations of the membrane potential (Anderson et al., 2000b), similar to the cells in other regions of the neocortex (Steriade et al., 1996; Mukovski et al., 2006).

It has been suggested that the γ -range fluctuations play an important role in cortical information processing. For example, synchronization of γ -activity across subpopulations of neurons, which encode different features of an object, may serve as a mechanism enabling feature specific binding of neuronal responses (Eckhorn et al., 1988; Gray and Singer, 1989; Singer, 1993, 1999). Intracellular studies reveal a number of properties of the γ -band fluctuations, which enable them to subserve synchronisation and patterning of neuronal activity. For instance, γ -band fluctuations support reliable spike generation, impose precise temporal windows for synaptic integration and produce precise temporal patterns of activity (Lampl and Yarom, 1993; Mainen and Sejnowski, 1995; Nowak et al., 1997; Volgushev et al., 1998, 2003; Salinas and Sejnowski, 2000). Another aspect of the functional importance of the high frequency activity is its capability to facilitate detection of weak signals by the mechanism similar to stochastic resonance. In the visual cortex, this mechanism has been suggested as playing a role in producing contrast invariance of the orientation tuning (Anderson et al. 2000a).

Simple cells in the visual cortex encode temporal characteristics of visual stimuli in the temporal structure of their firing (Dean and Tolhurst, 1983; Skottun et al., 1991), which is coupled to depolarizations of the membrane potential, occurring at temporal frequency of the stimulation (Carandini and Ferster, 2000; Volgushev et al., 2003). Recently we have found that the amplitude of the γ -band fluctuations correlated with the phase of the low frequency, stimulus-induced membrane potential changes, being maximal at depolarization peaks and minimal at hyperpolarization troughs of the membrane potential responses (Volgushev et al., 2003). We hypothesized that this coupling of the strength of the high frequency fluctuations to the phase of the slow, stimulus-frequency membrane potential changes may improve stimulus encoding.

Here we tested this hypothesis using a single compartment conductance-based neuron model. The input to the model was adjusted to reproduce typical features of membrane potential responses and firing rates, recorded in cat visual cortical neurons during presentation of moving gratings. We simulated responses of the model neuron to presentation of moving gratings of different orientations. The model neuron was subject to fluctuating conductance inputs of three different classes. In the first class, only the low (stimulus) frequency component of the input was orientation-dependent. In the second class, in addition to orientation-dependence of the low-frequency component, also the γ -range component depended on orientation. In the third class, both the low-frequency and the γ -band components depend on orientation and, in addition, the strength of the γ -band fluctuations was modulated by the slow, stimulus-frequency changes of the membrane potential. We show that stimulus encoding is greatly improved only for the third class of synaptic inputs.

3.2. Materials and Methods

3.2.1. Physiology

Experiments were performed on eight adult cats (3.0 – 4.5kg). The procedures were approved by a local animal welfare committee (Bezirksregierung Ansberg, Germany). The details of the surgery and the maintenance of animals are described elsewhere (Voslushev et al., 2000, 2003). Intracellular recordings were made with sharp electrodes filled with 2.5 Mol potassium acetate. Electrode resistance was 70 – 120 $M\Omega$. Neurons with a stable resting membrane potential were recorded for at least 15 *min* at a sampling frequency of 10 – 40 *kHz*. Visual responses were evoked by moving gratings of different orientations, which were presented in pseudo-random order on a screen in front of the animal. The gratings were generated using subroutines of the Vi-

sion Works stimulation system (Cambridge Research Systems, New Hampshire, USA) and our own programs.

Spectral analysis of the membrane potential was performed after the action potentials were removed. Action potentials were first detected by the threshold and then their onset was determined as the point at which the rate of change of the membrane potential $\frac{dV}{dt}$ first exceeded 5% of the maximal rate of $\frac{dV}{dt}$ for the action potentials of the particular neuron. To safely remove the entire waveform of the action potential, we linearly interpolated the membrane potential between the interval from 0.7 ms before the onset to T_{post} after it. Spike detection threshold (usually 30–40 mV from the mean resting membrane potential) and T_{post} (usually 3 – 5 ms) were adjusted individually for each cell by visual inspection of the voltage traces.

The stimulus and the γ -range component of the membrane potential were extracted as follows. First we transformed the membrane potential into Fourier-space using the Fast-Fourier transform (FFT) function of MatLab (Mathworks, version 6.5), then we set all coefficients corresponding to frequencies outside the desired range to zero and performed the inverse FFT to transform the result back to time domain. The low frequency range was set to 1 – 3 Hz in order to cover the temporal frequency of the visual stimulation. The γ -range was set 25 – 70 Hz. The relationship between the phase of the slow changes of the membrane potential and the amplitude of the γ -range fluctuations was quantified as following. We calculated the power of the γ -range fluctuations of the membrane potential in a running window of 102.4 ms, with 10 ms step, and then calculated the linear correlation coefficient between this signal and the low frequency component.

3.2.2. Single Compartment Model

For all simulations in this paper we used a single-compartment conductance-based model adapted from Wang and Buzsaki (1996) modified as described below. The model contained Hodgkin-Huxley type ion currents and time-dependent excitatory and inhibitory synaptic conductances. Changes of the membrane potential V of the model neuron are described by the following differential equation:

$$C_m \frac{dV}{dt} = -I_L - I_{Na} - I_K - I_M - I_{syn}, \quad (3.1)$$

where C_m is the membrane capacitance, I_L is the leak current, I_{Na} and I_K are the spike generating sodium and potassium currents, I_M is a non-inactivating potassium current

for spike frequency adaptation, and I_{syn} is the total synaptic current. Dynamics of each ionic current (for synaptic see below) is given by the following equation:

$$I(t) = g(t)[V(t) - E_{reversal}], \quad (3.2)$$

where $g(t)$ is the respective ionic conductance, and $E_{reversal}$ is the reversal potential of that current. For the leak current, the reversal potential was $E_L = -75 \text{ mV}$ and the leak conductance g_L did not change with time, but remained constant.

Since this model was originally developed to simulate a network of fast-spiking interneurons, we have adjusted it as follows. To account for the fast initiation dynamics of action potentials in neocortical neurons (Naundorf et al., 2006), we set the kinetics of sodium channels 10 times faster, and the width of their activation curve 2 times narrower, than in the original model. This allowed the firing patterns and rates during stimulation as well as the shape of the generated action potentials to be brought closer to the experimental data. Details of the kinetic equations of the intrinsic currents and the other model parameters are given in Appendix A.

The total synaptic current I_{syn} , which represents the synaptic input evoked by the visual stimulation as well as the background activity, is described as:

$$I_{syn}(t) = g_e(t)(V(t) - E_e) + g_i(t)(V(t) - E_i), \quad (3.3)$$

where $g_e(t)$ and $g_i(t)$ are stochastic processes, which represent the conductance of the excitatory and inhibitory synapses, and E_e and E_i are the reversal potentials of the excitatory and inhibitory currents. The excitatory $g_e(t)$ and inhibitory $g_i(t)$ conductance traces were derived from a Gaussian white noise, which was filtered in order to obtain fluctuations of the membrane potential with a spectral composition, similar to the spectral composition of the experimental data. Details of this adjustment of the model parameters to the experimental data are explained in Sec. 3.3.2.

Visual stimulation was simulated by adding a sinusoidal excitatory conductance to the excitatory background activity, $g_{e0}(t)$. The total excitatory synaptic conductance, $g_e(t)$, is then given by:

$$g_e(t) = \bar{G}_e + g_s \sin(2\pi ft) + g_{e0}(t), \quad (3.4)$$

where \bar{G}_e is the mean conductance, g_s determines the strength of the stimulation by a grating with a given temporal frequency (for example, $f = 3 \text{ Hz}$), and $g_{e0}(t)$ represents the excitatory background activity. Further details are given in Appendix C.

3.2.3. Estimation of the Information Rate

Information theory provides the most rigorous way to assess the quality of stimulus encoding. To estimate the information rate in our recordings and simulation experiments, we have exploited a linear filter approach, which has been widely used in computational neuroscience studies (Bialek et al., 1991; Gabbiani, 1996; Rieke et al., 1997; Borst and Theunissen, 1999). For more information about this approach see Sec. 2.4.2.

A lower bound on the information rate between stimulus and response can be obtained from the following equation (Gabbiani, 1996; Borst and Theunissen, 1999):

$$I_{LB} = -\frac{1}{2\pi} \int_0^\infty \log_2 [1 - \gamma^2(\omega)] d\omega, \quad (3.5)$$

where γ^2 is the coherence between the stimulus and the response. The coherence is obtained from

$$\gamma^2(\omega) = \frac{|P_{SR}(\omega)|^2}{P_{SS}(\omega)P_{RR}(\omega)} \leq 1, \quad (3.6)$$

where $P_{SS}(\omega)$ and $P_{RR}(\omega)$ are the power spectra of the stimulus and the spike train, and $P_{SR}(\omega)$ denotes the Fourier transform of the cross-correlation of the stimulus and the spike train.

The coherence $\gamma^2(\omega)$ was calculated as follows. From the membrane potential traces of 5000 *ms* duration, which were recorded during grating movement, we extracted the low frequency component (1–3 *Hz*) of the membrane potential fluctuations (stimulus). The spike response was constructed as a train of delta pulses, with pulses at spike onset times (spike onset times were determined as described above). Stimulus and spike response were then divided into segments of 819.2 *ms* duration (with an overlap of 50%). All segments were then transformed into Fourier space, multiplied by its complex conjugate, and averaged at each frequency to yield the estimate of the power spectrum (P_{XX}) and the cross power spectrum (P_{XY}), e.g. $P_{XY}(\omega) = \langle X(\omega)Y(\omega)^* \rangle$, where $*$ denotes the complex conjugate and $\langle \rangle$ denotes the averaging over segments. We used the same procedure for the calculation of the information rate of the simulated traces, which had duration of 200 *sec*.

3.3. Results

Results presented in this paper consist of three sections. First, we describe intracellular recorded responses of cat visual cortex neurons to presentation of visual stimuli *in*

in vivo. These data were used to obtain key features of the membrane potential changes, which were then reproduced in the simulations. Furthermore, stimulus encoding in the recorded neurons was characterized from these data for a later comparison with the simulation results. Second, we constructed input conductances, which reproduced in a model neuron the main parameters of the recorded membrane potential traces. Third, we studied in the model neuron the influence of correlations between the amplitude of high frequency (γ -range) fluctuations of the membrane potential and the phase of the low frequency changes ($0.3 - 3 Hz$) on the stimulus encoding in a conductance-based neuron model. Most parameters of the model neuron were constrained to data obtained from cellular recordings of neurons in the cat visual cortex (Volgushev et al., 2003).

3.3.1. Intracellular Recordings from Cat Visual Cortex Neurons

Intracellular recordings were made from neurons in cat visual cortex *in vivo*. For the analysis, we have selected 9 neurons with simple receptive fields, which showed clear response modulation at temporal frequency of the optimally oriented moving grating (Dean and Tolhurst, 1983; Skottun et al., 1991; Carandini and Ferster, 2000, Volgushev et al., 2003). In these recordings, we analyzed key features of the cellular responses to presentation of moving gratings of different orientations and directions of movement. Specifically, we quantified the relation between stimulus orientation/direction of movement on the one hand, and low frequency ($< 4 Hz$) modulation of the membrane potential at temporal frequency of stimulation, high frequency ($> 25 Hz$) fluctuations of the membrane potential and spike responses on the other. We also characterized the relation between low frequency and high frequency fluctuations of the membrane potential and encoding of the stimulus in the spike trains of recorded neurons.

Fig. 3.1 shows an example of membrane potential traces of a visual cortex cell during responses to the presentation of a moving grating of optimal (Fig. 3.1A) and non-optimal orientation (Fig. 3.1D). An optimally orientated grating induced strong modulation of the membrane potential at the temporal frequency of stimulation, accompanied by strong fluctuations in the high frequency range and bursts of action potentials at depolarization peaks (Fig. 3.1A). The low frequency ($0.3 - 3 Hz$) modulation reached about $20 mV$ peak-to-peak amplitude (Fig. 3.1B, continuous trace). High frequency components ($25 - 70 Hz$; γ -range) of the membrane potential fluctuations were estimated after spike removal (see Methods for details). High frequency fluctuations of the membrane potential reached peak-to-peak amplitude of more than $10 mV$ (Fig. 3.1C).

3. γ -Band Membrane Potential Fluctuations and Stimulus Encoding

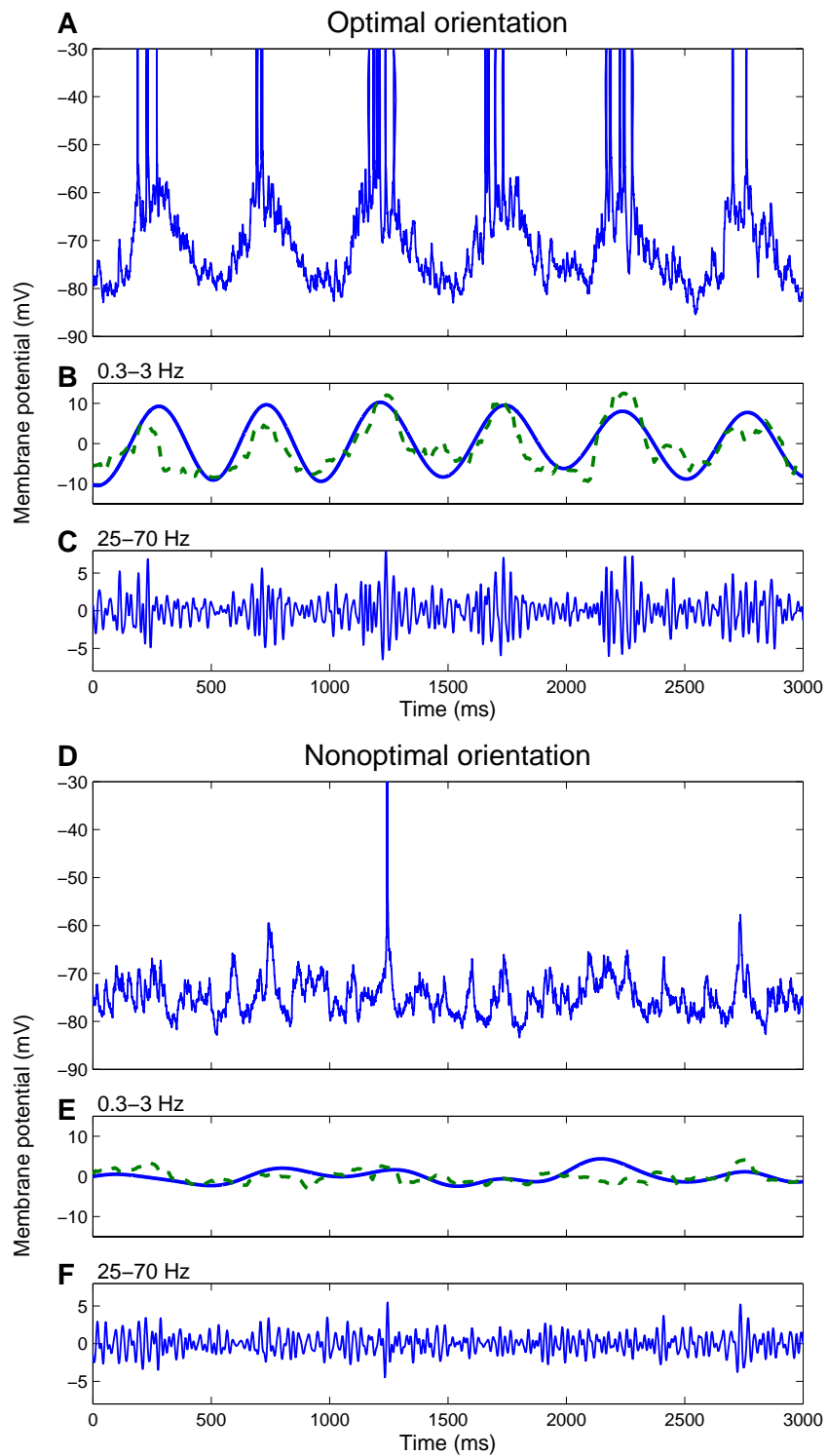


Figure 3.1.: Responses of a cell in cat visual cortex to optimally orientated moving gratings of optimal (A) and non-optimal (D) orientations and their analysis. A) and D): Membrane potential traces. Temporal frequency of the moving grating was 2Hz. Action potentials are truncated. B), C) and E), F): Analysis of the relation between the low frequency component [0.3 – 3 Hz, solid lines in B) and E)] and the high frequency, γ -range component [25 – 70 Hz, solid lines in C) and F)] from the traces in A) and D). In B) and E), dashed lines show the power of the γ -range fluctuations estimated in a running window of 102.4 ms. Note that the γ -power (dashed) curves are normalized to match the amplitude of the respective low frequency components.

Comparison of the two components demonstrates clearly that the amplitude of the γ -range fluctuations correlated with the phase of the low frequency membrane potential modulation. The amplitude of high frequency fluctuations was high at depolarizing peaks (positive phase) of the low frequency modulation, but much lower during negative phases, at relatively hyperpolarized membrane potentials. To quantify the relationship between the slow membrane depolarizations (continuous trace in Fig. 3.1B) and the amplitude of the γ -range membrane potential fluctuations we first calculated a running average of the γ -power (dashed curve in Fig. 3.1B, see Sec. 3.2 for details), and then calculated the linear correlation coefficient between these two signals. The γ -power was significantly correlated with the slow modulation of the membrane potential ($r = 0.67$).

During presentation of orthogonally oriented (non-optimal) grating, both the low frequency modulation and high frequency fluctuations of the membrane potential were much weaker, and action potentials were generated only occasionally (Fig. 3.1D). Despite the low amplitude, a comparison of the low (Fig. 3.1E) and high (Fig. 3.1F) frequency components of the membrane potential fluctuations reveals no clear relationship. Nevertheless, the strength of γ -range fluctuations was weakly but significantly correlated with the phase of the slow membrane depolarizations ($r = 0.37$).

To compare the spectral composition of membrane potential traces during presentation of optimal and non-optimal stimuli, we calculated their power spectra. Figure 3.2A shows that most pronounced difference between the power spectra for optimal (blue curve) and non-optimal orientation (red curve) was in two frequency ranges. Optimal stimuli evoked much stronger modulation of the membrane potential at low frequencies 0.3 – 3 Hz, around the temporal frequency of stimulation. We refer to the integral of the power spectrum in the range of 0.3 – 3 Hz as stimulus power. Furthermore, the power of the high frequency membrane potential fluctuations, especially in

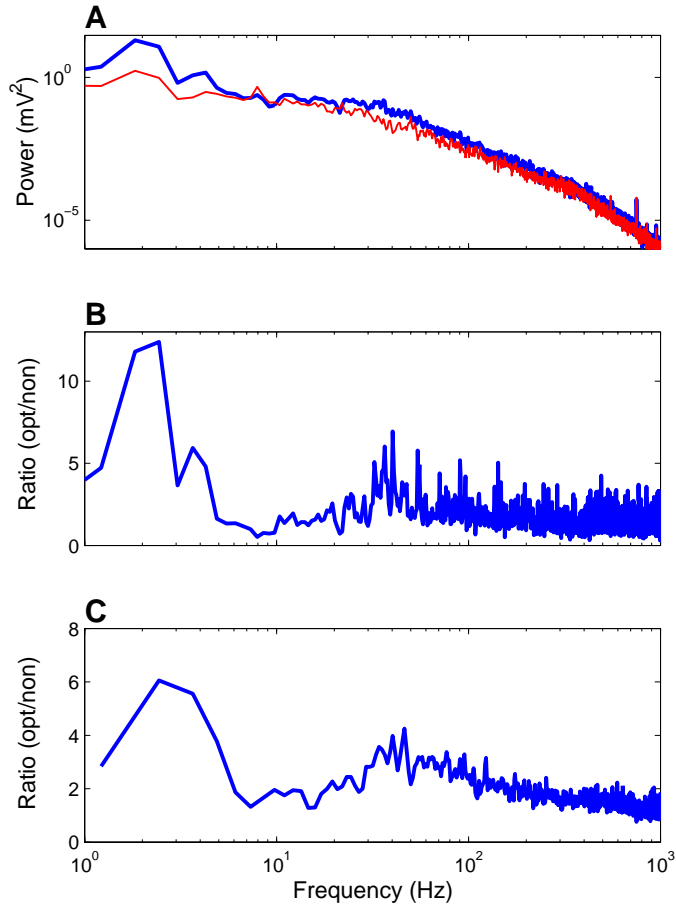


Figure 3.2.: Power spectra of the membrane potential responses to the optimal and non-optimal orientations of neurons, recorded in cat visual cortex. A) Power spectra of the membrane potential responses of the cell from Fig. 3.1 to the optimal (blue line) and non-optimal (red line) orientations. B) Ratio between the power spectra of responses to the optimal and non-optimal orientation, data from A). C) Cumulative ratio of power spectra of responses to the optimal and non-optimal orientation for nine neurons.

3. γ -Band Membrane Potential Fluctuations and Stimulus Encoding

	Optimal	Non-optimal	Null	
Spike response	16.9	0.29	6.2	Hz
Information rate	6.12	0.13	3.39	Bits/sec
Stimulus-power	33.7	3.9	9.4	mV^2
γ -power	4.78	1.92	2.68	mV^2
r	0.67	0.37	0.47	
$\langle V_m \rangle$	-69.8	-72.7	-66.4	mV

Table 3.1.: Estimated values for the mean firing rate, of the information rate, of the strength of the low (stimulus, $1 - 3\text{Hz}$) and the γ -range ($25 - 70\text{Hz}$) membrane potential fluctuations, of the linear correlation coefficient r between stimulus phase and the strength of the γ -range fluctuations, and for the mean membrane potential of the neuron, shown in Fig. 3.1.

the γ -frequency range ($25 - 70\text{Hz}$), was clearly stronger during the optimal stimulation. The difference in both the low and the high frequency ranges stands out clearly in Fig. 3.2B, in which the ratio of the two power spectra is plotted. The difference between the optimal and non-optimal responses in the two frequency ranges was typical for our sample, as illustrated by two clear peaks around the stimulus power and the γ -power on the cumulative ratios of power spectra for nine neurons (Fig. 3.2C).

Responses to the optimal and non-optimal orientations showed the most pronounced differences, summarized in Table 3.1 for the cell shown in Fig. 3.1. Responses to stimuli of other orientations were characterized by intermediate values of the above parameters, which showed clear dependence on the orientation, changing gradually with changing orientation (Fig. 3.3). In all cells, stimuli of the optimal range, as defined by the maximal spike responses, evoked the strongest modulation of the membrane potential in the low and the high frequency ranges and induced the strongest correlations between the γ -range power and the phase of low frequency modulation of the membrane potential. Furthermore, the information rates were also maximal during the responses to optimal stimuli.

Table 3.2 summarizes characteristic values for nine neurons, which were estimated from the responses to optimal, non-optimal (orthogonal orientation) and null (optimal orientation, but opposite direction of movement) stimuli. We observed more than a 10-fold difference between the optimal and non-optimal spike responses and information transfer rates. Optimal and non-optimal responses were characterized by a several-fold difference in the strength of the low (stimulus-power) and the high frequency (γ -power) membrane potential fluctuations, and a 50% to a 2-fold difference in the

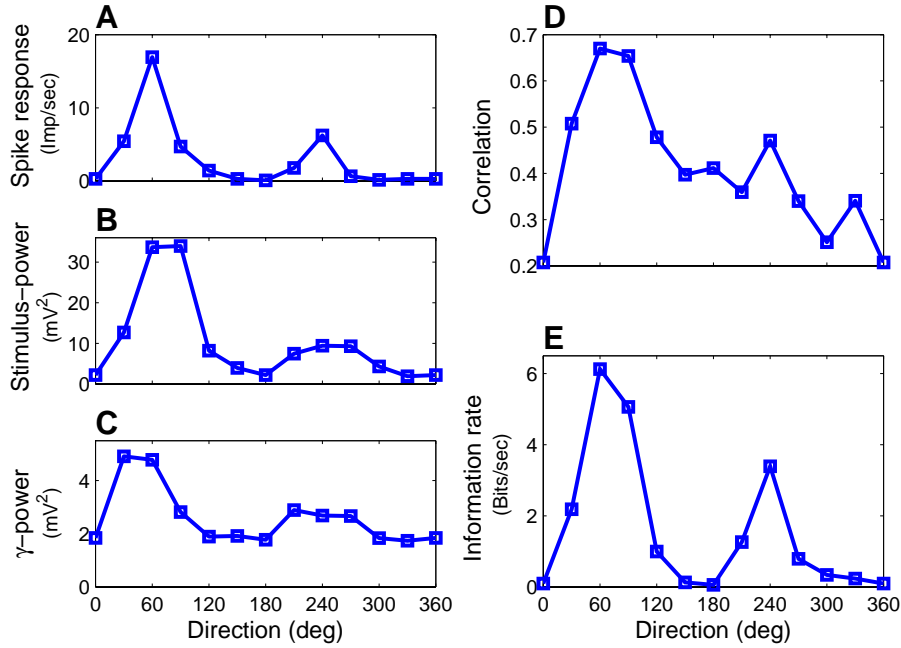


Figure 3.3.: Dependence of the response properties of the visual cortex neuron on the direction of movement of grating stimuli. Data for the cell shown in Fig. 3.1. A) Spike response. B) Stimulus-power (0.33 Hz) of the membrane potential. C) γ -power (25 – 70 Hz) of the membrane potential. D) Linear correlation coefficient between the strength of the γ -range fluctuations and the phase of the low frequency fluctuations of the membrane potential. E) and information rate.

correlation of the γ -power to the phase of the low frequency modulation (r). In the following sections, we will use these values and their ranges for restraining the models and to compare simulation results with the recordings.

3.3.2. Construction and Tuning of Input Conductances

Having quantified the properties of the membrane potential traces during responses to different orientations in the recorded neurons, we constructed input conductances, which reproduced these features in a model neuron. Specifically, we aimed to reproduce the following characteristics:

- Spectral composition of the membrane potential fluctuations.
- Averaged firing frequency.

3. γ -Band Membrane Potential Fluctuations and Stimulus Encoding

	Optimal	Non-optimal	Null	
Spike response	14.1 ± 11.9	1.1 ± 1.6	4.8 ± 3.6	Hz
Information rate	5.7 ± 2.4	0.5 ± 0.8	2.7 ± 2.0	Bits/sec
Stimulus-power	18.4 ± 9.4	3.7 ± 3.5	8.9 ± 5.9	mV^2
γ -power	2.66 ± 1.91	0.95 ± 0.65	1.8 ± 1.54	mV^2
r	0.61 ± 0.15	0.36 ± 0.12	0.48 ± 0.15	
$\langle V_m \rangle$	-68.2 ± 4.7	-71.1 ± 4.8	-68.2 ± 4.6	mV

Table 3.2.: Average values ($n = 9$) for the mean firing rate, of the information rate, of the strength of the low (stimulus, $1 - 3\text{Hz}$) and the γ -range ($25 - 70\text{Hz}$) membrane potential fluctuations, of the linear correlation coefficient r between stimulus phase and the strength of the γ -range fluctuations, and for the mean membrane potential.

- Dependence of the low frequency modulation of the membrane potential on stimulus orientation/direction of movement.
- Dependence of the high frequency fluctuations on stimulus orientation.
- Relation between low frequency and high frequency fluctuations of the membrane potential.

To construct fluctuating conductance input, which reproduces the spectral composition of membrane potential traces recorded in visual cortex neurons, the excitatory $g_e(t)$ and inhibitory $g_i(t)$ conductance traces were generated as follows. We generated a Gaussian white noise, transferred it to Fourier space, and multiplied it component-wise with a function $f(\omega)$:

$$f(\omega) = a_1 \exp(-\tau_1\omega) + a_2 \exp(-\tau_2\omega) + a_3 \exp(-\tau_3\omega), \quad (3.7)$$

and then transferred the result back to the time-domain with an inverse Fourier transformation. In the function $f(\omega)$, the parameters $a_1 - a_3$ and $b_1 - b_3$ represented three frequency ranges, $B_{low} \in [0 - 25]\text{Hz}$, $B_\gamma \in [25 - 70]\text{Hz}$, and $B_{high} \in [70 - 1000]\text{Hz}$, and were adjusted in such a way that the average power of the simulated membrane potential in each of these three frequency ranges deviated by less than 3% from the power spectrum of the recorded cell.

In Fig. 3.4A and B, power spectra of the simulated voltage traces (red lines) are shown together with the power spectra of recorded membrane potential traces (blue lines) for the optimal and non-optimal responses. This Fig. illustrates that our adjustment procedure allowed the spectral composition of the recorded membrane potential

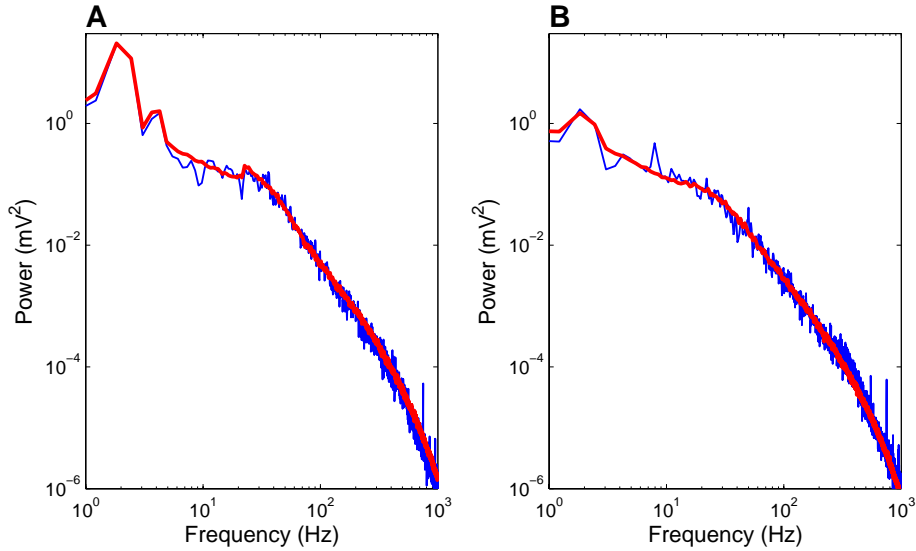


Figure 3.4.: Power spectra of the membrane potential responses to optimal (A) and non-optimal (B) orientation in the recorded cell (blue lines, the neuron from Fig.3.1) and in the simulation responses of the model neuron (red lines).

traces to be reproduced well, as well as the difference between the optimal and non-optimal responses in the two - the low and the high - frequency ranges. Adjustment of the coefficients of the function $f(\omega)$ to reproduce the frequency spectra of recorded data was performed only for optimal and non-optimal orientation. For all other orientations, the coefficients were linearly interpolated according to the measured direction tuning of neuronal responses.

Next, we implemented in the simulated traces the correlation between the amplitude of the γ -range fluctuations and the phase of slow modulation of the membrane potential using the following procedure. First we segregated the conductance trace $g_{e0}(t)$ [cf. eq. (3.4)] in Fourier space into two frequency components. The first component, $g_{e\gamma}(\omega)$, contained the frequencies in the γ -range ($25 - 70 \text{ Hz}$), and the second component, $g_{rest}(\omega)$, contained all remaining frequencies ($< 25 \text{ Hz}$ and $> 70 \text{ Hz}$). The amplitude of the γ -range component was modulated with a sinusoidal signal according to eq. (3.8). The resulting signal was then added to $g_{rest}(\omega)$ to yield the total conductance $g_{e0}(t)$:

$$g_{e0}(t) = g_{rest}(t) + \beta [1 + \epsilon \sin(2\pi ft)] g_{e\gamma}(t). \quad (3.8)$$

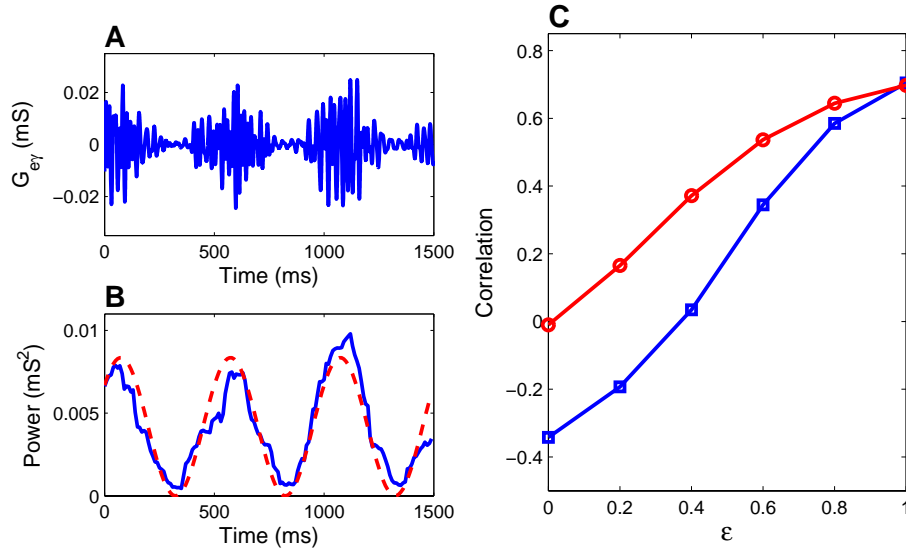


Figure 3.5.: Modulation of the γ -range conductance in the model neuron. A) γ -range component (25 – 70 Hz) of the excitatory conductance trace with a strong ($\epsilon = 1$) modulation. B) Relation between the expected modulation of the γ -power of the excitatory conductance (red dashed line) and the γ -power calculated from the trace in A) [solid line] using a running window of 102.4 ms duration. C) Linear coefficient of correlation (r) between the amplitude of the γ -range fluctuations and the slow changes of the membrane potential in the model neuron plotted against the strength of modulation of excitatory γ -range conductance (ϵ) for responses to a strong (blue square line) and a weak (red circle line) stimuli.

In eq. (3.8), ϵ determines the degree of modulation ($\epsilon \in [0, 1]$). Since the modulation affects the standard deviation of $g_{e0}(t)$, we included an additional parameter β , which allowed to compensate for the change of the standard deviation of $g_{e0}(t)$ and to bring it back to the same value as in the original trace without modulation. The phase of the gamma-modulation was adjusted to match the phase of the stimulus.

Figure 3.5A shows an example trace of the γ -frequency component of the excitatory conductance $g_e(t)$, with a strong modulation ($\epsilon = 1$) of the amplitude of the γ -range fluctuations. In Fig. 3.5B, the running average of the γ -power (blue solid line), calculated in a sliding window of 102.4 ms, is compared to the expected modulation of the γ -power (red dashed line). The measured modulation of the γ -power is in good agreement with the expectation. However, even the strongest ($\epsilon = 1$) modulation of the γ -power of excitatory conductance led to a smaller than 1 correlation between the

amplitude of the γ -range fluctuations and the slow depolarizations in the membrane potential ($r = 0.9$ for the example in Fig. 3.5A and B).

Several factors contributed to the reduction of the correlation in the membrane potential trace compared to the actual modulation of the conductance. Apart from the low pass filter property of the neuron, the calculation procedure contributed as well. The estimate of the correlation coefficient depends on the duration of the sliding window used for the calculation of the running average of the γ -power. Too short a window gives unreliable estimates of the γ -power, while for too long a window the assumption of constant stimulus does not hold. With the stimulation frequencies used in our study (0.5 to 2.5 Hz), maximal values were obtained with a running window of about 100 ms duration. However, even with this optimal window length the correlation coefficient was 0.9 for a perfectly correlated signal.

One further factor contributing to the reduction of the correlation in the membrane potential traces is a shunting effect of the slow changes of the input conductance and thus of the input resistance of the neuron at temporal frequency of stimulation. During the positive, depolarizing phase of the response to stimulation, when the γ -range conductances have higher amplitudes, the total input conductance is also larger, leading to a stronger shunting. As a result, high-amplitude γ -range conductances will be subject to a stronger reduction by shunting during the translation into membrane potential fluctuations, than low-amplitude γ -range conductances. Thus, low-frequency, stimulus-induced modulation of the input conductance counteracts the modulation of the amplitude of the γ -range fluctuations. Figure 3.5C illustrates the relation between the conductance modulation (ϵ) and measured correlation (r) between the γ -power and slow depolarizations in the membrane potential for the strong (e.g. optimal; blue square line) and weak (e.g. non-optimal; red circle line) responses. Figure 3.5C shows that strong stimulation has a stronger reducing effect on the measured correlation, and can lead even to negative values of the correlation coefficient.

Figure 3.6 illustrates membrane potential traces of the model neuron for optimal (Fig. 3.6A-C) and non-optimal (Fig. 3.6D-F) orientation and their analysis, which was done in exactly the same way as the analysis of intracellular recordings in visual cortex neurons (see Fig. 3.1). The simulated traces reproduce well the properties of those recorded. The simulated and the recorded responses have similar amplitudes of the slow modulation and the γ -range fluctuations of the membrane potential, as well as the correlation between the amplitude of the γ -range fluctuations and the phase of the slow modulation. To obtain in the membrane potential traces the values for correlation coefficient similar to those observed in the experiment, we had to introduce strong conductance modulation ($\epsilon > 0.9$) for the optimal response. At non-optimal

3. γ -Band Membrane Potential Fluctuations and Stimulus Encoding

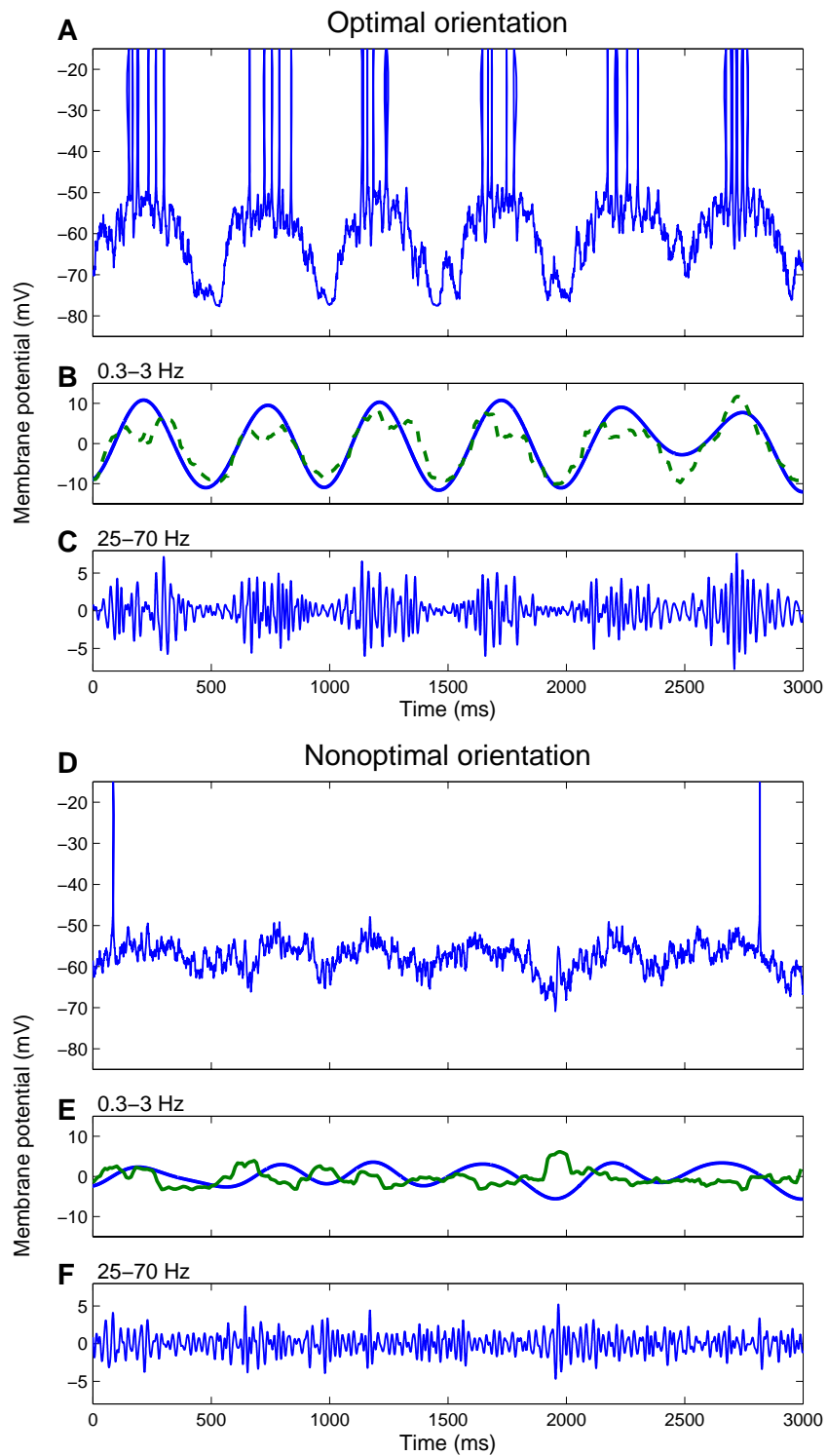


Figure 3.6.: Simulated responses of the model neuron to optimal (A) and non-optimal (D) orientation and their analysis. The spectral composition of the simulated traces was adjusted to match the spectral composition of the responses recorded in the cell in Fig. 3.1. A) and D) Simulated membrane potential traces. Temporal frequency of the moving grating was 2 Hz . Action potentials are truncated. B), C) and E), F) Analysis of the relation between the low frequency component [$0.3 - 3\text{ Hz}$, solid lines in B) and E)] and the high frequency, γ -range component [$25 - 70\text{ Hz}$, C) and F)] from the traces in A) and D). In B) and E) dashed lines show the power of the γ -range fluctuations estimated in a running window of 102.4 ms . Note that the γ -power (dashed) curves are normalized to match the amplitude of the respective low frequency components.

orientation, lower values of ϵ , between 0.3 and 0.5 were sufficient to reproduce the correlation seen in the experimental data.

Despite an overall similarity to the recorded membrane potential responses, the simulated traces have slightly different shapes of the slow depolarizations. In the simulations, the depolarization peaks are somewhat broader due to a cut off, which occurred because a substantial part of the stimulus was supra-threshold. The correspondence of the shape of depolarization peaks to the recordings could have been recovered by decreasing the average membrane potential. However, this would also lead to a substantial reduction of the average firing rate of the model neuron. Since stimulus encoding depends strongly on firing rate, we opted for obtaining in the simulations the similar firing rates, but slightly deviating from the recorded shapes of the slow depolarizations.

3.3.3. γ -Band Membrane Potential Fluctuations and Stimulus Encoding

Using the neuron model described above, we studied the influence of the high frequency membrane potential fluctuations, dependence of their strength on stimulus optimality, and modulation of their amplitude by slow membrane depolarizations on orientation tuning of spike responses and neuronal encoding. To this end, we simulated and analyzed responses to stimuli of different orientations/directions of movement for three classes of inputs. In the first class, only the low frequency stimulus power was adjusted to fit the experimentally observed values. This class will be referred to as *stimulus alone*. In the second class, in addition to stimulus-power, also the γ -power increase with stimulus optimality was implemented. In this class, *unmodulated gamma*, the γ -power was adjusted to the experimentally observed values, but was not modulated

with the slow membrane depolarizations ($\epsilon = 0$). In the third class, *modulated gamma*, in addition to the stimulus and γ -power, also the modulation of the amplitude of the γ -range fluctuations by slow membrane depolarizations was adjusted to the experimental values. For this latter adjustment we used ϵ values between 0.3 and 1, so that the correlation coefficients calculated for the simulated responses were similar to the experimentally observed values.

Orientation tuning of the model neuron

Figure 3.7 shows orientation tuning of different parameters in the model neuron for the three classes of inputs (solid lines, color coded), and compares the simulations with the data from the recorded visual cortex neuron (black dashed line). In Fig. 3.7A, stimulus-power of the membrane potential is plotted against the direction of stimulus motion. With all three classes of inputs, simulation results reproduce the experimentally observed data well. For most of the orientations, the simulation results essentially coincided with experimental data, and in all cases deviated by less than 5%.

Figure 3.7B compares the γ -power in the simulations and recorded neuron. Most pronounced deviations from the experimental data were observed in the *stimulus alone* simulation, in which only the stimulus power was adjusted to the experimental data (blue square line). Interestingly, even in this case the γ -power increases slightly with stimulus optimality. This increase was due to the fact that in the model, the power spectra of the membrane potential traces for different orientations is generated from the optimal and non-optimal spectra by linear interpolation (see above, Fig. 3.4 and related text). In the two other scenarios, unmodulated gamma (green cross line) and modulated gamma (red diamond line), the increase of the γ -power with stimulus optimality was explicitly included in the model. In both latter cases, orientation dependence of the γ -power observed in the experiments was faithfully reproduced in the simulations.

Figure 3.7C shows the linear correlation coefficient between the amplitude of the γ -range fluctuations and the phase of the slow membrane depolarizations as a function of stimulus orientations. Here, only the most complete of the three models, with the modulated gamma (red diamond line), reproduced the experimental data. To achieve similar values of the correlation coefficient as observed experimentally, modulation of the excitatory conductance in the model had to be set in the range of $0.3 < \epsilon < 1$. Two other models, stimulus alone and unmodulated gamma (blue and green lines), fail to reproduce experimental data. In fact, in both cases, even negative correlations were observed for most orientations. This was due to the shunting effect of the stimulus

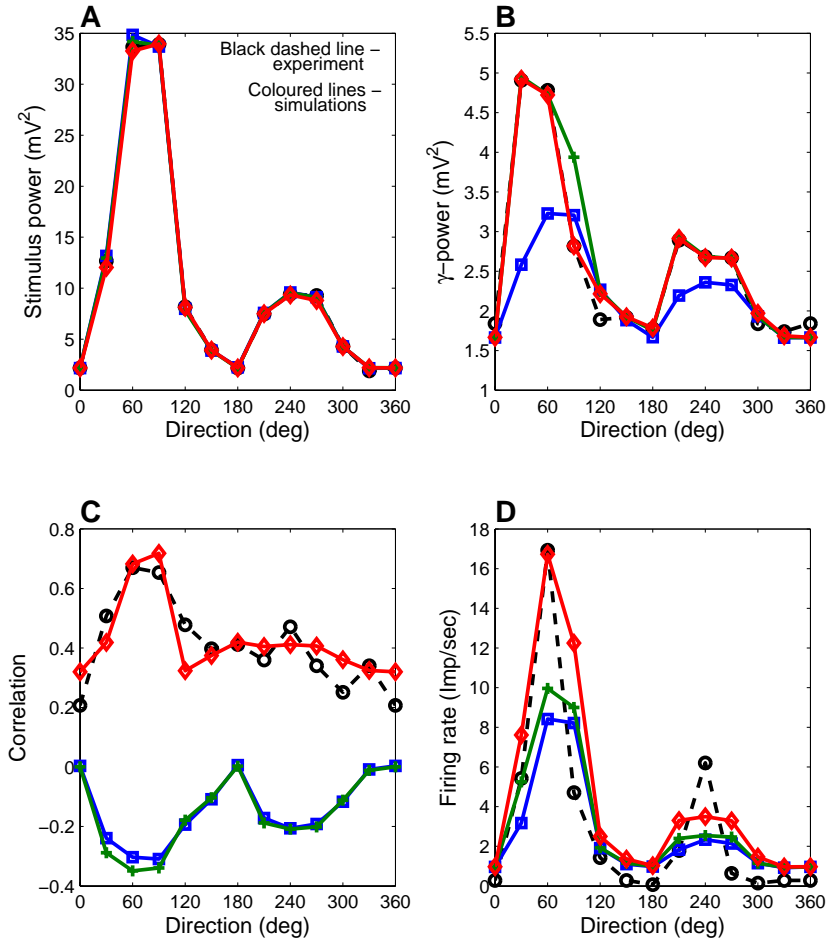


Figure 3.7.: Comparison of the features of the neuronal responses, recorded in the visual cortex, and of the simulated responses in the model neuron, which received inputs of three different classes. In A-D), circles and black dashed lines show recorded data (neuron from Fig. 3.1). Simulated data are shown in different colors for three types of inputs. Blue square lines: *stimulus alone* input with only stimulus power adjusted to fit the experimental data. Green cross lines: *unmodulated gamma* input, in which in addition to the stimulus-power, also the γ -power depended on stimulus optimality. Red diamond lines: *modulated gamma* input, in which in addition to the stimulus and γ -power, the modulation of the amplitude of the γ -range fluctuations by slow membrane depolarizations was also adjusted to the experimental values. All response features are plotted against the direction of grating movement. A) Strength of the low frequency fluctuations of the membrane potential (stimulus power). B) γ -power of the membrane potential responses. C) Correlation between the stimulus and the γ -power. D) Spike count.

conductance, which affected (reduced) the amplitude of unmodulated γ -range fluctuations most strongly during strong depolarizations, thus introducing the negative correlation (see Fig. 3.5 and related text above).

Figure 3.7D shows the spike tuning of the recorded cell and the models. The tuning of the recorded neuron is best reproduced by the most complete model, with the modulated gamma (red diamond line). Some minor deviations of the simulated spike response from the experimental data were due to the fact that in the recorded cell, the mean membrane potential was also changing as a function of stimulus orientation. This dependence was not implemented in the model, leading to small difference in firing rates at null orientation. In the simulations without the modulation of the γ -power, or *stimulus alone* (blue and green lines), the model neuron generated considerably fewer spikes. At optimal orientation the firing rate in these models dropped to about 50 – 60% of that in the recorded neuron and in the model with γ -power modulation. Comparison of the three models shows that the γ -range fluctuations of the membrane potential lead to a substantial increase in spike response, only if they were modulated in phase with the slow membrane depolarizations.

Results presented in Fig. 3.7 demonstrate that all three classes of input reproduce the low frequency modulation of the membrane potential at temporal frequency of stimulation and, if implemented, the properties of the high-frequency fluctuations fairly well. Differences in other parameters allow to make inferences on the contribution of the γ -range fluctuations to stimulus encoding.

Figure 3.8 compares the information rate in the model neuron and in the responses of the recorded cell. The information rate was highest for the simulations, which included the modulation of the amplitude of the γ -range fluctuations (red diamond line). At optimal orientation, the estimated information rate for the model neuron was even slightly higher than for the cell (black dashed line), despite the equal averaged firing rate. For the null direction of movement, information rate in the recorded cell was slightly higher. In the models without modulation (blue and green curves), the information rate was clearly lower than with modulation, which was an expected consequence of the lower firing rates. The percent decrease in information rate (to 60 – 70%), however, was not as strong as the decrease in firing rate (to 50 – 60%). Moreover, both models without γ -power modulation, had essentially same information rates, showing that addition of unmodulated γ -range fluctuations of the membrane potential has little effect on encoding. Thus, information encoding is improved only by modulated γ -range fluctuations, whereby higher information rates are due to the ability of the modulated γ -range fluctuations to facilitate stimulus-locked firing of neurons.

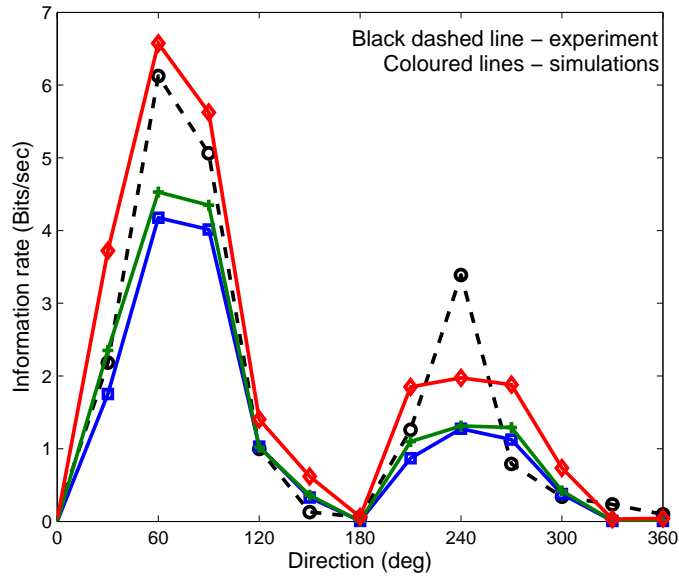


Figure 3.8.: Comparison of the information rate in the recorded and simulated responses. Circles and black dashed lines: recorded data, neuron from Fig. 3.1. Simulated data are shown in different colors for three types of inputs, as in Fig. 3.7. Blue square lines: *stimulus alone* input. Green cross lines: *unmodulated gamma* input. Red diamond lines: *modulated gamma* input. Information rate is plotted against the direction of grating movement.

γ -Activity Modulation and Stimulus Encoding

To further investigate the effect of the γ -activity modulation on stimulus encoding, we have used the most complete model, with stimulus-dependent low frequency modulation, stimulus-dependent γ -power modulation, and depolarization-dependent modulation of the γ -activity. In this model, we systematically changed the strength of the depolarization-dependent modulation of the γ -activity, while adjusting all other parameters to match the averaged values of our experimental data sample (Table 3.2).

Dependency of the information rate and the firing rate on the strength of γ -activity modulation with the phase of slow membrane depolarizations (ϵ) is shown in Fig. 3.9. A decrease of the modulation of γ -range conductance (ϵ) leads to a decrease of both the information rate and firing rate (Fig. 3.9A, solid lines). Interestingly with decreasing ϵ , the firing rate decreases slower, reaching 86% at $\epsilon = 0$ (blue solid line) than the information rate, which falls to 77% at $\epsilon = 0$ (red solid line).

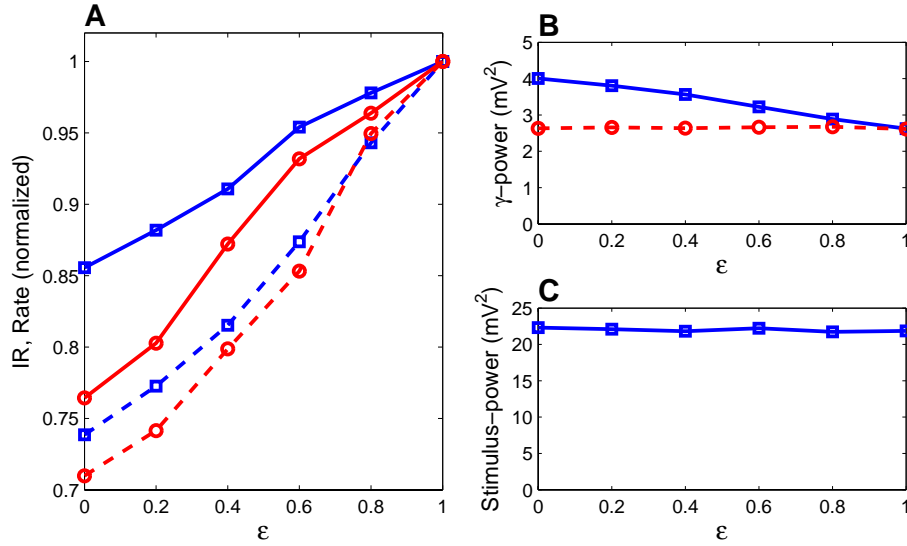


Figure 3.9.: Dependence of the information rate, the firing rate and the high (γ -range) and the low (stimulus) frequency power in the model neuron on the degree of modulation of the γ -band activity by the low frequency changes of the membrane potential (ϵ). A) Information rate and the firing rate plotted against the degree of the γ -band activity modulation in the model neuron with (dashed lines) and without (continuous lines) keeping the total γ -power constant. A decrease of ϵ reduces both information rate (red solid curve) and firing rate (blue solid curve). The dashed lines show the corresponding values for the IR and firing rate, where the γ -band activity was kept constant at different values of ϵ . Information rate and firing rate are normalized to one at $\epsilon = 1$. B) γ -power of the membrane potential plotted against the degree of modulation ϵ (blue solid curve). The red (dashed) curve represents the γ -power of V_m for simulations, where the γ -power of the excitatory conductance was adapted to match the experimentally observed value. C) Stimulus power plotted against the degree of modulation (ϵ).

The slower decrease of the firing rate may be due to the fact that the decrease of ϵ actually leads to an increase of the total power of the γ -range fluctuations of the membrane potential as illustrated in Fig. 3.9B (blue solid line). When the amplitude of the γ -range fluctuations was strongly correlated with depolarization peaks ($\epsilon = 1$), the γ -range fluctuations are subjected to substantial shunting by the stimulus-induced high conductance. With decreasing correlation ($\epsilon < 1$), the power of the γ -range fluctuations of the excitatory conductance becomes redistributed towards the negative phases of the stimulus-induced depolarizations, and the γ -range fluctuations are less shunted by the stimulus conductance. As a result, the total power of the membrane potential fluctuations in the γ -band increases with decreasing ϵ . This increase of the total γ -band power of the membrane potential fluctuations explains the slower decrease of the firing rate in Fig. 3.9A. If we adjust the amplitude of the γ -range fluctuations in the model such that the total γ -power of the membrane potential fluctuations remains the same at all values of ϵ (Fig. 3.9B; red dashed curve), both the firing rate and the information rate decrease more substantially, but also more uniformly, with decreasing ϵ (Fig. 3.9A, dashed curves).

Changing the degree of modulation of the γ -power by the slow membrane depolarizations had only little effect on stimulus-power (Fig. 3.9C). A minor increase in stimulus power (solid line) with decreasing ϵ can be attributed to re-distribution of the γ -activity. With decreasing ϵ , some of the γ -range conductance is shifted away from the depolarization peaks, leading to a weaker shunting of the depolarization peaks, first, by the γ -range conductance itself, and second, due to lower firing rate, decreased shunting of depolarization by action potential-related conductances.

Factors Influencing Firing Rate and Stimulus Encoding

Information rate depends on firing rate, because each additional spike contains some information about the stimulus, and on the information content of each action potential, i.e. the precision of its relation to the stimulus. Thus, stimulus encoding may be changed either by varying the firing rate or the precision of the spiking. In the next series of simulations we investigated, how the firing rates and stimulus encoding are affected by variation of the amplitude of the low frequency, stimulus-related modulation of the membrane potential, and by variation of the power of the membrane potential fluctuations in the γ -range. For both these parameters, we used the ranges of variability seen in the experimental data, and modified them by plus-minus one standard deviation from the mean (see Table 3.2). We compared the behaviour of two models, the first one with complete modulation of the γ -range power by slow membrane depolarizations ($\epsilon = 1$), and the second one with un-modulated γ -range activity

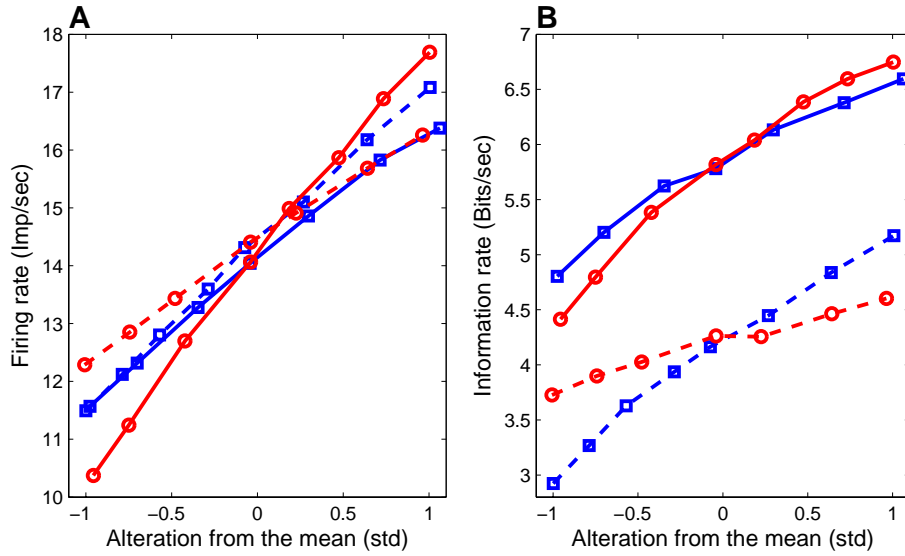


Figure 3.10.: Dependence of the firing rate (A) and the information rate (B) on alteration of the stimulus-power (blue square curves) or the γ -power (red circle curves). Both, the stimulus and the γ -power were altered plus-minus one standard deviation from the mean values measured in visual cortex neurons (see Table 3.2). Solid lines: Model with complete modulation of the γ -power by slow membrane depolarizations ($\epsilon = 1$). Dashed lines: Model with un-modulated γ -power.

($\epsilon = 0$).

In Fig. 3.10A, the firing rate is plotted against the changes of the stimulus-power or the γ -power. In both models, alteration of either the stimulus or the γ -range power led to changes of the firing rate. However, the firing rate was affected most strongly by changing the γ -power in the complete model with the slow depolarization-modulated γ -range activity (red solid line). This is indicated by the bigger range of the firing rate changes (10.3 Hz to 17.7 Hz) and the maximal slope of the respective regression line [3.7 Hz per std, as compared to 2.4 Hz per std (blue solid curve), 2.8 Hz per std (blue dashed curve) and 2.0 Hz per std (red dashed curve) for the three other cases].

Figure 3.10B shows dependences of changes of the information rate on the alteration of the stimulus-power or the γ -power for the two models (same simulations as in Fig. 3.10A). Figure 3.10B demonstrates two important points. First, information rates were systematically higher in the model with the γ -range activity, modulated by the slow membrane depolarizations. This is illustrated by the fact that the solid lines,

which represent the data obtained with the modulated-gamma model, are located higher than the dashed lines, which represent data from the model with un-modulated gamma. Second, in the model with modulated-gamma, alteration of the γ -power has a stronger effect on stimulus encoding, than alteration of the low frequency stimulus-power. This is indicated by the broader range of the information rates covered (4.4 to $6.7 \frac{\text{bits}}{\text{sec}}$, and steeper slope of the dependence on the input alteration ($1.19 \frac{\text{bits}}{\text{sec}}$ per std), of the respective data [compare red and blue solid lines].

Taken together, these results show that alternation of the γ -band activity at the input to the neuron represents the most effective way of changing the rate of its firing and the stimulus encoding, and that the model with modulated gamma provides the most efficient encoding of the stimulus.

3.4. Discussion

Main results of the present study are the following. (i) Analysis of our intracellular recordings from visual cortex neurons showed that the difference between membrane potential responses to the optimal and non-optimal stimuli is most pronounced in two frequency ranges: at low frequencies around temporal frequency of the stimulation and at high frequencies, in the γ -range and above ($20 - 200 \text{ Hz}$). Furthermore, the amplitude of the γ -range fluctuations correlated with the phase of the low frequency membrane potential changes. Our simulations showed that (ii) stimulus encoding was substantially improved by the modulation of the amplitude of the high frequency fluctuations by the phase of low frequency changes of the membrane potential; (iii) changing the degree of modulation of the γ -activity by the low frequency signal clearly had a stronger effect on both the firing rates and information rates than changing the amplitude of the low-frequency stimulus itself; (iv) non-modulated, uniform γ -activity lead to only a moderate enhancement of the firing rates, information rates, and improvement of encoding as compared to the *stimulus-alone* condition, in which only the amplitude of the low frequency stimulus itself was varied.

Electrophysiological Results

We have selected for the analysis only visual cortex neurons with simple-type receptive fields, with clear modulation of the membrane potential and firing at temporal frequency of the stimulation (Dean and Tolhurst, 1983; Scottun et al., 1991; Carandini and Ferster, 2000; Volgushev et al., 2003). We did not consider here neurons with complex receptive fields, in which temporal frequency of the stimulation is reflected

little in the modulation of the membrane potential and firing. Because of the difference in the response modulation, simple cells are much better suited for encoding temporal structure of stimuli, than complex cells.

Our previous study showed that γ -band fluctuations of the membrane potential are a common property of visual cortex neurons, present in both simple and complex cells (Volgushev et al., 2002, 2003). In the simple cells, the amplitude of the γ -band fluctuations correlated with the phase of the low frequency, stimulus-induced membrane potential changes, being maximal at depolarization peaks and minimal at hyperpolarization troughs of the membrane potential responses (Volgushev et al., 2003). Results of the present study confirm and extend these findings. We have used now an improved measure of the relation between the high frequency fluctuations and the slow changes of the membrane potential – correlation between the low frequency component and the running average of the power of the high frequency fluctuations. This measure gives better estimation of their relation and higher correlation values than the envelope-based method used in our previous study. A further important advantage of this measure is that it can be better formalized and thus used as a variable (and also as a constraint) in the simulations.

We have found that difference in the spectral composition of membrane potential responses to presentation of the optimal and non-optimal stimuli is most pronounced in two ranges: the low ($< 4 Hz$) and the high ($20 - 200 Hz$). The difference between the optimal and non-optimal responses in the low frequency range, around temporal frequency of stimulation is present in simple cells by definition. More interesting is that the difference becomes less at intermediate frequencies ($5 - 20 Hz$), but increases again to several-fold in the γ -band and higher ($20 - 200 Hz$). The decreased difference in the middle-range indicates that the stronger high frequency fluctuations of the membrane potential during the optimal stimulation were not due to high-order harmonics of the stimulation frequency. Rather, high frequency fluctuations might reflect a genuine temporal structure of the input activity. Together with such features of the γ -band fluctuations as their abilities to make generation of action potentials more reliable (Mainen and Sejnowski, 1995; Nowak et al., 1997; Volgushev et al., 1998, 2003; Salinas and Sejnowski, 2000), produce precise temporal patterns of activity (Mainen and Sejnowski, 1995; Nowak et al., 1997) and impose precise temporal windows for synaptic integration (Lampl and Yarom, 1993; Volgushev et al., 1998), the stronger contribution of high-frequencies to the optimal responses may indicate an interesting possibility that most relevant information in neuronal networks (e.g. presence of the optimal stimulus in the receptive field) is transmitted by the γ -band activity. This possibility fits also well to the long-suggested role of γ -band fluctuations in synchronizing activity of neuronal ensembles and binding the descriptions of an object (Eckhorn

et al., 1988; Gray and Singer, 1989; Singer, 1993, 1999).

Simulated Responses of the Model Neuron: What they Reproduce and what they Show

Simulated responses of the model neuron to different orientations of moving gratings reproduced the membrane potential traces, their spectral composition as well as other implemented features well.

Simulations clearly reveal mutual shunting effects between the low (stimulus) frequency and the high frequency fluctuations. Due to the shunting by the stimulus-frequency changes in membrane conductance, the high frequency fluctuations of conductance are translated into membrane potential changes non-uniformly, with stronger shunting during peaks of slow depolarizations. One further factor, masking the relation of the membrane potential changes to the underlying conductances is a non-linear – either sublinear or supra-linear – summation of synaptic inputs impinging onto the neuron (Häusser et al., 2000). These factors impose limitations on the reliability of measurements of the correlation between the low frequency depolarizations and the amplitude of high frequency fluctuations of the membrane potential. In the simulations, we had to implement a much stronger modulation of high-frequency conductances to reproduce the values of correlation coefficients seen in the recordings. This indicates that the real difference between the depolarization peaks and hyperpolarization troughs in the strength of γ -range conductance might be even higher than assessed from the membrane potential traces. An implication of these simulation results is that the γ -power is clearly non-evenly (non-randomly) distributed between slow depolarizations and hyperpolarizations – otherwise the shunting by the low frequency conductance changes should have led to a negative correlation, which we never observed in the recordings. This points towards an intrinsic relation between the γ -band activity and low frequency depolarizations and is compatible with the abovementioned possibility that it is an inherent property of the activity in neuronal networks, to be γ -structured.

Comparison of the simulated responses of the model neuron subject to three different classes of inputs (*stimulus alone*, *unmodulated gamma*, and *modulated gamma* – see Sec. 3.3 for details) showed that only the most complete model, with the γ -activity modulated by the phase of slow depolarizations, faithfully reproduced the firing rates and information rates, seen in the recorded neuron. In contrast, both types of inputs without modulated γ -activity, the stimulus-alone and the unmodulated gamma, produced similar firing rates and information rates in the model neuron, well below the recorded data. Thus, the γ -activity as such, without being modulated by the phase of

stimulus-frequency depolarizations, brings about little enhancement of the firing and little improvement of the encoding.

Of course, unmodulated γ -activity at the input could still be useful for detection of weak stimuli, causing an effect similar to stochastic resonance (Anderson et al., 2000a; Volgushev and Eysel, 2000; see Moss et al., 2004 for a review). However, this effect does work in only a relatively narrow range of the relations between the threshold, the amplitude of the high frequency fluctuations (*noise* in stochastic resonance) and the stimulus strength. Apparently, the real values, which we measured in the recorded neurons and implemented in the model, were outside that range. With the measured ranges of parameters, modulation of the γ -activity by the stimulus-frequency membrane depolarization resulted in the substantial increase of the firing rates and improvement of the stimulus encoding.

Limitations of the Model

Several limitations of our model are worth mentioning. First, modulation of the γ -activity in the model was implemented by modulating the excitatory conductance only. In reality, γ -band fluctuations might originate from precise temporal organisation of excitatory and inhibitory inputs/conductance, with possible additional contribution of intrinsic membrane mechanisms of some cells (Jagadeesh et al., 1992; Jahnsen and Karnup, 1994; Gutfreund et al., 1995; Gray and McCormick, 1996; Hutcheon et al., 1996; Bringuier et al., 1997; Lampl et al., 1999). However, since the aim of our study was to investigate how the stimulus encoding is influenced by the presence of high frequency fluctuations and their relation to the low frequency stimulation, the exact mechanism with which the fluctuating conductance was produced was of little importance. In fact, in our model, introducing fluctuations of inhibitory conductance in addition to the excitatory did not influence encoding unless the total power of the γ -band fluctuations was affected. This also shows the robustness of our results with respect to the detailed mechanisms of the high frequency fluctuations.

Second, spectral composition of the membrane potential, resulting from the spatial and temporal integration of numerous synaptic inputs impinging on the dendrites, equipped with active ionic conductances is not necessarily Gaussian or filtered Gaussian as implemented in our model. Moreover, it might be possible to adjust the spectral composition of the simulated membrane potential traces to those recorded with a different combination(s) of stochastic processes, than the one we have used. However, Destexhe et al. (2001) demonstrated that filtered Gaussian provides a reasonably good approximation of membrane potential fluctuations, therefore we opted for this easily tractable mathematical generation of conductances.

Finally, we have used for simulations a conductance-based model with Hodgkin-Huxley type channels. Since stimulus encoding in model neurons depends on the properties of the action potential generation mechanism (Fourcaud-Trocm et al., 2003; Naundorf et al., 2005), we have adjusted parameters of the kinetic equations to achieve a better correspondence between the simulated and the recorded action potentials. Although recent study have demonstrated that the Hodgkin-Huxley type models cannot describe precisely the initiation dynamics of cortical action potentials (Naundorf et al., 2006), there is still no simple and approved model available for an alternative description. For that reason, we decided to use the Hodgkin-Huxley type model with *tuned* channel kinetics. Moreover, since rapid dynamics of action potential initiation is beneficial for the encoding of fast signals (Naundorf et al., 2006), such as γ -range fluctuations, it may even facilitate the effects of fast membrane potential fluctuations on stimulus encoding, reported here.

Modulated γ -Band Activity and Stimulus Encoding

Fast, γ -band fluctuations of the membrane potential possess several features, which make them especially well-suited to subserve synchronisation of neuronal activity and/or binding of object representations (Eckhorn et al., 1988; Gray and Singer, 1989; Singer, 1993, 1999). To these features of the γ -band fluctuations belong the ability to support reliable spike generation, impose precise temporal windows for synaptic integration and produce precise temporal patterns of activity (Lampl and Yarom, 1993; Mainen and Sejnowski, 1995; Nowak et al., 1997; Volgushev et al., 1998, 2003; Salinas and Sejnowski, 2000).

Our earlier results indicated that γ -band fluctuations may also modify the gain at which membrane depolarizations are translated into spike responses (Volgushev et al., 2002), and that the strongest γ -fluctuations are associated with the peaks of slow membrane depolarizations (Volgushev et al., 2003, 2004). We suggested that the modulation of the amplitude of the γ -band fluctuations by the phase of the low frequency membrane potential changes might improve stimulus encoding (Volgushev et al., 2003, 2004). Theoretical results by Lindner and Schimansky-Geier (2001) support this suggestion. They have shown that the modulation of the noise intensity is an efficient way to transmit signal through neural ensembles. Here we show that the modulation of the amplitude of the γ -range fluctuations within the experimentally observed range can indeed lead to a higher information transmission efficiency. With the modulated-gamma input, the model neuron reproduced both the firing rates and information rates of the recorded cells most closely. This was not the case for the input with non-modulated (i.e. independent of the slow depolarization) γ -activity, or

the input with only low (stimulus) frequency depending on orientation.

Firing of the model neuron showed clear and strong dependence on the degree of γ -modulation, either when the modulation influenced the total γ -power due to shunting effects of the low frequency depolarizations (see results), or when the model was compensated for that shunting, and the total γ -power remained constant. Furthermore, the degree of modulation of the γ -activity had an even stronger effect on both the firing rate and the information rate, than variation of the strength of the low frequency input itself, implemented in the model as changes of the amplitude of the low (stimulus) frequency component.

Thus, not just the net depolarization, but also the fine temporal structure of the input is critical for producing high-frequency responses and for transmission of information at high rates. In turn, precise temporal organisation at the inputs might produce a precisely patterned spike output of the cells, and thus precise temporal pattern of activity at the inputs to the next-level neurons. Taken together, these properties allow the γ -band activity not only to improve stimulus encoding in every single neuron, but also to facilitate propagation of the encoded information through multiple processing layers of the neuronal network.

4. Neural Information Transmission

4.1. Introduction

In the introduction of this thesis we have discussed that a basic feature of spike trains observed in many experiments *in vivo* is the high degree of variability arising from the background activity, which is permanently present in the cortex (Destexhe and Pare, 1999; Destexhe et al., 2003). This fluctuating activity can significantly influence the information transmission properties of cortical neurons by making transmission fast (Tsodyks and Sejnowski, 1995; Silberberg et al., 2004) or by allowing the transmission of otherwise subthreshold signals, for example through stochastic resonance (Bulsara et al., 1991; Longtin, 1993). Stochastic resonance is a phenomenon in which the transmission of a signal - measured for example by the mutual information between input and output - becomes optimal for a certain noise level, which depends on the properties of the distribution of the input signal.

Since stochastic resonance was proposed as a possible explanation of the periodicity of the ice ages (Benzi et al., 1981; Nicolis, 1982), it has been shown that stochastic resonance is fundamental in many physical, chemical, and biological processes [for a general review on stochastic resonance see Gammaitoni et al. (1998)]. For stochastic resonance to occur, a neural system has to be non-linear (bistable system) and the driving input has to consist of a weak (subthreshold) signal and a stochastic force (noise). Neural systems are both strongly nonlinear, e.g. they possess a threshold for action potential generation, and they are subjected to many noise sources, which are either external or intrinsic (cf. Sec. 1).

Unsurprisingly, it was recognized early that stochastic resonance may also play a major role in neural information processing. Over the last two decades, stochastic resonance in neural systems has been investigated, both theoretically (Bulsara et al., 1991; Longtin, 1993; Wiesenfeld and Moss, 1995; Lindner and Schimansky-Geier, 2001; Rudolph and Destexhe, 2001; Hoch et al., 2003) and experimentally (Douglas et al., 1993; Collins et al., 1995; Simonotto et al., 1997; Russell et al., 1999; for a review see Moss et al., 2004). These studies concluded that there is strong evidence for stochastic resonance in the sensory and peripheral nervous system. Nevertheless, it is still unclear

to what extent stochastic resonance plays a role in the central nervous system of higher animals.

Maximal information transmission, however, may not be the only goal neurons try to achieve. Neural activity is costly in metabolic terms, and energy consumption and dissipation becomes a concern, for example for the densely packed central nervous system of higher animals. Several researchers have suggested that the overall energy consumption constrains information transmission, and it has been argued that neurons try to achieve a balance between information transmission and energy consumption, leading to energy efficient codes (Levy and Baxter, 1996; Laughlin et al., 1998; Balasubramanian et al., 2001; de Polavieja, 2002; Hoch et al., 2003). Energy efficient codes favor many parallel low intensity pathways (Laughlin et al., 1998). Indeed, recent studies on the energy consumption of the cortex have suggested that the average firing rates of cortical neurons might be less than 1 Hz (Attwell and Laughlin, 2001; Lennie, 2003). Such low firing rates are typical for weak (subthreshold) signals, which raises the hypothesis that stochastic resonance is a useful mechanism for low cost information transmission.

In the following, we explore the complex relationship between information transmission, energy consumption and background activity. Using a leaky integrate-and-fire neuron, we show that noise can enhance information transmission substantially if the input signal is subthreshold. Nevertheless, information rates are much higher for supra-threshold signals and we show that the addition of noise always deteriorates information transmission for such signals. The transmission of signals in the supra-threshold regime, however, is also accompanied with high firing rates of the neurons involved. Thus the question arises as to why cortical cells favour low firing rates (Olshausen and Field, 2005). After including metabolic constraints we find that optimal information transmission in terms of information rate per unit cost occurs mainly in the subthreshold regime, where neurons can exploit the membrane potential fluctuations to maximize information transmission (stochastic resonance). Thus we conclude that in the central nervous system of higher animals, information is likely to be coded using low firing rates and populations of cells, similar as it was proposed for cells in the blowfly retina (Laughlin et al., 1998).

4.2. Materials and Methods

We consider a leaky integrate-and-fire (LIF) neuron. For a detailed description of the LIF model see Sec. 2.2.1. The membrane potential V of the leaky LIF neuron changes

in time according to the following differential equation:

$$\tau_m \frac{dV(t)}{dt} = (E_L - V(t)) + \frac{I_{stim}(t)}{g_L} + D \frac{dW(t)}{dt}, \quad (4.1)$$

where $\tau_m = 10 \text{ ms}$ is the membrane time constant, $g_L = 0.05 \mu\text{S}/\text{cm}^2$ is the leak conductance of the membrane, $E_L = -70 \text{ mV}$ is the reversal potential, $I_{stim}(t)$ is the external signal, and $dW(t)$ is the infinitesimal increment of a Wiener process, which describes the influence of the background activity on the membrane potential (see Sec. 2.2 for more details about the LIF and the noise model). In this study we used an aperiodic Gaussian signal $I_{stim}(t)$, which is generated by Fourier transforming a band-limited white noise power spectrum to time domain. The lower and upper cut-off frequency were $f_{low} = 2 \text{ Hz}$ and $f_{high} = 5 \text{ Hz}$, respectively.

To characterize stochastic resonance, we estimated the information between the input signal and the neural response with the help of the linear reconstruction method (see Sec. 2.4.2 for more details). The information rate is obtained with the following equation (Borst and Theunissen, 1999):

$$I_{lin} \geq -\frac{1}{2\pi} \int_0^\infty \log_2 [1 - \gamma^2(\omega)] d\omega, \quad (4.2)$$

where $\gamma^2(\omega) = \frac{|P_{SR}(\omega)|^2}{P_{SS}(\omega)P_{RR}(\omega)}$ is the coherence between the stimulus and the response, $P_{SS}(\omega)$ and $P_{RR}(\omega)$ are the power spectra of the stimulus and the spike train, and $P_{SR}(\omega)$ denotes the cross power spectrum between the stimulus and the spike train.

The coherence $\gamma^2(\omega)$ was calculated as follows. Stimulus and spike response were divided into segments of 819.2 ms duration (with an overlap of 50%). All segments were then transformed into Fourier space, multiplied by their complex conjugate, and averaged at each frequency to yield the estimate of the power spectrum (P_{XX}) and the cross power spectrum (P_{XY}), e.g. $P_{XY}(\omega) = \langle X(\omega)Y(\omega)^* \rangle$, where $*$ denotes the complex conjugate and $\langle \rangle$ denotes the averaging over segments. All simulations were done using the Euler integration scheme with an exact update equation (Gillespie, 1996) and had a duration of 200 sec . The simulation time step was set to $dt = 0.1 \text{ ms}$.

4.3. Results

4.3.1. Stochastic Resonance

Here we investigate the role of noise on the dynamics of subthreshold input signals. When a noisy current is injected into the neuron, stochastic resonance occurs and

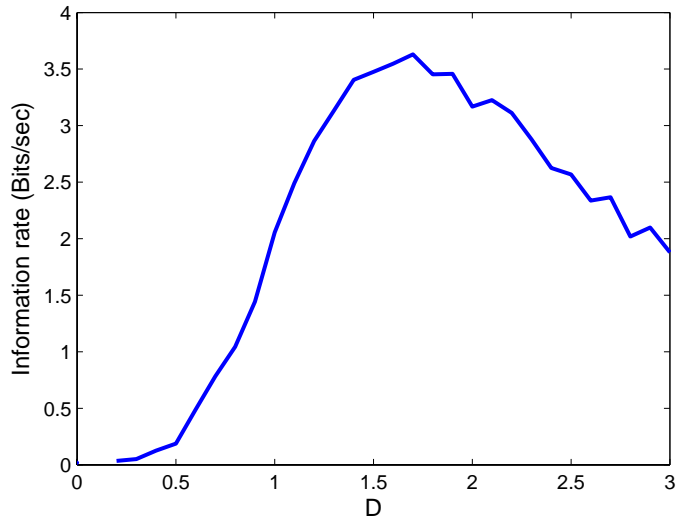


Figure 4.1.: Stochastic resonance-like behavior of the leaky integrate-and-fire neuron. The Fig. shows the information rate calculated from eq. (4.2) plotted as a function of the noise level D . The bias current was set to $I_{bias} = 0.6 nA$ and standard deviation of the input signal was $0.1 nA$.

the transmission of subthreshold input signals is enhanced. Figure 4.1 shows the stochastic resonance like behavior of a leaky integrate-and-fire neuron. The Fig. shows the information rate plotted against the noise level. Without noise, the input signal is too weak to evoke a response and, therefore, no information can be transmitted. An increase of the noise level due to a higher value of D in eq. (4.1) leads to fluctuating membrane potential, which occasionally initiates action potentials. In the beginning, information rate increases fast with increasing D , because the stronger fluctuating membrane potential evokes more spikes allowing the transmission of more information about the stimulus. A higher noise level, however, leads not only to higher firing rates of the neuron, but also reduces the information that the action potential contains about the stimulus. Thus, the beneficial increase of the firing rate is counterbalanced by less informative action potentials leading to a decrease of the information rate at high noise levels, as Fig. 4.1 shows. Nevertheless, there exists an optimal amount of noise, which maximizes information transmission.

This optimal noise level depends on the statistic of the input signal and on the distance between the average membrane potential and the spike threshold, as Fig. 4.2 indicates. The Fig. shows the information rate as a function of the noise level D for four different bias currents. The blue line corresponds to simulations with a bias

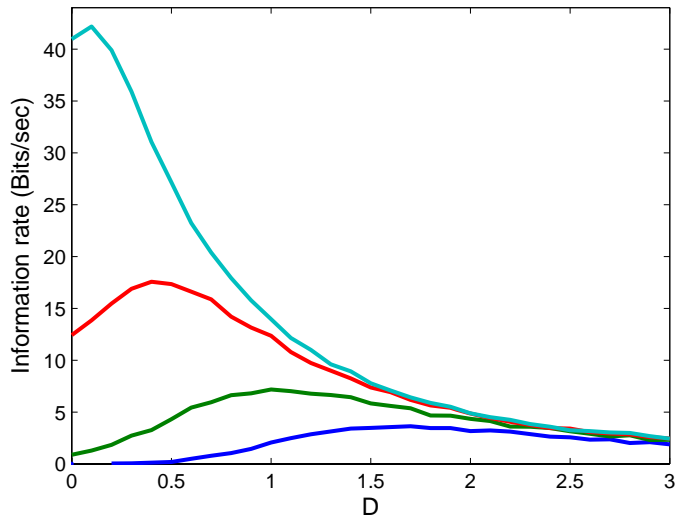


Figure 4.2.: Dependency of the stochastic resonance phenomenon on the strength of the input signal, expressed by the bias current. The blue line represent a weak signal ($I_{bias} = 0.6 nA$), where as the cyan line corresponds to stimulation with a strong signal ($I_{bias} = 1, 1 nA$). The green and the red line represent intermediate values of I_{bias} , e.g. $I_{bias} = 0.75 nA$ and $I_{bias} = 0.9 nA$, respectively. The standard deviation of the input signal was $0.1 nA$.

current of $I_{bias} = 0.6 nA$, which leads to an average membrane potential (without spike process and reset) of $\langle V_m \rangle = -58 mV$. For this bias current the input signal is totally subthreshold. An increase of the bias current to $I_{bias} = 0.75 nA$ (green line; $\langle V_m \rangle = -55 mV$) or $I_{bias} = 0.9 nA$ (red line; $\langle V_m \rangle = -52 mV$) leads to an average membrane potential, which remains just below spike threshold. For a bias current of $I_{bias} = 1.1 nA$, the input signal is mainly supra-threshold (cyan line). Figure 4.2 shows nicely that information transmission is greatly improved only in the subthreshold regime ($I_{bias} \leq 1 nA$). At small values of I_{bias} , the distance to the spike threshold is increased and a stronger fluctuating membrane potential is needed in order to evoke a response. Thus, information transmission is optimal at higher noise levels. Conversely, for a given noise level information transmission is optimized, if the neuron lowers its threshold. At high noise levels ($D > 2$), however, the information rate only weakly depends on the distance to threshold, as Fig. 4.2 indicates.

4.3.2. Energy Efficient Information Transmission

Information transmission in the brain is metabolically expensive (Laughlin et al., 1998, Attwell and Laughlin, 2001; Lennie, 2003). In particular, the generation of spikes consumes a huge amount of energy. If the cost of firing is high in comparison to the *housekeeping* cost, then it is advantageous for the brain to use energy efficient neural codes (Levy and Baxter, 1996; Laughlin et al., 1998; Balasubramanian et al., 2001; de Polavieja, 2002; Hoch et al., 2003). Given a fixed amount of energy, there are several ways to achieve energy efficient information transmission. One strategy is to use an input distribution so that the energy constraint can be fulfilled (Hoch et al., 2003). Another strategy is to maximize the information rate per metabolic cost to transmit as much information as possible. In the following we will take a closer look at the latter.

Information Rate per Metabolic Cost

As a measure of metabolic efficiency we consider the ratio between the transmitted information R_{info} and the total metabolic cost E . We assume that the average metabolic cost E per unit time is a sum of a term proportional to the average rate \bar{r} of the neuron and a term which contributes a fixed baseline cost b . The baseline cost represents the metabolic expense of maintaining a neuron. We set

$$E = c(b + \bar{r}), \quad (4.3)$$

where c is a proportionality constant, which can be interpreted as the average cost per spike. Both information rate and average cost change with the actual noise level. To investigate the relationship between the average membrane potential, the noise level and the information rate per unit cost I_E , we vary the bias current I_{bias} and the noise level of the neuron.

Figure 4.3 shows the normalized information rate per unit cost for different baseline cost ($b = 0$ thick solid line, $b = 5$ thick dotted line, $b = 20$ thin solid line, $b = 100$ thin dotted line) plotted against the bias current. In Fig. 4.3A the noise level of the LIF neuron was set to $D = 0.2$ and in Fig. 4.3B to $D = 0.5$. If metabolic costs are taken into account, the maximum of I_E is shifted to lower values of I_{bias} . This is due to the fact that high energy costs favor low output rates, which - in turn - can be achieved if the distance to the threshold is increased. An increase in the baseline costs b leads to a shift of the maximum of I_E to higher values of I_{bias} , because the smaller dependency of the total cost on the output activity \bar{r} allows for higher output rates. In the limit of

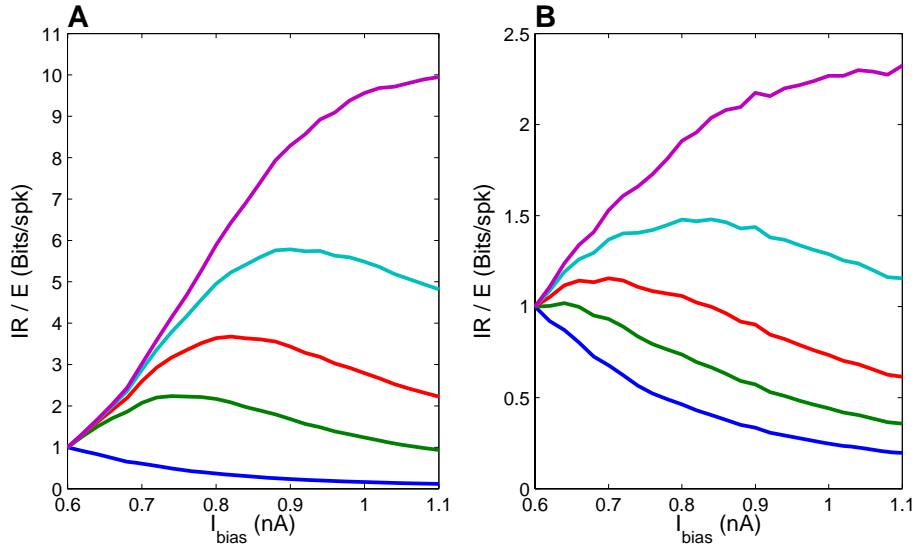


Figure 4.3.: Information rate per cost I_E plotted against the bias current for different baseline costs ($b = 0$: blue line; $b = 1$: green line; $b = 3$: red line, and $b = 10$: cyan line). The black line is the information rate per cost for the limit of large baseline costs. In A) the noise level of the LIF neuron was set to $D = 0.9$ and in B) to $D = 1.5$.

large baseline costs, the activity dependent costs ($\bar{r}N$) can be neglected, and optimal information transmission is achieved in the supra-threshold regime.

To quantify the optimal encoding regime, we obtained the average membrane potential of the neuron from the bias current, which maximizes the information transmission per unit cost for different baseline costs and noise levels. Figure 4.4 shows the average membrane potential that optimizes information transmission, plotted against the standard deviation of the membrane potential σ_V for different baseline costs ($b = 1$: blue line; $b = 3$: green line; and $b = 10$: red line). Interestingly, the Fig. reveals that the optimal distance between the average membrane potential and the threshold (black dashed curve) is about one to two σ_V , depending on the actual baseline cost. Thus, for less dominating baseline cost, the information transmission becomes maximal at an average membrane potential, which is about one standard deviation of V_m away from the threshold.

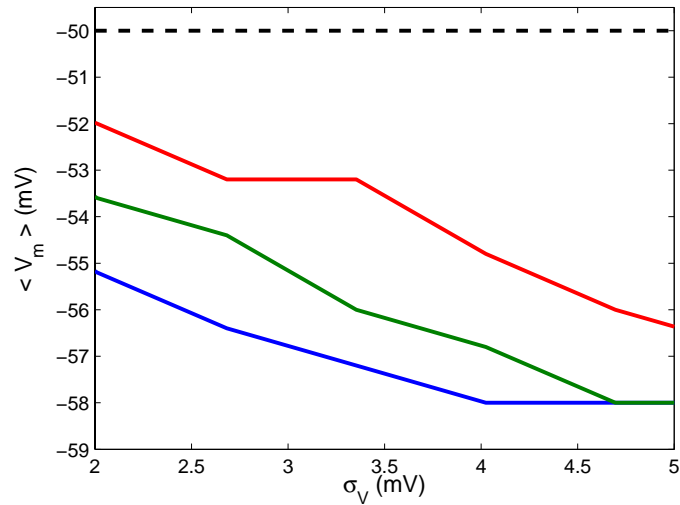


Figure 4.4.: Average membrane potential, for which information rate per unit cost is maximal, plotted against the standard deviation of the membrane potential σ_V for different baseline costs ($b = 1$: blue line; $b = 3$: green line; and $b = 10$: red line).

4.4. Discussion

In this model study we examined how background activity affects the information transmission. We showed that the background activity can have a wide influence on the information transmission properties of a LIF neuron if the driving signal is mainly subthreshold. For such signals, the noise level has to be adjusted accurately in order to optimize stimulus encoding for changing intensities of the input (Collins et al., 1995, Wenning and Obermayer, 2003; Hoch et al., 2003). On the other hand, a neuron could improve information transmission by making the stimulus more supra-threshold. In principle, this could be achieved either by lowering the spike threshold or by increasing the average membrane potential through a strengthening of the stimulus inducted synaptic drive. In the high noise regime, however, a reduction of the distance between the average membrane potential and the spike threshold was found to barely affect the information rate.

Recent studies have shown that neural systems prefer information transmission via many parallel low intensity channels (Laughlin et al., 1998; Balasubramanian et al., 2001; Hoch et al., 2003). Similar to that, our simulations of the LIF neuron have shown that after taking the cost of information transmission into account, optimal information transmission occurs in the subthreshold regime. This holds even for small

4. *Neural Information Transmission*

noise levels, provided that the baseline costs are not too small compared to the rate dependent costs. Since application of noise is one way to allow for transmission of otherwise subthreshold signals, the strive for energy efficient codes may be a justification of stochastic resonance in neural systems.

5. Pulse Detection

5.1. Introduction

Recent experimental and modeling studies have shown that cortical neurons receive a large number of simultaneous active inputs, which give rise to a strongly fluctuating membrane potential (Paré et al., 1998; Anderson et al., 2000a) and much effort has been made to understand the role of these fluctuations for neural computation. In the previous chapter we have shown that such a fluctuating membrane potential may improve the transmission of weak time-dependent signals. In this chapter we go a step further towards information processing and concentrate upon the question of how the detection of weak synchronous activity depends on the dynamics of the membrane potential.

It is widely believed that synchronous activity, which is found in many regions of the brain (Alonso et al., 1996; Usrey and Reid, 1999; Engel et al., 2001), is an important element in cortical processing. It has been shown that the synchronous arrival of spikes from a presynaptic ensemble of neurons is more efficient in evoking a response (Alonso et al., 1996; Salinas and Sejnowski, 2000), and it has been argued that such rapid excitations are necessary to explain the high variability of spike trains observed *in vivo* (Stevens and Zador, 1998). In the visual cortex, however, the detection of synchronous activity of a presynaptic ensemble may be strongly influenced by the synaptic background activity (Azouz and Gray, 2003), and it may be difficult for a postsynaptic neuron to distinguish responses to synchronous inputs from those that occur by chance. In general, increasing the synaptic weight may not help in this case, as the significance of the input at a certain synapse may change on a time scale of milliseconds. It may be advantageous for neurons if they were able to increase detection performance through other mechanisms - for example, by adapting the temporal correlation of the membrane potential through a variation of the synaptic delay constants of their synapses.

In a previous study, we have shown for a single leaky integrate-and-fire (LIF) neuron with current noise that if the noise is colored (Ornstein-Uhlenbeck process), the

detection of synchronous spiking events becomes more robust for increasing temporal correlations of the noise (Wenning et al., 2005). However, these simulations did not take into account the increase in conductance due to the background activity, which dramatically modifies integrative properties of a cell (Destexhe and Paré, 1999; Destexhe et al., 2003; Azouz and Gray, 2003), such as the effective membrane time constant or the shape of induced postsynaptic potentials (Kuhn et al., 2004). Furthermore, we have shown for the single neuron case that the fraction of correctly detected subthreshold pulses never becomes better than 50% since half of the time the membrane potential fluctuations are below its mean (Wenning et al., 2005). To overcome this limitation, a population of neurons has to be considered.

In our model study, we thus explore how the detection performance of a neural population depends upon the statistics of the synaptic background activity, the synaptic time constants, and the shape of the postsynaptic potential (PSP). For a population of LIF neurons with current noise, we find that the detection performance increases with increasing time constants of the synaptic noise, similar to the single neuron case. If the synchronous activity, however, is induced by a biologically more realistic model of a synapse (exponential decaying PSP in place of short rectangular pulses), we find a broad regime, where a *decrease* of the temporal correlation of the membrane potential leads to an increase in the detection performance of the population. We show that this increase in detection performance is due to the larger decay phase of the PSP, which allows a faster changing membrane potential to induce more action potentials. Additional simulations of a population with conductance-based LIF neurons, which include the effects of conductance fluctuations and shot noise, yield similar results. Since it is likely that cortical neurons process synchronous activity at low firing rates (Olshausen and Field, 2005), we conclude from these simulations that, in contradiction to single neuron model, the detection performance of a neural population is optimized by a reduction of the temporal correlation of the membrane potential.

5.2. Materials and Methods

5.2.1. Single-compartment model

We consider a population of LIF neurons with no recurrent connection between the neurons. For a detailed description of the LIF model see Sec. 2.2.1. The membrane potential V_m of the LIF neurons changes in time according to the differential equation:

$$C_m \frac{dV_m}{dt} = -I_L - I_p - I_{syn}, \quad (5.1)$$

where $I_L = -g_L(V_m - E_L)$ is the leak current, $C_m = 0.5 \text{ nF}$ is the membrane capacitance, and $E_L = -80 \text{ mV}$ is the reversal potential. The leak conductance was set to $g_L = 100 \text{ nS}$ and $g_L = 30 \text{ nS}$ for the simulations with current and conductance noise, respectively. The threshold value was set to $V_{th} = -55 \text{ mV}$ and, after a spike, the membrane potential was clamped to $V_{rest} = -65 \text{ mV}$ for a duration of $T_{ref} = 1.8 \text{ ms}$ (absolute refractory period).

The input to each neuron in the population consisted of a regular train of pulses and synaptic noise I_{syn} . In order to mimic synaptic delays, the pulses had the same onset time but with a jitter in time according to a Gaussian distribution with zero mean and standard deviation $\sigma_{Tp} = 0.5 \text{ ms}$ if not stated otherwise. The time interval between successive pulses was large ($T_p = 100 \text{ ms}$) compared to the membrane time constant, so that the preceding pulse had no significant influence on the one following.

We used two different models to describe the PSP of an individual pulse. The first was similar as in Wenning et al. (2005), and described the PSP as a narrow rectangular current pulse with strength I_p and duration of 0.2 ms . As a second model we used the exponential synapse. When a pulse was arrived by the neuron, a quantal current increase was produced, which then decayed exponentially towards zero with a decay time constant of $\tau_p = 2.7 \text{ ms}$. For most simulations the strength of the PSP was adjusted such that a given detection quality was achieved.

5.2.2. Synaptic Noise Model

Synaptic background activity not only leads to a strongly fluctuating membrane potential but also increases the conductance of the neuron (see above). According to Richardson and Gerstner (2005), the conductance increase can be taken into account either by adjusting the membrane time constant properly (effective-time-constant approximation) or by modeling the conductance-based synaptic drive explicitly. The latter approach is superior, since it allows the modeling of nongaussian features of the membrane potential fluctuations, such as its skew (for more details see Richardson and Gerstner, 2005).

In this study we investigate pulse detection for two different noise models. First, we describe the total synaptic current I_{syn} as the sum of a bias current I_{bias} , which was included to adjust the average membrane potential $\langle V_m \rangle$ to a given value, and a synaptic noise current I_N , which was described by an Ornstein-Uhlenbeck process (OUP, cf. Sec. 2.3):

$$\frac{dI_N(t)}{dt} = -\frac{1}{\tau_X} I_N(t) + D \frac{dW}{dt}, \quad (5.2)$$

where τ_X is the synaptic time constant, D is the diffusion coefficient, and $dW(t)$ is the infinitesimal increment of a Wiener process. Different noise conditions are modeled by changing the time constant τ_X and the diffusion coefficient D of the OUP. If the spike process is omitted, e.g. if we only consider the subthreshold dynamics of the membrane potential, then changing τ_X or D affects the standard deviation σ_V of the membrane potential but not its mean. The relation between σ_V and the parameters of the OUP is given by (Wenning et al., 2005)

$$\sigma_V^2 = \frac{D}{2} \frac{\tau_m^2 \tau_X^2}{\tau_m + \tau_X}. \quad (5.3)$$

We use eq. (5.3) to determine the value of D , which leads to the same value of σ_V after a change of τ_X . In addition we adjusted the membrane time constants of the LIF neurons to 5 ms in order to account for the reduction of the membrane time constant due to the synaptic background activity.

Second, we used a synaptic noise model which includes the synaptic conductance explicitly. This allows the examination of the combined effects of conductance fluctuations and shot noise on the membrane potential. The total synaptic current I_{syn} is given by:

$$I_{syn}(t) = g_e(t)(V_m(t) - E_e) + g_i(t)(V_m(t) - E_i), \quad (5.4)$$

where $g_e(t)$ and $g_i(t)$ are two fluctuating conductances, where each was driven by a Poisson process:

$$\tau_e \frac{dg_e}{dt} = -g_e + a_e \tau_e \sum_{t_{k_e}} \delta(t - t_{k_e}), \quad (5.5)$$

$$\tau_i \frac{dg_i}{dt} = -g_i + a_i \tau_i \sum_{t_{k_i}} \delta(t - t_{k_i}), \quad (5.6)$$

where τ_e and τ_i are the synaptic time constants, a_e and a_i are the quantal conductance amplitudes, t_{k_e} and t_{k_i} are the Poisson-distributed arrival times of the spikes generated by the background activity with rate f_e and f_i . Mean and variance of $g_e(t)$ and $g_i(t)$ are related to $\tau_{e,i}$, $a_{e,i}$, and $f_{e,i}$ through (Richardson and Gerstner, 2005):

$$\langle g_{e,i} \rangle = a_{e,i} \tau_{e,i} f_{e,i}, \quad (5.7)$$

$$\sigma_{e,i} = a_{e,i} \sqrt{\frac{\tau_{e,i} f_{e,i}}{2}}. \quad (5.8)$$

Mean, standard deviation, and synaptic time constants of the excitatory and inhibitory conductances were taken from Destexhe et al. (2001). Different combinations of mean and standard deviation of the membrane potential were achieved by varying the mean $\langle g_{e,i} \rangle$ and the standard deviation $\sigma_{e,i}$ of the excitatory and inhibitory conductance independently (for more details see Appendix C). In addition we reduced the leak conductance of the neuron such that the effective membrane time constant was similar to the current-based neuron, e.g.

$$\tau_{eff} = \frac{C_m}{G_{tot}} = \frac{C_m}{g_l + \bar{g}_e + \bar{g}_i} \sim 5 \text{ ms}, \quad (5.9)$$

in order to ease the comparison of the two models.

All simulations were done using the Euler integration scheme with an exact update equation (Gillespie, 1996). The simulation time step was set to $dt = 0.1 \text{ ms}$.

5.2.3. Temporal Correlation of the Membrane Potential

The temporal correlation (or correlation time) of the membrane potential of a neuron is determined mainly by the time constant of the synaptic noise and by the conductance state of the neuron. For the current-based LIF neuron, the effect of the conductance on the membrane potential dynamics was accounted by a reduction of the membrane time constant. Hence, the temporal correlation of V_m depends only on the synaptic time constant of the noise.

Figure 5.1A shows the correlation time of the membrane potential plotted against σ_V for different values of τ_X , e.g. $\tau_X = 2.5 \text{ ms}$ (blue lines), $\tau_X = 5 \text{ ms}$ (red lines), and $\tau_X = 10 \text{ ms}$ (black lines). The solid and dotted lines correspond to simulations with $\langle V_m \rangle = -65 \text{ mV}$ and $\langle V_m \rangle = -59 \text{ mV}$, respectively. The correlation time of V_m was estimated using eq. (2.23) [cf. Sec. 2.4]. An increase of the synaptic time constants of the OUP leads to an increase of the temporal correlation of the membrane potential, which means that the number of rapid and large fluctuations of V_m is reduced. In other words, after a spike it takes more time on average to reach the threshold again. Note that the dependence of the temporal correlation of the membrane potential on mean and standard deviation of V_m is negligible, as Fig. 5.1A indicates.

Figure 5.1B shows the correlation time of the membrane potential for the conductance-based LIF neuron. The red lines show the correlation time of V_m for simulations with

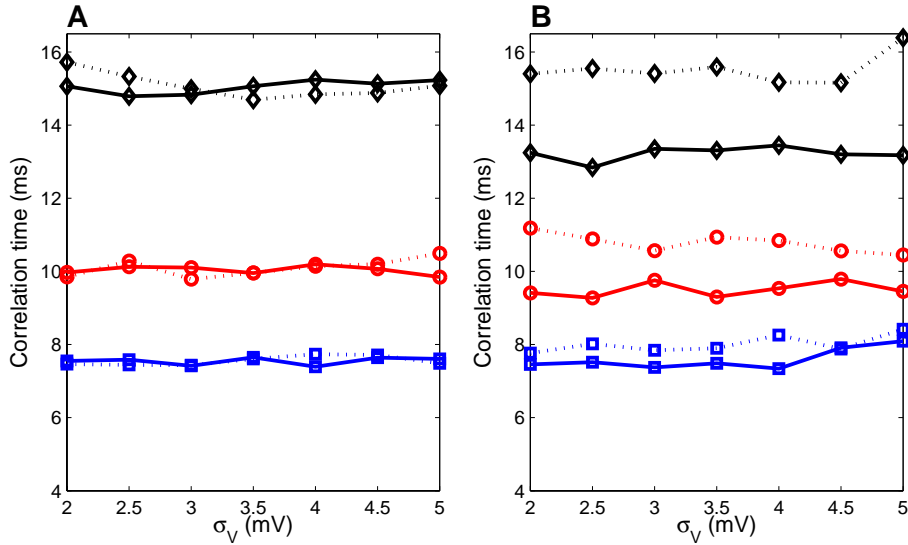


Figure 5.1.: Correlation time of the membrane potential plotted against σ_V for the current-based (A) and the conductance-based (B) LIF neuron. The red lines show the correlation time for $\tau_X = 5 \text{ ms}$ (A) and $\tau_e = 2.7 \text{ ms}$, $\tau_i = 10.5 \text{ ms}$ (B), respectively. In both Fig., the blue lines correspond to simulations with reduced and the black lines to increased synaptic time constants by a factor of two. The solid represent simulations with $\langle V_m \rangle = -65 \text{ mV}$ and the dotted lines correspond to $\langle V_m \rangle = -59 \text{ mV}$. For other simulation parameters see Sec. 5.2.1.

$\tau_e = 2.7 \text{ ms}$ and $\tau_i = 10.5 \text{ ms}$, whereas the blue lines represent the simulation results for $\tau_{e,i} \rightarrow \frac{1}{2}\tau_{e,i}$ and the black line for $\tau_{e,i} \rightarrow 2\tau_{e,i}$. At an average membrane potential just below threshold ($\langle V_m \rangle = -59 \text{ mV}$; dotted lines), a modification of the synaptic time constants leads to similar values for the temporal correlation as for the current-based model. At $\langle V_m \rangle = -65 \text{ mV}$, however, a change of τ_e, τ_i leads to smaller values of the temporal correlation. Such low values of $\langle V_m \rangle$ were achieved by a strong reduction of the excitatory mean conductance while the standard deviation remains almost the same, which results in a reduction of f_e accompanied by an increase of the quantal amplitudes a_e according to eq. (5.7). Since the statistical parameters of the inhibitory conductance do not change, the stronger PSP of the excitatory drive slightly reduce temporal correlation of the membrane potential.

5.2.4. Pulse Detection Scenario

The entire response of the population is the sum of the individual responses of the single neurons, and serves as the basis for calculating the receiver operating characteristic curve (ROC). The ROC curve provides a convenient way to quantify the detection performance of a population of neurons and is calculated as follows. First, we divide the whole response into time windows (bin) of equal size and count the number of spikes in these bins. If the number of spikes is above a certain threshold, we then classify the response as correctly detected if there was an input pulse during that time, and as a false positive event otherwise. The ROC curve is given by the fraction of correctly detected events as a function of the number of false positive examples and is generated by varying the detection threshold. Fig. 5.2A shows the resulting raster plot of a simulation of a population of 100 HH neurons (triggered by the pulse onset). Each row of the plot shows the entire response of the population to one pulse packet. The resulting raster plot is summed up to yield the peri stimulus time histogram (PSTH), which is shown in Fig. 5.2B. Because the response to the pulse packet is spread over time, the area under the ROC curve depends on the bin size (Fig. 5.2D). In the following, all ROC curves were calculated with a bin size that maximized the area under the ROC curve. Bins were always centered to the maximum of the PSTH. Fig. 5.2C shows the re-binned raster plot of Fig. 5.2A with an optimal bin size of 4.6 ms .

5.3. Results

First, we explored the relationship between the detection performance and the mean and standard deviation of the membrane potential for a population of 100 LIF neurons with current noise. Figure 5.3A shows the area under the ROC curve plotted against the standard deviation of the membrane voltage. At an average membrane potential of $\langle V_m \rangle = -65\text{ mV}$ (blue solid curve), a high detection quality for weak pulses is only achieved if the standard deviation of membrane potential is high, because the correct detection rate increases faster with σ_v than the false positive rate. If the distance to the threshold is decreased ($\langle V_m \rangle = -59\text{ mV}$; red dotted curve), however, the detection quality decreases slightly with increasing values of σ_v . The stronger fluctuating membrane potential leads to a higher firing rate of the neurons making the detection of the pulses more difficult. Depending on the distance to threshold and the pulse strength, there exists an optimal level of σ_v , for which the detection quality is maximal, similar as in a stochastic resonance setting.

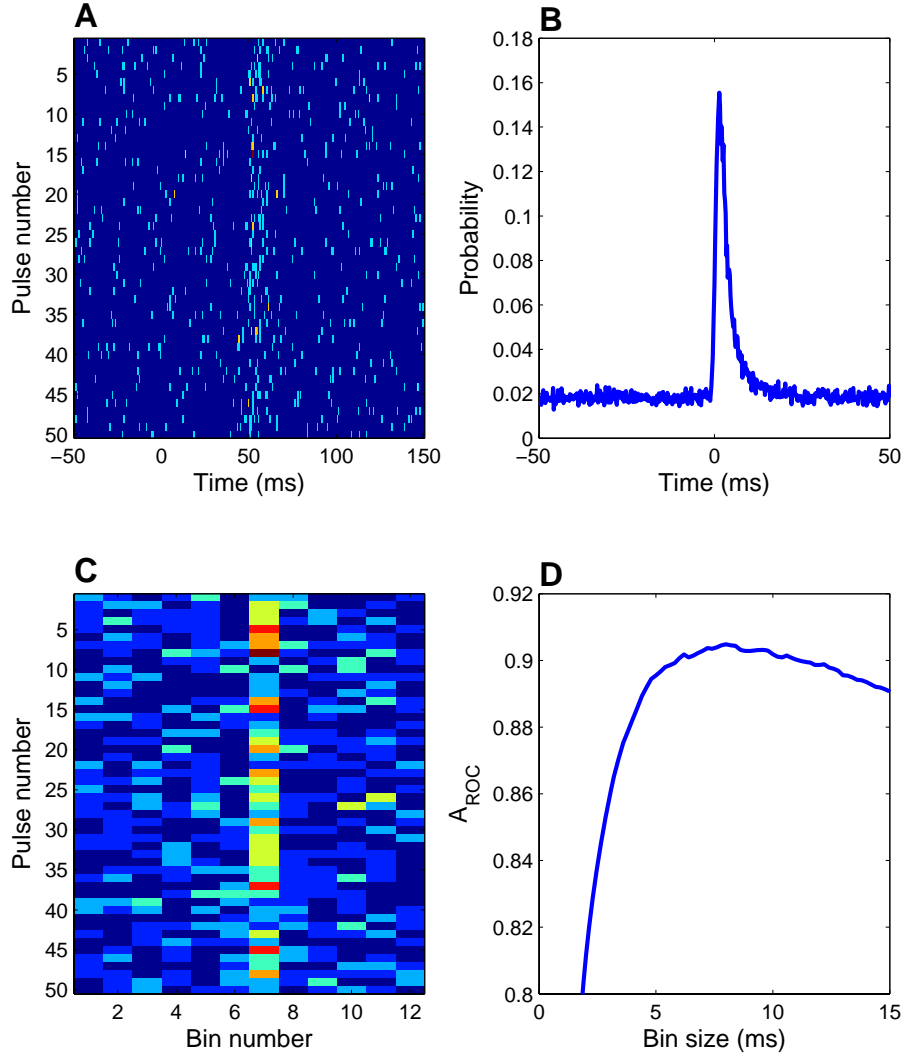


Figure 5.2.: Calculation of the ROC curve for a population of 100 neurons ($\langle V_m \rangle = -63$ mV, $\sigma_V = 5$ mV, $dt = 0.2$ ms). A) Raster plot of the response (bin size equals $dt = 0.2$ ms). Each row shows the response to one pulse. The traces were aligned in such a way that the pulse onset is at $t = 0$ ms. B) Post stimulus time histogram of the response. C) Raster plot of the population response with an optimal bin size of 4.6 ms, which maximizes the area under the ROC curve. D) Dependency of the area under the ROC curve on the bin size.

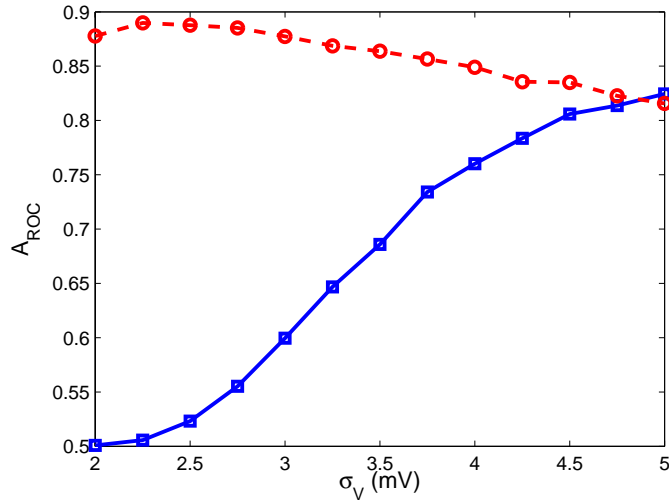


Figure 5.3.: The area under the ROC curve plotted against the standard deviation of the membrane voltage (σ_V) for a population of 100 LIF neurons with current noise (red dashed line: $\langle V_m \rangle = -59 \text{ mV}$, $I_p = 2 \text{ nA}$; blue solid line: $\langle V_m \rangle = -65 \text{ mV}$, $I_p = 4 \text{ nA}$). For other simulation parameters see Sec. 5.2.1.

Furthermore, we find that the response detection quality of the population critically depends on the temporal precision of the input measured by the standard deviation of the underlying density of spike arrival times (cf. Sec. 5.2.1). Figure 5.4A shows the area under the ROC curve plotted against the standard deviation of spike arrival times (σ_{Tp}) for a population of 100 LIF neurons. The red dashed curve shows the simulation results for the population with an average membrane potential of the neurons just below threshold ($\langle V_m \rangle = -57 \text{ mV}$ and $\sigma_V = 2 \text{ mV}$). The detection quality is highest for highly synchronized inputs and decreases with increasing σ_{Tp} . An increased temporal dispersion of the input requires a larger optimal time window for pulse detection and, therefore, accumulates more noise induced action potentials, which results in a decrease in detection performance. Hence, at high values of σ_{Tp} , an increase of σ_V to 5 mV (black dotted curve) leads to a decrease in detection performance, because of the higher firing rate of the neurons. A decrease of the firing rate due to a lower average membrane potential on the other hand, leads to an improved detection performance (blue solid curve: $\langle V_m \rangle = -65 \text{ mV}$ and $\sigma_V = 5 \text{ mV}$).

Interestingly, we find that the detection window (T_{det}) itself depends hardly at all on the mean and standard deviation of V_m , as Fig. 5.4B indicates. For all three above mentioned cases, T_{det} is almost linearly related to σ_{Tp} . Moreover, optimal detection is

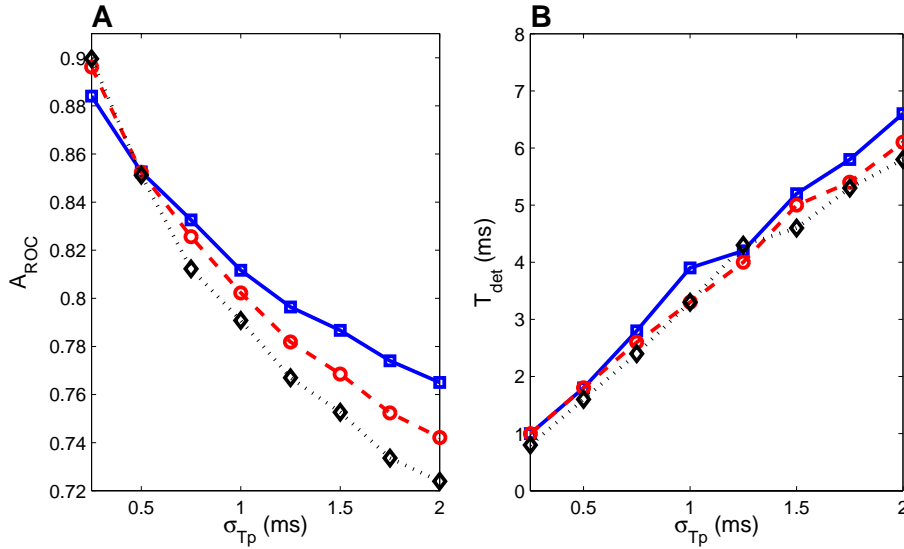


Figure 5.4.: A) The area under the ROC curve plotted against the standard deviation of the spike arrival times (σ_{Tp}) for a population of 100 LIF neurons. B) Width of the optimal time window T_{det} plotted against σ_{Tp} . In both Fig., the curves show the simulation results for different combinations of $\langle V_m \rangle$ and σ_V , e.g. the blue (solid) curve corresponds to $\langle V_m \rangle = -65 mV$ and $\sigma_V = 5 ms$, the red dashed curve corresponds to $\langle V_m \rangle = -57 mV$ and $\sigma_V = 2 ms$, and the black dotted curve corresponds to $\langle V_m \rangle = -57 mV$ and $\sigma_V = 5 ms$. The pulse strength was adjusted such that the area under the ROC curve was approximately 0.85 for $\sigma_{Tp} = 0.5 ms$. For other simulation parameters see Sec. 5.2.1

achieved at a time window, which is approximately four times the standard deviation of spike arrival times.

The above described relation between the optimal time window and σ_{Tp} is not valid for low values of σ_V and large distances between $\langle V_m \rangle$ and the spike threshold. In this regime, the optimal time window T_{det} for pulse detection is much broader and its dependency on σ_{Tp} is reduced (Fig. 5.5B). Because most of the pulses do not lead immediately to a spike response, which leaves the membrane potential just below threshold, the probability that a spike is induced by the noise strongly increases. Figure 5.5C shows the post stimulus time histogram of the response of a single neuron for $\sigma_{Tp} = 0.5 ms$ (blue solid curve). The Fig. shows nicely that the probability of a spike response increases during the time window of $\pm 2\sigma_{Tp}$ at pulse onset time ($t = 0 ms$). After the immediate response, however, the probability of a spike response

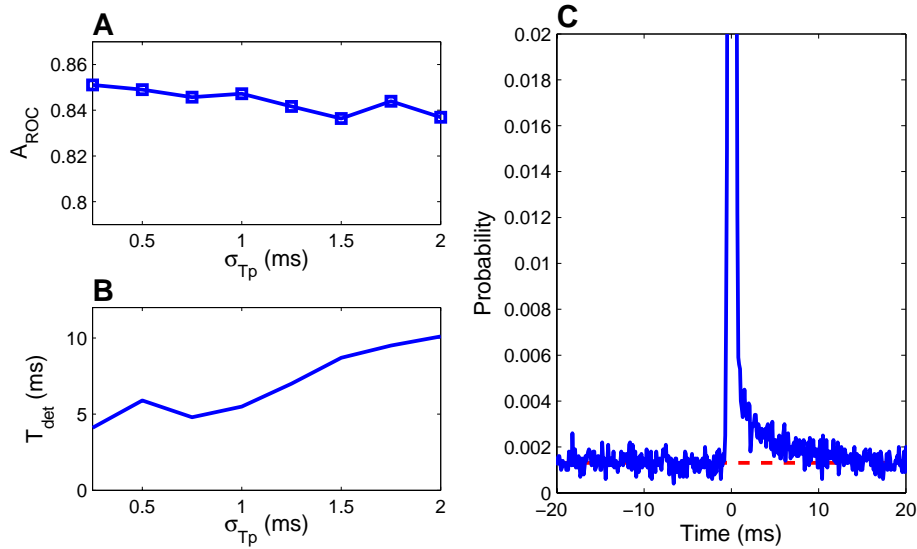


Figure 5.5.: A) The area under the ROC curve plotted against the standard deviation of the spike arrival times (σ_{Tp}) for a population of 100 LIF neurons ($\langle V_m \rangle = -65 mV$ and $\sigma_V = 2 mV$). B) Width of the optimal time window T_{det} plotted against σ_{Tp} for the population in A). C) Post stimulus time histogram of the population response for $\sigma_{Tp} = 0.5 ms$ (blue solid curve). The red (dashed) line indicates the probability of a spike response by the noise alone.

is elevated for at least another 10 ms as a comparison with the dashed line indicates, which represents the probability of a spike response induced by the noise alone. The population can increase its detection performance if it takes advantage of the prolonged increase in spiking probability. As a consequence, the optimal detection windows are long and the area under the ROC curve remains almost the same (Fig. 5.5A).

5.3.1. Effect of the Synaptic Time Constants

Besides the mean and standard deviation, the temporal correlation of the membrane potential is an important factor influencing the detection of synchronous spiking effects (Wenning et al., 2005). There we have investigated how well a single LIF neuron with current noise (OUP) detects short current pulses for increasing values of σ_V . If the noise induced firing rate of the neuron is high, an increase of the temporal correlation of the membrane potential improves the detection performance, because of the beneficial decrease of the false positive rate. At low noise levels, however, the firing rate of

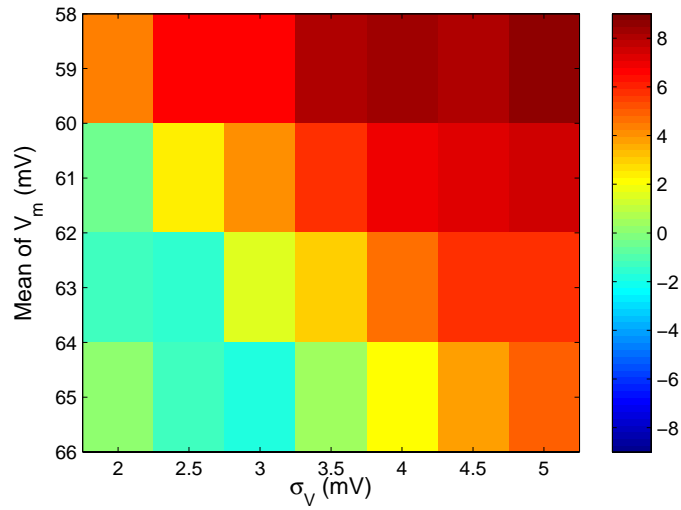


Figure 5.6.: Percentage increase of the area under the ROC curve when the time constant of the current noise is raised ($\tau_X = 2.5 \text{ ms} \rightarrow \tau_X = 10 \text{ ms}$), for different combinations of $\langle V_m \rangle$ and σ_V of the membrane potential. The population consisted of 100 LIF neurons and the pulse strength was adjusted such that the area under the ROC curve was approximately 0.85 for $\tau_X = 5 \text{ ms}$ and $\sigma_{T_p} = 0.5 \text{ ms}$. For other simulation parameters see Sec. 5.2.1.

the neuron is low and changes of the temporal correlation barely affect the detection performance.

Although using a different measure for detection performance, we find the same behavior for a neural population consisting of 100 LIF neurons. Figure 5.6A shows the percentage increase of the area under the ROC curve for an increase of the synaptic time constant by a factor of four for a broad range of different values of $\langle V_m \rangle$ and σ_V . The Fig. shows nicely that the detection performance increases with increasing temporal correlation of the membrane potential, if both the mean and standard deviation of V_m are raised. Note that a modification of the time constant of the OUP leads to a change of σ_V [cf. eq. (5.3)]. Since the detection performance critically depends upon $\langle V_m \rangle$ and σ_V (see above), we adjusted after each change of τ_X the diffusion constant D in such a way that $\langle V_m \rangle$ and σ_V of the free membrane potential (without spike threshold) remained at the same value.

The area under the ROC curve depends on two quantities: the probability of correct detection and the false positive rate. Either an increase of the probability of correct detection or a decrease of the false positive rate can lead to a better detection perfor-

mance. Figure 5.7A shows the probability of correct detection as a function of σ_V for an average membrane potential of $\langle V_m \rangle = -65 mV$. In contrast to the single neuron case (Wenning et al., 2005), Fig. 5.7A shows that the probability of correct detection slightly depends on the value of τ_X . A reduction of τ_X from $10 ms$ (red diamond curve) to $2.5 ms$ (blue square curve) leads to small increase of the probability of correct detection. This increase is a result of the higher false positive rate at $\tau_X = 2.5 ms$ (Fig. 5.7C), which noticeable contributes to the probability of correct detection, since the optimal time window for pulse detection is much larger than in Wenning et al. (2005). If we take the contribution of the false positive rate into account (see the corresponding dotted lines in Fig. 5.7A), we find that the probability of correct detection is almost independent of τ_X . Thus, at low values of $\langle V_m \rangle$ and σ_V , an increase of the synaptic time constants results to a decrease in the probability of correct detection counterbalancing the beneficial decrease of the false positive rate (Fig. 5.7C).

At an average membrane potential just below threshold ($\langle V_m \rangle = -59 mV$) on the other hand, the firing rates of the neurons are high and a reduction of τ_X leads to a substantial decrease in the false positive rate (Fig. 5.7D), which contributes remarkably to the better detection performance of the population. Moreover, the probability of correct detection decreases for increasing τ_X (Fig. 5.7B) similar to before. However, after taking the reduction of the false positive rate into account (dotted lines in Fig. 5.7B), the Fig. reveals a higher probability of correct detection after the increase of τ_X . After each spike, the membrane potential is reset to V_{rest} , which is substantially lower than $\langle V_m \rangle$. Hence, it takes some time until the membrane potential recovers in average to its resting value $\langle V_m \rangle$ leading to a lower average membrane potential at pulse onset times at high firing rates. At $\langle V_m \rangle = -59 mV$ a reduction of the synaptic time constants leads to substantial higher firing rates of the neurons, which noticeably lowers the average membrane potential at pulse onset times explaining the slight decrease of the probability of correct detection.

5.3.2. Effect of the Shape of the Postsynaptic Potential

The above results were derived with short current pulses in order to provide a pulse detection scenario similar as in Wenning et al. (2005). From a biological point of view, however, current pulses are unrealistic and the exponential synapse might be a better model because it includes the decay phase of the PSP. In the following we use a single exponential synapse with a decay time of $\tau_p = 2.7 ms$ at each neuron to introduce the synchronous activity.

The replacement of the current pulse synapses by the exponential synapses changes the pulse detection task remarkably. Since the width of the PSP is mainly determined

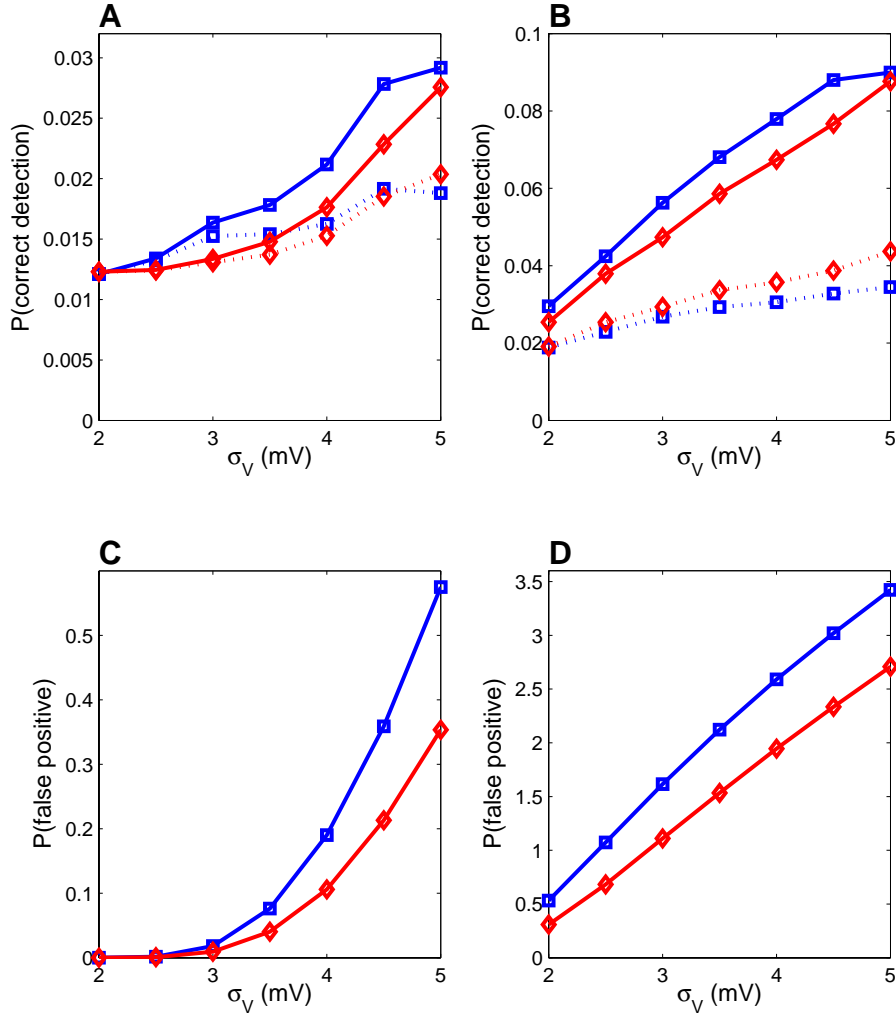


Figure 5.7.: A) Probability of correct detection of a single neuron plotted against σ_V for $\langle V_m \rangle = -65$ mV. The blue (square) curves represent the correct detection rate for neurons with $\tau_X = 2.5$ ms, the red (diamond) curves for neurons with $\tau_X = 10$ ms. B) The same as in A) but for $\langle V_m \rangle = -59$ mV. C) False positive rate as a function of σ_V . The different curves correspond to the two cases from A). D) The same as in C) but for $\langle V_m \rangle = -59$ mV. The population consisted of 100 LIF neurons and the pulse strength was adjusted such that the area under the ROC curve is approximately 0.85 for $\tau_X = 5$ ms and $\sigma_{T_p} = 0.5$ ms. For other simulation parameters see Sec. 5.2.1.

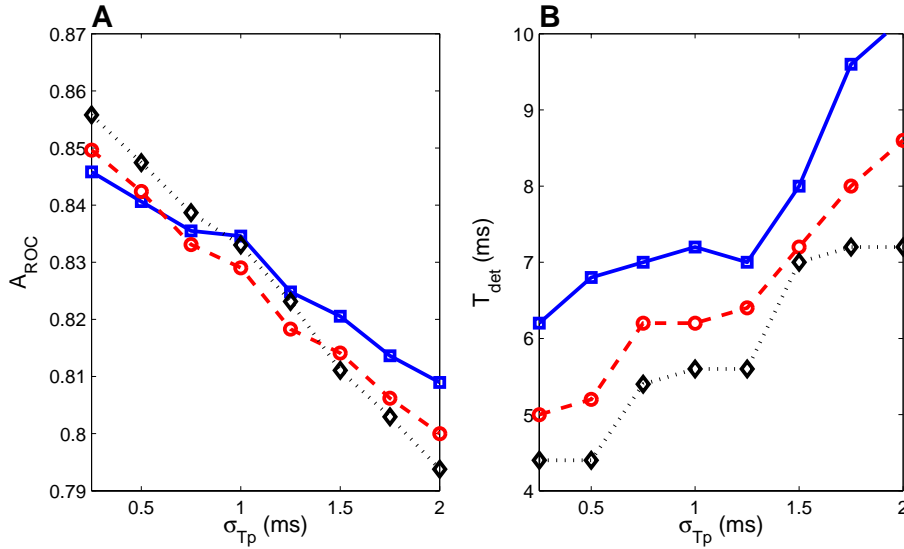


Figure 5.8.: A) The area under the ROC curve plotted against the standard deviation of the spike arrival times (σ_{Tp}) for a population of 100 LIF neurons. B) Width of the optimal time window T_{det} plotted against σ_{Tp} . In both Fig., the curves show the simulation results for different combinations of $\langle V_m \rangle$ and σ_V , e.g. the blue (solid) curve corresponds to $\langle V_m \rangle = -65 mV$ and $\sigma_V = 5 ms$, the red dashed curve corresponds to $\langle V_m \rangle = -57 mV$ and $\sigma_V = 2 ms$, and the black dotted curve corresponds to $\langle V_m \rangle = -57 mV$ and $\sigma_V = 5 ms$. The quantal increase of the exponential synapses was adjusted such that the area under the ROC curve was approximately 0.85 for $\sigma_{Tp} = 0.5 ms$. For other simulation parameters see Sec. 5.2.1

by the synaptic decay constant τ_P , the use of exponential synapses leads to a broadening of the optimal detection window, as Fig. 5.8B indicates. Moreover, we find that action potentials are more easily induced by the membrane potential fluctuations during the exponential decay of the PSP and, therefore, the dependency of the optimal time window on mean and standard deviation of the membrane potential increases. Note that the longer detection window also reduces the dependency of the area under the ROC curve on the standard deviation of the spike arrival times (Fig. 5.8A).

Interestingly, the dependency of the detection performance on the temporal correlation is substantially increased. Fig. 5.9 shows again the percentage increase of the area under the ROC curve for an increase of the synaptic time constants τ_X of the OUP by a factor of four. A comparison with Fig. 5.6 reveals that at low mean and standard deviation of the membrane potential, the population with reduced synaptic

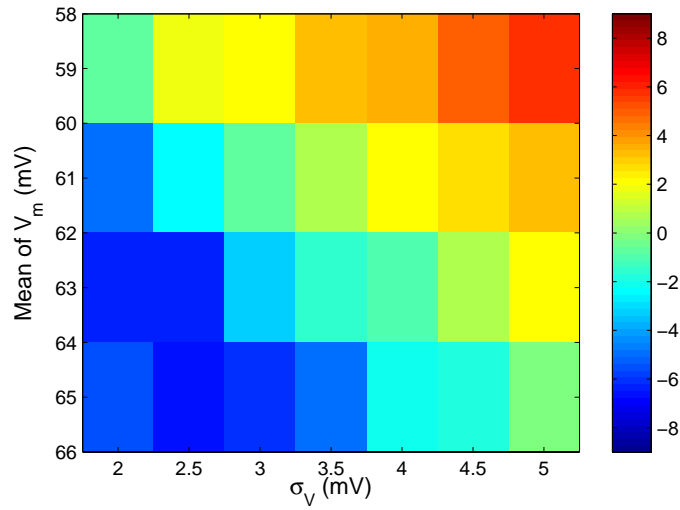


Figure 5.9.: Percentage increase of the area under the ROC curve when the time constant of the current noise is raised ($\tau_X = 2.5 \text{ ms} \rightarrow \tau_X = 10 \text{ ms}$), for different combinations of $\langle V_m \rangle$ and σ_V of the membrane potential. The population consisted of 100 LIF neurons and the strength of the exponential synapses was adjusted such that the area under the ROC curve was approximately 0.85 for $\tau_X = 5 \text{ ms}$ and $\sigma_{T_p} = 0.5 \text{ ms}$. For other simulation parameters see Sec. 5.2.1.

time constants performs even better than the population with the higher synaptic time constants (i.e. +7.1% at $\langle V_m \rangle = -65 \text{ mV}$ and $\sigma_V = 2.5 \text{ mV}$). Nevertheless, at an average membrane potential just below threshold, the increase of the synaptic time constant leads to an increase of the area under the ROC curve, and thus to a better detection performance, as was observed before.

If we take a closer look at the probabilities of correct detection and the false positive rate, we observe the following two points. First, since the noise model did not change, the dependency of the false positive rate on τ_X (Fig. 5.10C and D) is the same as in Fig. 5.7. Thus, the increased dependency of the detection performance on the temporal correlation originates entirely from a different behavior of the probabilities of correct detection. Figure 5.10A shows that the probability of correct detection is remarkably increased if the synaptic time constant is reduced. Although the optimal time window for the detection of exponential PSP is greatly enlarged, the increase of the probability of correct detection in Fig. 5.7A cannot be totally accounted by the increase of the false positive rate (see the corresponding dotted lines in Fig. 5.7A). The additional increase originates from the faster fluctuating membrane potential, which

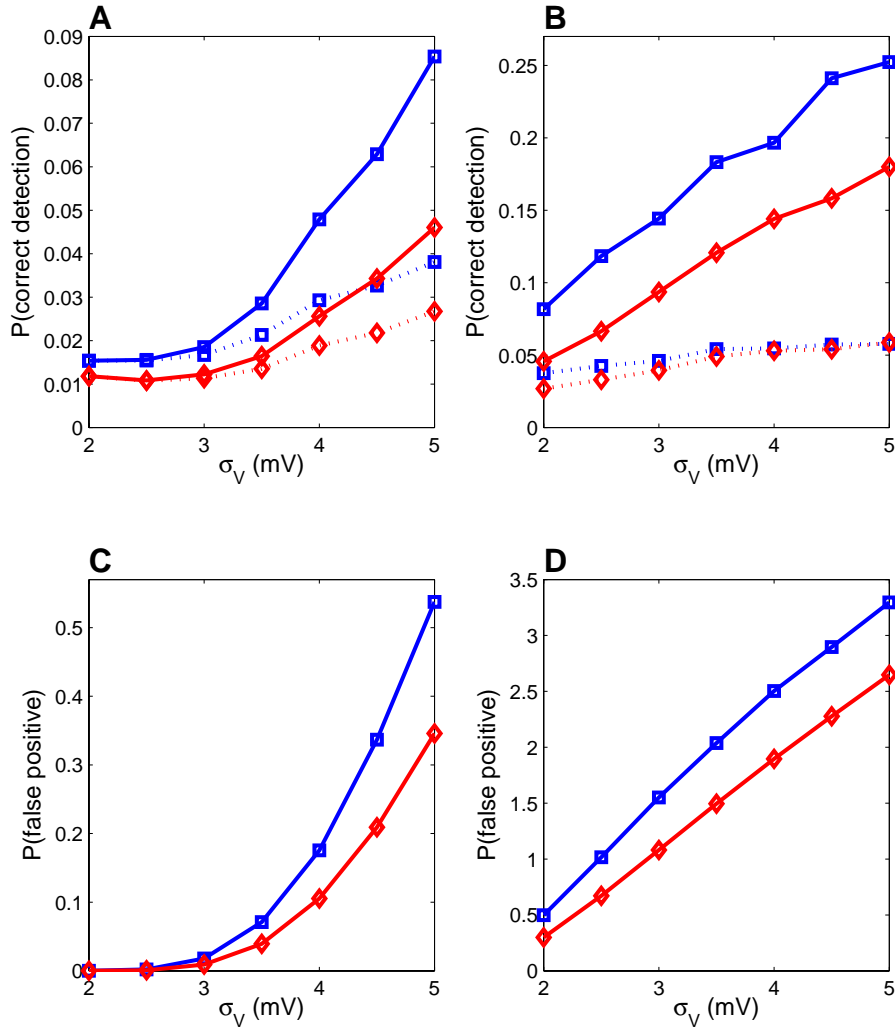


Figure 5.10.: A) Probability of correct detection of a single neuron plotted against σ_V for $\langle V_m \rangle = -65$ mV. The blue (square) curves represent the correct detection rate for neurons with $\tau_X = 2.5$ ms, the red (diamond) curves for neurons with $\tau_X = 10$ ms. B) The same as in A) but for $\langle V_m \rangle = -59$ mV. C) False positive rate as a function of σ_V . The different curves correspond to the two cases from A). D) The same as in C) but for $\langle V_m \rangle = -59$ mV. The population consisted of 100 LIF neurons and the strength of exponential synapses was adjusted such that the area under the ROC curve was approximately 0.85 for $\tau_X = 5$ ms and $\sigma_{Tp} = 0.5$ ms. For other simulation parameters see Sec. 5.2.1.

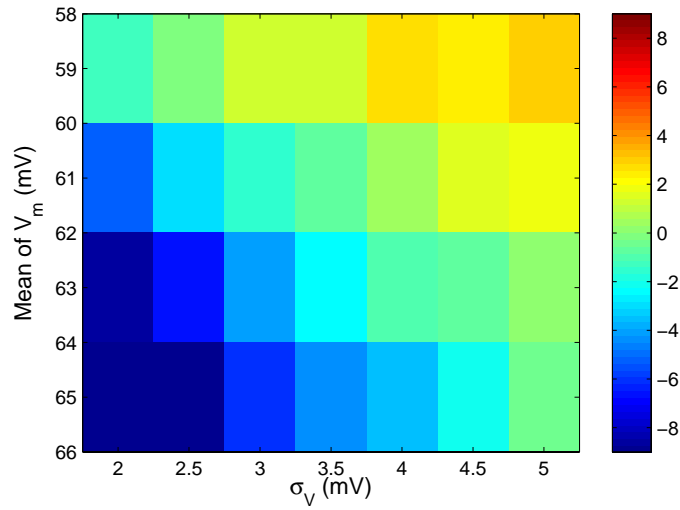


Figure 5.11.: Percentage increase of the area under the ROC curve when the time constant of the background activity is raised by a factor of four ($\frac{1}{2}\tau_{e,i} \rightarrow 2\tau_{e,i}$), for different combinations of $\langle V_m \rangle$ and σ_V of the membrane potential. The population consisted of 100 LIF neurons with conductance noise and the strength of the exponential synapses was adjusted such that the area under the ROC curve was approximately 0.85 for $\tau_X = 5\text{ ms}$ and $\sigma_{T_p} = 0.5\text{ ms}$. For other simulation parameters see Sec. 5.2.1.

more easily induces action potentials at the declining phase of the PSP. Note that near the threshold (Fig. 5.7B), the increase of the probability of correct detection due to the faster changing membrane potential is counterbalanced by the lower average membrane potential at pulse onset times (see above).

5.3.3. Effect of the Synaptic Conductance

In the two previous sections we used current-based neuron models and adjusted the membrane time constant to 5 ms in order to account for the effect the synaptic background conductance has on the stochastic voltage dynamics. However, this approach is only adequate if presynaptic firing rates are high and PSP are small. Otherwise, the effect of shot noise cannot be neglected and should be included into the noise model (Richardson and Gerstner, 2005). In the following, we use the conductance-based noise model described in Sec. 5.2.2 to investigate how the above derived results change, if shot noise and conductance fluctuations are taken into account.

Fig. 5.11 shows the percentage increase of the area under the ROC curve for an increase of the excitatory and inhibitory synaptic time constant by a factor of four ($\frac{1}{2}\tau_{e,i} \rightarrow 2\tau_{e,i}$) for the population with conductance noise. A modification of the time constants of $g_e(t)$ and $g_i(t)$ leads to a change in the mean and standard deviation of the membrane potential. Because the detection performance depends upon $\langle V_m \rangle$ and σ_V (see Sec. 5.3), in both cases we adjusted the mean and the standard deviation of the excitatory and inhibitory conductance fluctuations in such a way that $\langle V_m \rangle$ and σ_V remain at the same value (without threshold). Different to the current-based model, we find that an increase of the synaptic time constants leads to a smaller increase of the detection performance near threshold ($\langle V_m \rangle = -59 \text{ mV}$). For low values of $\langle V_m \rangle$ and σ_V , however, we find that an increase of the synaptic time constants leads to a much stronger decrease of the detection performance.

Figure 5.12A to D show the probability of correct detection and the false positive rate of the simulations with conductance-based neurons. A comparison with the current-based model (Fig. 5.10) reveals only marginal differences. Although mean and standard deviation of both models were the same, the probability of correct detection and false positive rate of the conductance-based model are slightly higher. In addition, we find also a small increase of the probability of correct detection after the accountancy of the influence of the false positive rate (dotted lines in Fig. 5.10A and B). Both effects are small and robust (e.g. a rerun of the simulations yielded similar results) and lead to a slightly improved detection performance at reduced synaptic time constants (Fig. 5.11).

5.4. Discussion

For the reliable detection of weak synchronous activity leading to subthreshold depolarizations, an ensemble of neurons has to be considered, since the correct detection rate of single neurons is limited to 50% (Wenning et al., 2005). Here we set up a population model consisting of 100 neurons and asked how the detection performance of such an ensemble depends on statistical properties of the membrane potential fluctuations. As a performance measure we used the area under the ROC curve, which describes the discrimination ability of the population to distinguish intervals where synchronous synaptic activity had been received from those where it had not. Our results lead to the following conclusions:

First, besides the mean and standard deviation of the membrane potential, its temporal correlation has a significant impact on the detection performance of the population. An increase of the temporal correlation leads to a smoother membrane potential

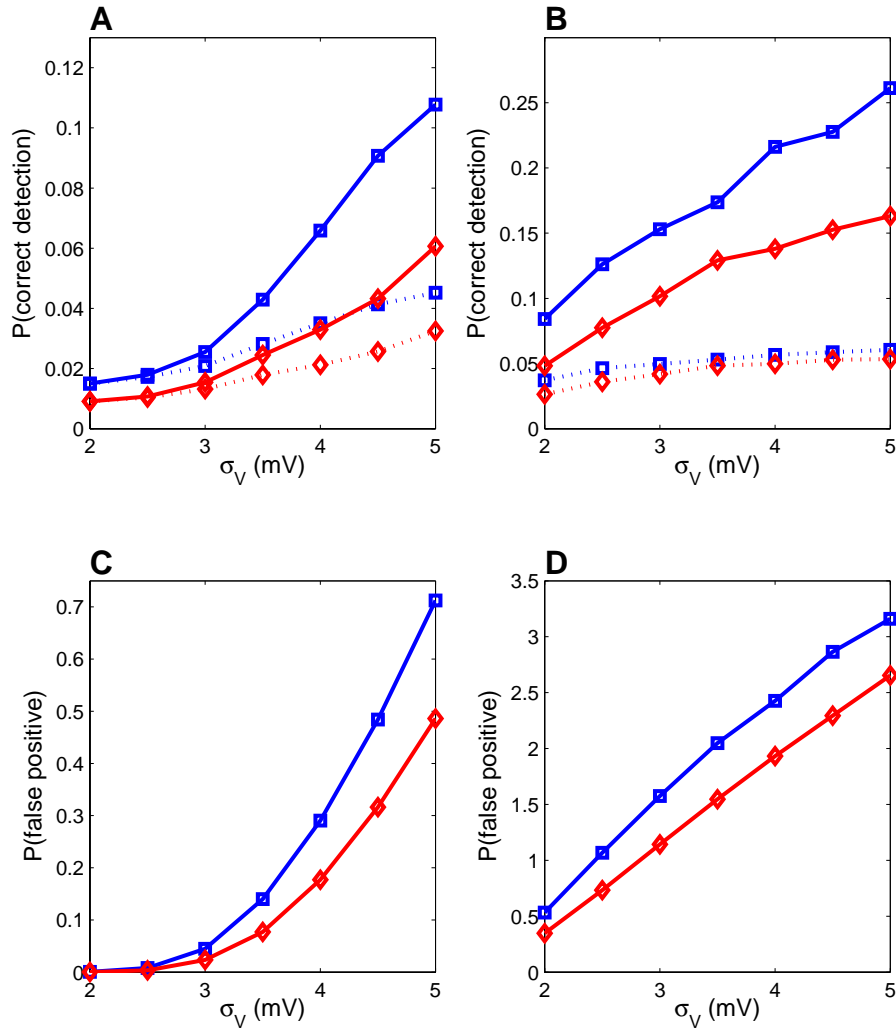


Figure 5.12.: A) Probability of correct detection of a single neuron plotted against σ_V for $\langle V_m \rangle = -65$ mV. The blue (square) curves and the red (diamond) curves represent the correct detection rate for neurons with lower ($\tau_{e,i} \rightarrow \frac{1}{2}\tau_{e,i}$) and higher ($\tau_{e,i} \rightarrow 2\tau_{e,i}$) temporal correlation of the membrane potential. B) The same as in A) but for $\langle V_m \rangle = -59$ mV. C) False positive rate as a function of σ_V . The different curves correspond to the two cases from A). D) The same as in C) but for $\langle V_m \rangle = -59$ mV. The population consisted of 100 LIF neurons and the strength of the exponential synapses was adjusted such that the area under the ROC curve is approximately 0.85 for $\tau_X = 5$ ms and $\sigma_{Tp} = 0.5$ ms. For other simulation parameters see Sec. 5.2.1.

with a lower average rate of change resulting to a reduction of the number of noise induced action potentials and thus to better detection performance at high firing rates. At low firing rates, however, a decrease of the temporal correlation is beneficial for the pulse detection task, since a faster changing membrane potential induces more likely action potentials during the interval where the synchronous activity was present. Since it is likely that cortical neurons process information at low firing rates (cf. Sec. 4.1 and Olshausen and Field, 2005), our results suggest that the detection performance of a population might be optimized by a reduction of the temporal correlation of the membrane potential.

Second, the shape of the postsynaptic potential is an important factor modulating the dependency between the detection performance and the temporal correlation. For signals with a stronger temporal correlation, the number of noise induced action potentials during the decay of the PSP is reduced, which results in a decrease in the percentage of correctly detected PSP. Interestingly, it has been shown that the shape of the PSP itself depends on the conductance state of the neuron and that an increase of the neurons conductance leads to a reduction of the amplitude and width of a PSP (Kuhn et al., 2004). Thus, we expect that at high background activity, the dependency of the detection performance on the temporal correlation is reduced because of the smaller width of the PSP.

Third, the more detailed model of synaptic background activity, which includes the effects of conductance fluctuations and shot noise on the membrane potential, led to similar results as the simulations with the current-based model, where the conductance increase was taken into account by a reduction of the membrane time constant. This indicates that for biologically realistic values of mean and standard deviation of the excitatory and inhibitory conductances (taken from Destexhe et al., 2001), the higher order properties of the membrane potential distribution, as for example its skew, barely affected the detection performance of the neural population.

Limitations of the model

Our population model rests on several simplifications, which may limit the conclusions of this study:

First, synaptic noise was assumed to be independent across the neurons allowing the population to average away much of the variability seen in the population response. In principle, the assumption of independent noise across the neurons allows the detection of smallest inputs in the limit of increasing population size. Recent experimental studies, however, have shown that the membrane potentials of nearby neurons can

be significantly correlated (Lampf et al., 1999; Usrey and Reid, 1999). Even worse, computational studies have indicated that the membrane potential fluctuations observed *in vivo* can only be achieved if there is substantial synchrony in the synaptic input (Destexhe and Paré, 1999; Harsch and Robinson, 2000). If the membrane potentials of neurons are correlated, only a part of the noise induced variability in the population response can be reduced by averaging, which limits the fidelity of the pulse detection task. Thus, if the dependency of the detection performance on population size and PSP amplitude is explored, synchrony in the synaptic input should be considered. However, since the temporal correlation of the membrane potential depends only on local properties of the neuron, we expect that the relation between the detection performance and temporal correlation is barely affected by input synchrony.

Second, an important element of realism that was not considered concerns the spike generation mechanism. The sensitivity of cortical neurons to synchronous synaptic inputs depends upon the rate of change of the membrane depolarization preceding a spike (Azouz and Gray, 2000; Henze and Buzsáki, 2001). Thus, we expect that the inclusion of Hodgkin-Huxley type spike generating mechanism may affect the dependency of the detection performance on the temporal correlation of the membrane potential. However, such an investigation is not straightforward. The detection performance strongly depends on the mean and standard deviation of the membrane potential, which change after an alteration of the temporal correlation. For the Hodgkin-Huxley neuron it is not clear how its synaptic noise parameters should be adjusted in order to allow for a meaningful comparison between simulations with different temporal correlations. In comparison, the LIF neuron can be simulated without a spike threshold allowing for an adjustment of mean and standard deviation of the membrane potential after a change of its temporal correlation. This is no longer possible for the Hodgkin-Huxley model neuron.

Finally, synaptic integration takes place in dendrites. The active properties of dendrites as well as their spatial extension remarkably affects the way the synaptic input is processed (London et al., 2002; Reyes, 2001). The simulation of a neural population consisting of multi-compartment model neurons is computationally demanding and difficult to parameterize. However, it would be interesting to see, if the results derived in this study remain valid if a more detailed model of a cortical cell was used.

6. Information Rate Estimation

6.1. Introduction

In the central nervous system of higher animals, information is likely to be coded using populations of neurons. Recently, the fundamental question of how stimulus features are represented by an ensemble of neurons has received a lot of attention (Pouget et al., 2000; Averbek and Lee, 2004). To address this question it is necessary to quantify the information encoding capabilities of a neural population precisely. Information theory, originally developed to quantify information transmission in communication systems, provides neuroscientists with system analysis techniques, which allow for a characterization of the information encoding in the most thorough way (Bialek et al., 1991; Gabbiani, 1996; Rieke et al., 1997; Strong et al., 1998; Borst and Theunissen, 1999; Reinagel and Reid, 2000; Krahe et al., 2002; Hatsopoulos et al., 2004).

Nevertheless, the estimation of the information rate from time-varying responses of a population remains problematic, because the combinatorial explosion of possible response patterns rapidly leads to a lack of data. The linear decoding model (Bialek et al., 1991; Gabbiani, 1996; Rieke et al., 1997, Borst and Theunissen, 1999; Krahe et al., 2002), which requires significantly less amounts of data compared to the other methods (e.g. direct and upper bound method), seems most appropriate. The linear decoder provides only a lower bound on the information rate, which is only close to the true information rate if noise is additive and Gaussian distributed and if the assumed linear relationship between stimulus and neural response holds. However, the stimulus-response function of neurons is highly nonlinear, and information estimation with a linear method may lead to an underestimation of the true information rate. Recent experimental studies (Warland et al., 1997; Hatsopoulos et al., 2004), which used linear and nonlinear methods for the decoding of the responses of neural ensemble, reported similar performance of these two methods. Nevertheless, a thorough analysis of nonlinear decoding methods, which was beyond the scope of those studies, seems necessary.

In this contribution, we analyze a linear and a nonlinear decoding model with respect to how well they estimate the information rate from neural responses. We

consider responses of single neurons and pooled responses of populations with identical tuning. It was recently shown that pooling is an efficient way to extract the information from the population response (Shadlen et al., 1996; Panzeri et al., 2003; Arabzadeh et al., 2004) if the membrane potentials of the individual neurons of the population are only weakly correlated. We find that for aperiodic Gaussian stimuli, a linear decoding approach is sufficient to extract almost all of the information from the response of a single leaky integrate-and-fire (LIF) neuron, despite the neurons' strong nonlinear transfer function. Linear decoding, however, dramatically underestimates the information rate of pooled population responses at low noise levels. A nonlinear reconstruction method (as cf. a simple feed-forward neural network) is able to extract significantly more information from such responses.

We show that the difference between the linear and nonlinear method decreases either by increasing the frequency content of the stimuli to higher values or by increasing the strength of the membrane potential fluctuations. The former is a consequence of the dependency of the shape of the optimal linear decoding filter on the correlation structure of the input stimulus. We show that the reconstruction of the negative phase of stimuli with strong low frequency components fails leading to lower information rate estimates.

The later results from the linearization of the neurons transfer function by noise. It was recently shown in intracellular recordings *in vivo* that neocortical neurons have a strongly fluctuating membrane potential due to synaptic background activity (Paré et al., 1998; Anderson et al., 2000a). This synaptic activity not only enhances the responsiveness of neurons (Ho and Destexhe, 2000), but also facilitates the detection and transmission of weak signals (Wiesenfeld and Moss, 1995; Collins et al., 1996; Anderson et al., 2000a; Stacey and Durand, 2001). Using a biologically more realistic model of a population, which shows membrane potential fluctuations in the range typically observed in visual cells *in vivo*, the difference between the estimates of the linear and the nonlinear decoder decreases with increasing strength of membrane potential fluctuations, but the nonlinear decoder outperforms the linear decoder only if large enough populations are considered ($N_{pop} > 5$).

6.2. Materials and Methods

6.2.1. Population of Leaky Integrate-and-Fire Neurons

The first model of the neural population consists of N independent leaky integrate-and-fire (LIF) neurons. Each LIF neuron is characterized by its membrane potential

V , which changes in time according to the following differential equation:

$$C_m \frac{dV(t)}{dt} = -I_L + I_{stim}(t) + I_{bias} + D \frac{dW(t)}{dt}, \quad (6.1)$$

where $I_L = g_L(V(t) - E_L)$ is the leak current, $C_m = 0.5 \text{ nF}$ is the membrane capacitance, $g_L = 50 \text{ nS}$ is the leak conductance, $E_L = -70 \text{ mV}$ is the reversal potential, $I_{stim}(t)$ is the external signal, D is the diffusion coefficient, and $dW(t)$ is the infinitesimal increment of a Wiener process (Tuckwell, 1988). For a detailed description of the LIF model see Sec. 2.2.1.

The total input to each neuron was the sum of the input stimulus I_{stim} and the Gaussian white noise input, which had the same strength and was assumed to be independent across all neurons in the population. The time dependent input stimulus was generated by performing a fast Fourier transformation (FFT) of a white noise Gaussian process, then setting all values of the transformed process below a low (f_{low}) and above a high (f_{high}) cut-off frequency to zero, and then applying an inverse FFT to the latter. The standard deviation of the stimulus was set to $std(I_{stim}) = 0.1 \text{ nA}$ if not stated otherwise.

Throughout this paper we present results for two values of I_{bias} . First, we used a bias current of $I_{bias} = 0.65 \text{ nA}$, which leads to an average membrane potential (without spike process and reset) of $\langle V_m \rangle = -57 \text{ mV}$. For this bias current an input stimulus with $std(I_{stim}) = 0.1 \text{ nA}$ is totally sub-threshold. For the second bias current ($I_{bias} = 0.9 \text{ nA}$) the average membrane potential remains just below spike threshold ($\langle V_m \rangle = -52 \text{ mV}$), similar as reported in Anderson et al. (2000a). All simulations were done using the Euler integration scheme with an exact update equation [$dt = 0.1 \text{ ms}$] (Gillespie, 1996).

6.2.2. Population of Hodgkin-Huxley Neurons

To show the significance of the results derived with the LIF model, we made additional simulations with a biologically more realistic model of a neural population. The improved model differed from the LIF model with respect to the following two points: First, the LIF neurons were replaced by conductance based single-compartment models (adapted from Destexhe et al., 2001), which contained Hodgkin-Huxley type ion currents and synaptic conductances. Second, we introduced correlations between the membrane potentials of the neurons in the population by modeling the influence of the ongoing synaptic background activity on the neuron explicitly.

The membrane potential V of the Hodgkin-Huxley (HH) neurons changes in time according to the following differential equation:

$$C_m \frac{dV(t)}{dt} = -I_L - I_{Na} - I_K - I_M - I_{syn}(t) - I_{stim}(t), \quad (6.2)$$

where $I_L = g_L(V(t) - E_L)$ is the leak current, I_{Na} and I_K are the spike generating sodium and potassium currents and I_M is a non-inactivating potassium current for spike frequency adaptation. The HH model is described in detail in Sec. 2.2.2 and the intrinsic currents and othe model parameters are listed in Appendix A.

The influence of the synaptic activity on the neuron is described by the current I_{syn}

$$I_{syn}(t) = g_e(t)(V(t) - E_e) + g_i(t)(V(t) - E_i), \quad (6.3)$$

where $g_e(t)$ and $g_i(t)$ are the conductances of the excitatory (AMPA) and inhibitory (GABA_A) synapses, which were simulated as two-state kinetic models as described in Destexhe et al. (1994) and in Appendix B.

Each neuron in the population received 1000 excitatory and inhibitory Poisson spike trains through *AMPA* and *GABA_A* synapses. The conductances of the synapses were chosen such that the amplitude of the excitatory postsynaptic potential (EPSP) and the inhibitory postsynaptic potential (IPSP) matched the measurements of Markram et al. (1997) [EPSP peak value of 1.3 mV] and Tarczy-Hornoch et al. (1998) [IPSP peak value of -0.8 mV]. All simulations were done using the NEURON simulation environment (Hines and Carnevale, 1997).

In contrast to the LIF neuron, the standard deviation of the membrane potential of the HH neuron depends only weakly on the number of incoming spiking events, since the higher variability of spike count is counterbalanced by the simultaneous conductance increase, which leads to weaker postsynaptic potentials (Kuhn et al., 2004). High values of $\sigma_V >$ (e.g. $\sigma_V > 4\text{ mV}$) can only be achieved, if some of the synapses release simultaneously. Therefore, correlations between the release events were introduced as follows (Kuhn et al., 2003). The release events of single synapses were randomly chosen from a high density Poisson point process $x(t)$. In other words, the presynaptic spike train of a synapse is a thinned version of the high density point process. We use separate point processes for excitatory and inhibitory synapses. The count correlation coefficient c between two presynaptic spike train is then equal to P_{spk} (Kuhn et al., 2003), which is the probability of copying a pulse from $x(t)$ to the presynaptic spike train. Note that the rate of the high density point processes $x_{e,i}(t)$ is equal to $r_{e,i} = \frac{\lambda_{e,i}}{P_{spk}}$. A variation of P_{spk} in the range of $P_{spk} \in [0.0003, 0.0027]$ was

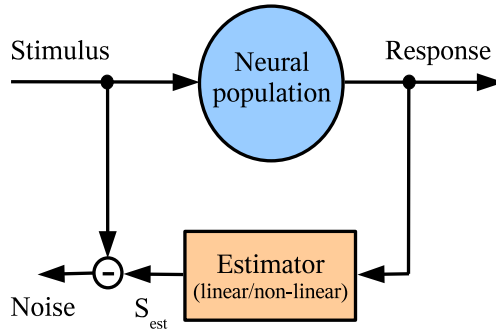


Figure 6.1.: Cartoon of a neural decoding method. The response of a single neuron or a neural population is used to reconstruct the input stimulus using an estimator, which minimizes the mean squared error between the stimulus and its estimate. From the remaining error (“noise”) a signal-to-noise ratio is calculated, which is used to estimate the information rate.

sufficient to adjust the standard deviation of the membrane potential to a reasonable range, e.g. $\sigma_V \in [3.5, 5.5] mV$. The firing rate of the excitatory background spike trains was set to $2 Hz$ and the inhibitory background firing rate was adjusted such that the average membrane potential of the neurons was approximately equal to $\langle V \rangle = -63 mV$. This led to inhibitory firing rates in the range of $1.4 Hz$ to $1.9 Hz$.

In addition, we introduced correlations between the membrane potentials of the neurons as follows. With the above described method we first generated a pool of presynaptic spike trains. After that, we distributed the spike trains randomly across the neurons such that the probability P_c that a pair of neurons in the population receive the same spike train was $P_c \sim 0.1$, which is in agreement with previously reported values (Braitenberg and Schüz, 1991; Hellwig et al., 1994).

6.2.3. Estimation of the Information Rate

Figure 6.1A shows the approach of linear and nonlinear decoding methods to estimate the information rate. In the first step, an estimator for the input stimulus is constructed based on the neurons’ (or the population) response. In the second step, the difference between the true and the estimated stimulus is used to calculate the information rate as will be described below in detail. Reconstruction approaches, however,

are based on many simplifying assumptions such that a validation with other more general methods is necessary.

Borst and Theunissen (1999) suggested using either the direct or the upper bound method depending on the data available. The direct method can be used to get an unbiased estimate of the average information rate (Strong et al., 1998; Borst and Theunissen, 1999; Reinagel and Reid, 2000). This method calculates the mutual information between stimulus and response based on an estimate of the probability distributions. If enough data is available, the direct method is the first choice for validation, which has been successfully applied to estimate the information transmission in single neurons (Strong et al., 1998; Reinagel and Reid, 2000). The direct method, however, is difficult to apply to populations of neurons, because the number of different spike patterns increases rapidly with population size and the probability of occurrence cannot be reliably determined.

The upper bound method (Borst and Theunissen, 1999), on the other hand, estimates the information rate from a frequency domain representation of mean response and neural noise and needs significantly less amount of data than the direct method. It is derived from the expected coherence. However, the bound is only tight if neuronal noise is additive and if the amplitudes of the Fourier-transformed response and noise traces are Gaussian distributed. At low noise levels, the input-output relationship of the neurons is highly nonlinear and the assumption of Gaussian distributed amplitudes does not hold, which leads to an overestimation of the true information (Haag and Borst, 1998; Borst and Theunissen, 1999). At high noise levels (linear regime), however, the estimates obtained with the linear and the upper bound method should be approximately the same. Thus a deviation between these methods indicates the nonlinear regime.

The Linear Reconstruction Method

The linear reconstruction method is introduced in detail in Sec. 2.4.2. The basic idea of this approach is to reconstruct an estimate of the stimulus S_{est} from the response and to calculate the information rate $I(S, S_{est})$ between the stimulus and this estimate with the help of a linear filter (Gabbiani, 1996; Rieke et al., 1997; Borst and Theunissen, 1999). To obtain the information rate between the input signal and the neural response, the following equation is used (cf. Sec. 2.4.2):

$$I_{lin} \geq -\frac{1}{2\pi} \int_0^\infty \log_2 [1 - \gamma^2(\omega)] d\omega, \quad (6.4)$$

where

$$\gamma^2(\omega) = \frac{|P_{SR}(\omega)|^2}{P_{SS}(\omega)P_{RR}(\omega)} \quad (6.5)$$

is the coherence between the stimulus and the response, $P_{SS}(\omega)$ and $P_{RR}(\omega)$ are the power spectra of the stimulus and the spike train, and $P_{SR}(\omega)$ denotes cross power spectrum between the stimulus and the spike train.

The coherence was calculated as follows. For each noise condition [different values of D , eq. (6.1)], we simulated the population of LIF neurons for 1000 s long with a temporal resolution of $dt = 0.2\text{ms}$. The whole response was then divided into approximately 1000 segments of 1 sec duration and transformed into frequency space. The power spectrum (P_{XX}) and the cross power spectrum (P_{XY}) were obtained by averaging the product of the respective Fourier-transformed segments, e.g. $P_{XY}(\omega) = \langle X(\omega)Y(\omega)^* \rangle$, where $*$ denotes the complex conjugate.

Reconstruction Using a Multilayer-Perceptron

Feedforward neural networks have been successfully applied both to predict the response of cortical neurons (Lau et al., 2002) and to decode spike trains from retinal ganglion cells (Warland et al., 1997) or from cortical cells (Hatsopoulos et al., 2004). Here we use a multilayer-perceptron to obtain an estimate of the input stimulus from the population response. Since data processing can not increase the information the response contains about the stimulus (Cover and Thomas, 1991), the estimate can be used the same way as described above, namely, to calculate a lower bound on the information rate:

$$I_{nn} \geq \frac{1}{2\pi} \int_0^\infty \log_2 \left[\frac{P_{SS}(\omega)}{P_{NN}(\omega)} \right] d\omega, \quad (6.6)$$

where P_{SS} is the power spectrum of the stimulus and P_{NN} is the power spectrum of the noise. We define noise as the difference between the stimulus and its estimate. The power spectra were calculated as described in the previous section.

The multilayer-perceptron consisted of one hidden layer and one linear output neuron (Fig. 6.2), whose value represents the estimate of the stimulus at time t . Each unit in the hidden layer had a sigmoidal activation function. There were 41 inputs to each neuron in the hidden layer, representing the number of spikes per bin of the pooled population response $r(t-20), r(t-19), \dots, r(t), \dots, r(t+20)$. The bin size was

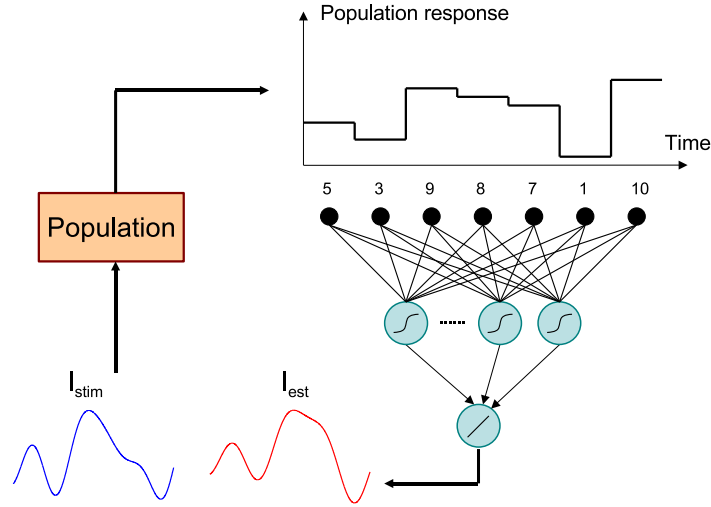


Figure 6.2.: Artificial neural network structure. Each neuron in the hidden layer receives 41 inputs, which represents the number of spikes in a 2ms interval of the pooled population response. The linear output neuron generates the estimate of the stimulus from the activation of the hidden neurons.

set to $T_b = 2\text{ms}$ and permitted the network to predict the stimulus $s_{est}(t)$ from a time window of $T_w = 82\text{ms}$, centered at time t .

For simplicity, we trained a separate network for each noise condition. However, the networks could be easily combined into a single network using a mixture of expert architecture (Jacobs et al., 1991). We used the back-propagation algorithm for the calculation of the Jacobian matrix, which was needed for the adjustment of the network weights according to the Levenberg-Marquardt optimization (Marquardt, 1963). The multilayer-perceptron was created and trained using the neural network toolbox from matlab.

We used a training set of approximately 50000 stimulus response pairs. A fraction of 30% of the data was used as validation set. Training was terminated either when the mean square error of the validation set failed to improve for 5 epochs (repetitions) in a row or the maximal number of epochs (100) was reached. To determine the proper number of hidden neurons and inputs, we trained networks with 4, 6, 8 and 10 hidden units, and 21, 31 and 41 inputs at three different noise conditions and six different combinations of I_{bias} and population size. The performance of the network did not significantly change with the number of hidden neurons but increased slightly with the

number of inputs. For one tested combination ($I_{bias} = 0.9 nA$, $N_{arr} = 1$ and $D = 0$) the increase in performance for increasing number of inputs was significant (t-test, alpha-level at 0.05). Thus we used a network with 41 inputs and 6 neurons in the hidden layer for all simulations in this study.

The Direct Method

This approach is based on the probability distribution of all possible words in the spike train, which is used to estimate the total entropy rate and the noise entropy rate. Following Strong et al. (1998), we calculated the information rate I ,

$$I = H(R) - H(R|S) \tag{6.7}$$

as the total entropy rate $H(R)$ of the response minus the conditional (noise) entropy rate $H(R|S)$ of the response given the stimulus, where the latter measures the variability of the response to repeated presentations of the same stimuli. A word w is a specific spike pattern in the response. It consists of L bins of duration T_b , where each bin contains the number of spikes, which occurred during the time interval T_b . T_b is generally much larger than the simulation time step dt . The total entropy of the spike train is then given by

$$H(L, T_b) = -\frac{1}{LT_b} \sum_w P(w) \log_2 P(w), \tag{6.8}$$

where $P(w)$ is the probability that a word w is observed in the response. Strong et al. showed, that the true entropy rate can be approximated by linearly extrapolating the estimate to infinite L .

The choice of the bin size critically affects the information rate estimation. Although a high temporal resolution is preferable, it also leads to a smaller maximum word length, because $P(w)$ cannot be reliably estimated given the amount of available data. Long range correlation in the response can usually not be taken into account at higher resolutions, because of the too short word length, which leads to an overestimation of the information rate. In the following, we used a bin size of $T_b = 4 ms$, because it yields information rates between the lower (linear decoder) and upper (see next section) bounds at high noise levels, where the integrate-and-fire models operate in an almost linear regime where bounds are tight.

Expected Coherence

Per definition, the coherence from eq. (6.5) lies between zero and one ($0 \leq \gamma^2 \leq 1$). A deviation from one can be attributed to either the nonlinearity of the neural system or the noise. To distinguish between these two causes, Haag and Borst (1998) suggested calculating an expected coherence γ_{exp}^2 for a linear system. Give a noise corrupted linear system, the response R is related to the input signal S via

$$R(\omega) = G_f(\omega)S(\omega) + N(\omega), \quad (6.9)$$

where $G_f(\omega) = \frac{P_{SR}(\omega)}{P_{SS}(\omega)}$ is the optimal linear forward filter. The expected coherence of a linear system is then related to the measured signal to noise ratio as follows (ω have been omitted for better readability):

$$\gamma_{exp}^2 = \frac{\langle S^* R \rangle \langle S R^* \rangle}{\langle S^* S \rangle \langle R^* R \rangle} \quad (6.10)$$

$$= \frac{\langle S^* (G_f S + N) \rangle \langle S (G_f^* S^* + N^*) \rangle}{\langle S^* S \rangle \langle (G_f^* S^* + N^*) (G_f S + N) \rangle} \quad (6.11)$$

$$= \frac{|G_f|^2 \langle S^* S \rangle^2}{\langle S^* S \rangle (|G_f|^2 \langle S^* S \rangle + \langle N^* N \rangle)} \quad (6.12)$$

$$= \frac{|G_f|^2 \langle S^* S \rangle}{|G_f|^2 \langle S^* S \rangle + \langle N^* N \rangle}. \quad (6.13)$$

Since the signal in the signal to noise ratio is the average response, the above relation turns into:

$$\gamma_{exp}^2 = \frac{SNR}{1 + SNR}. \quad (6.14)$$

The SNR can be obtained from the average population response for many repetitions of the same stimulus (signal) and the variance of the responses around the conditional mean (noise) after transforming them into frequency space.

The deviation of the expected coherence from one ($1 - \gamma_{exp}^2$) is caused by the noise and a difference between the expected and the measured coherence ($\gamma_{exp}^2 - \gamma^2$) is a result of the nonlinearity of the neural system. If the average response and the noise are Gaussian distributed, the expected coherence can be used to calculate an upper bound on the information rate from (Haag and Borst, 1998; Borst and Theunissen, 1999)

$$I_{UB} = \int_0^\infty \frac{d\omega}{2\pi} \log_2 [1 - \gamma_{exp}^2(\omega)]. \quad (6.15)$$

We use the upper bound in the following to indicate regions, where information transmission through the population is highly nonlinear. For a more detailed description of this approach see Borst and Theunissen (1999).

6.3. Results

In the following, we demonstrate how much information the response of a single integrate-and-fire model neuron conveys about temporary varying stimuli and how pooling affects the estimates of the information rate.

6.3.1. The Single LIF Neuron

Figure 6.3 shows the result obtained with the four different estimation methods described in Sec. 6.2.3 for a single LIF neuron. We used two different classes of stimuli: a low frequency input signal ($f_{stim} \in [0, 20] Hz$, Fig. 6.3A,C) and a stimulus with a frequency range of $f_{stim} \in [20, 40] Hz$ (Fig. 6.3B,D), which we refer to as low and high frequency signals in the following. In Fig. 6.3A the information rate is plotted against the standard deviation of the membrane potential [which is changed by varying the strength D of the Wiener process in eq. (6.1)] for the low frequency signal and a bias current of $I_{bias} = 0.9 nA$. The blue square line shows the information rate estimated with the linear method. For large values of the noise ($\sigma_V > 1.5 mV$), the blue square line is close to the upper bound (green dashed line) which indicates that the LIF neuron operates in a nearly linear regime. For lower noise values, the linear estimate deviates from the upper bound (which diverges for $\sigma_V \rightarrow 0$), but the results obtained with the direct method (black solid line) indicate that the upper bound overestimates the information rate. The upper bound becomes less tight, because the mean response and the additive noise are no longer Gaussian distributed and because the fluctuations of the response around its mean vanish for $\sigma_V \rightarrow 0$. Despite the remaining difference between the linear estimate (blue square line) and the direct method (black solid curve) for $\sigma_V < 1.5 mV$, which indicates that the LIF neuron is no longer well described by a linear system, the *nonlinear* neural network method (red circle line) fails to extract more information from the response as the linear method.

Figure 6.3B shows corresponding estimates of the information rate for the high frequency signal (same bias current). The region where the linear method (blue square line) is able to extract almost all information from the response is expanded to lower values of σ_V ($\sigma_V \geq 0.8 mV$). For $\sigma_V < 0.8 mV$, there are marked differences between

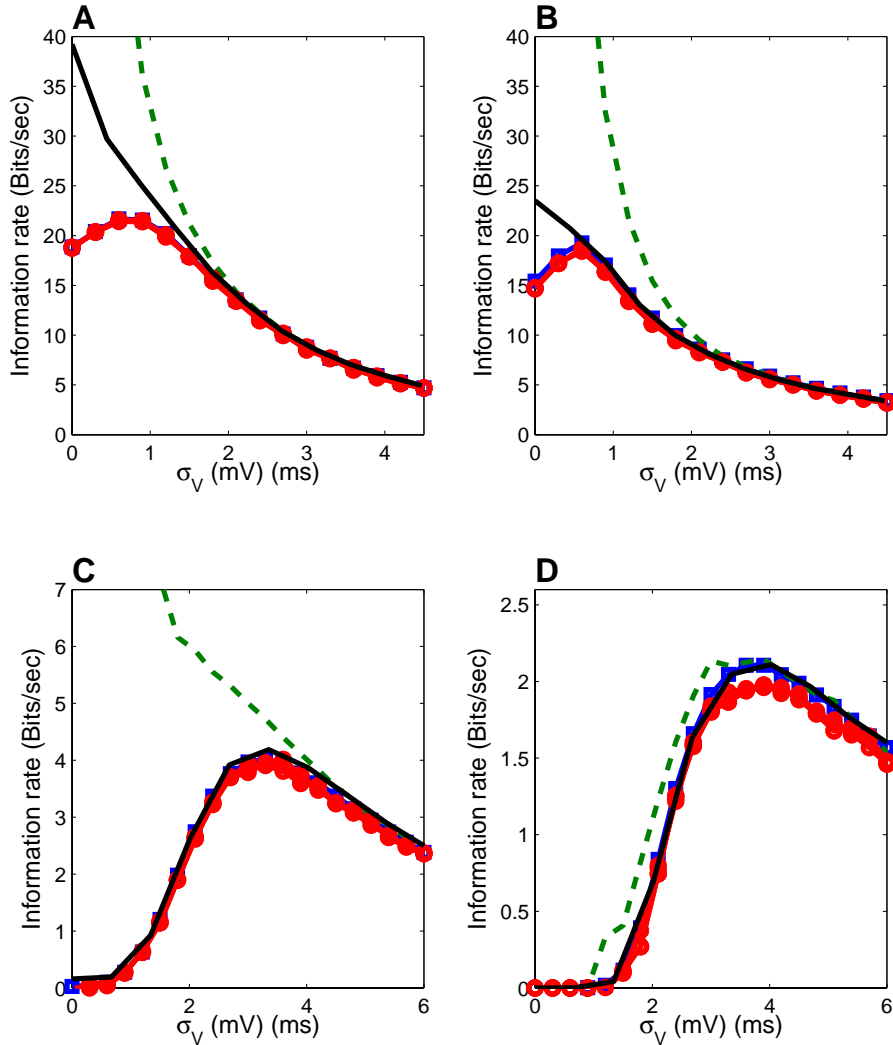


Figure 6.3.: Comparison of four different estimation techniques for the information rate for a LIF neuron. The figures show the information rate as a function of the standard deviation σ_V of the membrane potential for the linear reconstruction method (LM; blue square lines), the neural network based estimator (NN; red circle lines), the direct method (DM; black solid lines), and the upper bound method (UB; green dashed lines). A) Low frequency signal ($f_{stim} \in [0, 20] Hz$) and $I_{bias} = 0.9 nA$, leading to $\langle V_m \rangle = -52 mV$ (spike threshold at $V_{th} = -50 mV$). B) High frequency signal ($f_{stim} \in [20, 40] Hz$) and $I_{bias} = 0.9 nA$. C) Low frequency signal as in A), but $I_{bias} = 0.65 nA$ leading to $\langle V_m \rangle = -57 mV$. D) High frequency signal as in B), but $I_{bias} = 0.65 nA$. For the other simulation parameters see Sec. 6.2.1.

the linear and the direct method, but - as before - the neural network is not able to extract more information from the response in this regime.

Figure 6.3C shows the results for the four different estimation methods of Sec. 6.2.3 for the same low frequency stimulus as in Fig. 6.3A, but for a bias current of $I_{bias} = 0.65 \text{ nA}$, for which the input stimulus was nearly sub-threshold the whole time. The upper bound method (green dashed curve) still diverges for $\sigma_V \rightarrow 0$, but the differences between the linear and the direct methods now vanish. The same remains true for the high frequency signal (Fig. 6.3D), but now the upper bound remains tight and no longer diverges for $\sigma_V \rightarrow 0$, because the signal power decreases faster than the noise power in this limit. This means that the LIF neuron now behaves like a linear system for all values of σ_V . The estimate of the neural network is slightly reduced, which results from the small time window used for the estimation of the information rate. While correlations between response bins vanish quickly with distance, the estimate of the linear method is based on a larger number of response bins than that of the neural network (depending on the number of bins used for the Fourier transform), which leads to a better estimate of the information rate at higher noise levels.

The information rate estimate of the linear and the neural network method is only close to the true information if the stimulus is well reconstructed and the noise in the reconstruction is Gaussian distributed (cf. Sec. 2.4.2). Exemplary, Fig. 6.4 shows the distribution of the noise amplitudes in frequency space of the linear (Fig. 6.4A) and the neural network (Fig. 6.4B) method for the low frequency signal ($f_{stim} \in [0, 20] \text{ Hz}$). The noise was defined as the difference between the stimulus and its estimate, which was reconstructed from the response of a single neuron after stimulation with $I_{bias} = 0.65 \text{ nA}$ and $\sigma_V = 2 \text{ mV}$. The noise amplitudes were normalized by mean and standard deviation of the noise at that frequency. The Fig. shows that the noise distribution is well fit by a Gaussian distribution (black dotted curve). Furthermore, we used a χ^2 -test to analyze whether the noise distribution follows a Gaussian distribution. Figure 6.4C shows the χ^2 -value as a function of frequency for the linear (blue solid curve) and the neural network (red dashed curve) reconstruction method. For both methods the χ^2 -values are well below the threshold value of a significance level of $\alpha = 0.01$, which means that the null hypothesis of Gaussian distributed noise amplitudes can not be rejected. For $\sigma_V < 2 \text{ mV}$ we occasionally find χ^2 -values, which are above the threshold value. We conclude from this analysis that a deviation between the true information rate $I(R, S)$ and the estimated information rate between the stimulus and its estimate $I(S, S_{est})$ is a result of a bad reconstruction of the stimulus and not due to a non-Gaussian distribution of the noise amplitudes.

Taken together, our results show that although LIF neurons have a highly nonlinear transfer function, a linear reconstruction method can extract almost all information

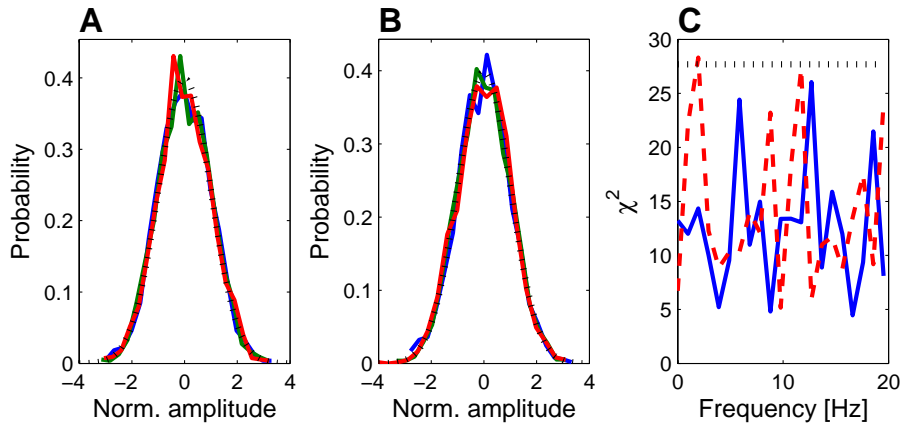


Figure 6.4.: A) Distribution of noise amplitudes of the linear method in frequency space at $f = 5 \text{ Hz}$ (blue curve), $f = 10 \text{ Hz}$ (green curve), and $f = 15 \text{ Hz}$ (red curve). The noise amplitudes were normalized by mean and standard deviation of the noise at that frequency and are well fit by a Gaussian distribution (black dotted line). B) The same as in A) but for the neural network method. C) χ^2 -value as a function of frequency for the linear (blue solid curve) and the neural network (red dashed curve) reconstruction method. The threshold value for the rejection of the null hypothesis of Gaussian distributed noise amplitudes ($\alpha = 0.01$) is indicated by the black (dotted) line. The neuron was stimulated with the low frequency signal ($f_{stim} \in [0, 20] \text{ Hz}$, $I_{bias} = 0.65 \text{ nA}$, and $\sigma_V = 2 \text{ mV}$). For the other simulation parameters see Sec. 6.2.1.

from the neural response - except for very low noise levels - and thus provides a reliable estimate of the information rate. However, this no longer holds for pooled population responses as we will show in the following.

6.3.2. Population of LIF Neurons

Figure 6.5A shows the information rate as a function of the standard deviation of the membrane potential for the same stimuli and bias currents as in Fig. 6.3A, but for a population consisting of 200 neurons. The Fig. shows the results for the linear method (blue square line), the neural network method (red circle line), and the upper bound method (green dashed line). The direct method can no longer be applied because of insufficient data. Without any background noise, the information rate is exactly the same as for the single neuron because all neurons in the population generate spikes at exactly the same time. For intermediate values of σ_V , however, the

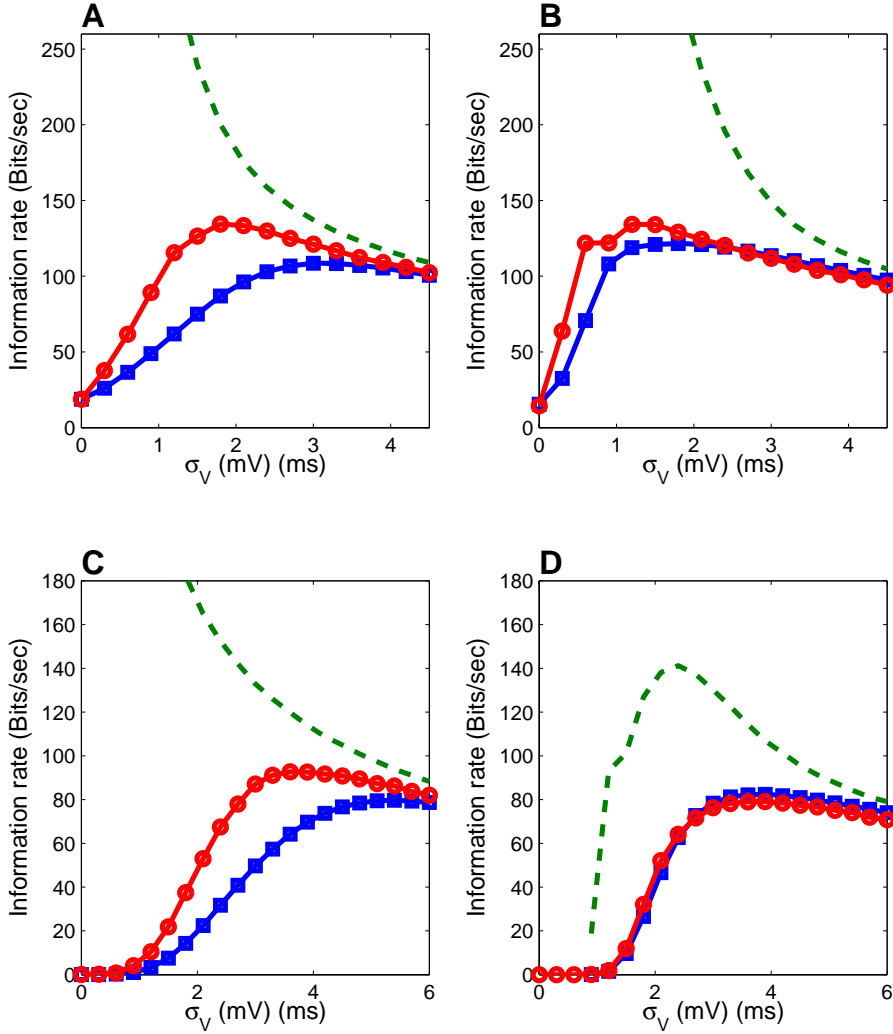


Figure 6.5.: Comparison of three different estimation techniques for the information rate for the pooled response of a population of 200 LIF neurons. The figures show the information rate as a function of the standard deviation σ_V of the membrane potential for the linear reconstruction method (LM; blue square lines), the neural network based estimator (NN; red circle lines), and the upper bound method (UB; green dashed lines). A) Low frequency signal ($f_{stim} \in [0, 20] Hz$) and $I_{bias} = 0.9 nA$, leading to $\langle V_m \rangle = -52 mV$ (spike threshold at $V_{th} = -50 mV$). B) High frequency signal ($f_{stim} \in [20, 40] Hz$) and $I_{bias} = 0.9 nA$. C) Low frequency signal as in A), but $I_{bias} = 0.65 nA$ leading to $\langle V_m \rangle = -57 mV$. D) High frequency signal as in B), but $I_{bias} = 0.65 nA$. For the other simulation parameters see Sec. 6.2.1.

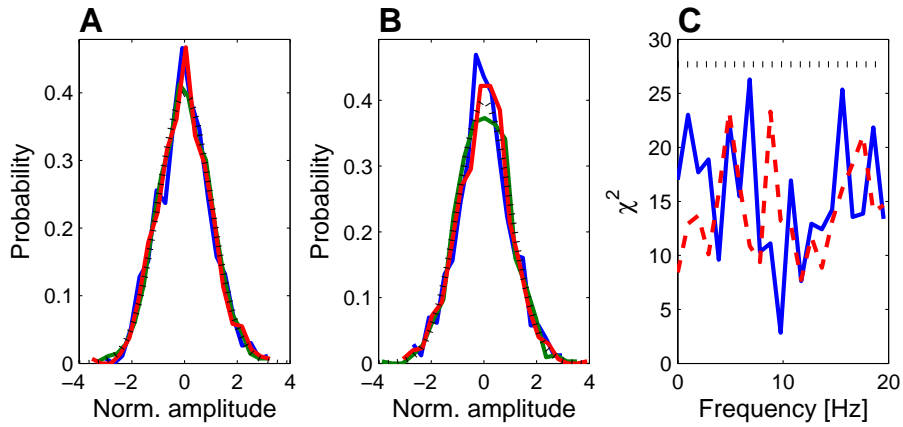


Figure 6.6.: A) Distribution of noise amplitudes of the linear method in frequency space at $f = 5 \text{ Hz}$ (blue curve), $f = 10 \text{ Hz}$ (green curve), and $f = 15 \text{ Hz}$ (red curve). The noise amplitudes were normalized by mean and standard deviation of the noise at that frequency and are well fit by a Gaussian distribution (black dotted line). B) The same as in A) but for the neural network method. C) χ^2 -value as a function of frequency for the linear (blue solid curve) and the neural network (red dashed curve) reconstruction method. The threshold value for the rejection of the null hypothesis of Gaussian distributed noise amplitudes ($\alpha = 0.01$) is indicated by the black (dotted) line. The population ($N = 200$) was stimulated with the low frequency signal ($f_{stim} \in [0, 20] \text{ Hz}$, $I_{bias} = 0.65 \text{ nA}$, and $\sigma_V = 2 \text{ mV}$). For the other simulation parameters see Sec. 6.2.1.

information transmission of the population is greatly improved. Like for the single neuron case, there is a large discrepancy between the information rate estimate of the linear method (blue square line) and the upper bound (green dashed line) for small values of σ_V . The value of σ_V , above which the population behaves like a linear system, however, is $\sigma_V \sim 5 \text{ mV}$ and twice as high, than for the single LIF neuron. The neural network, however, is now able to extract up to three times as much information from the population response as the linear reconstruction method. This effect is even more pronounced for sub-threshold stimuli (Fig. 6.5C). For the high frequency stimulus, the result remains qualitatively similar, but the information rate estimated with the linear method is closer to the upper bound for small values of σ_V (Fig. 6.5B,D) and to the estimate obtained with the neural network. Therefore, in contrast to the single LIF neuron, the nonlinear method outperforms the linear reconstruction method substantially for almost all values of σ_V .

Fig. 6.6 shows the distribution of the noise amplitudes in frequency space for the

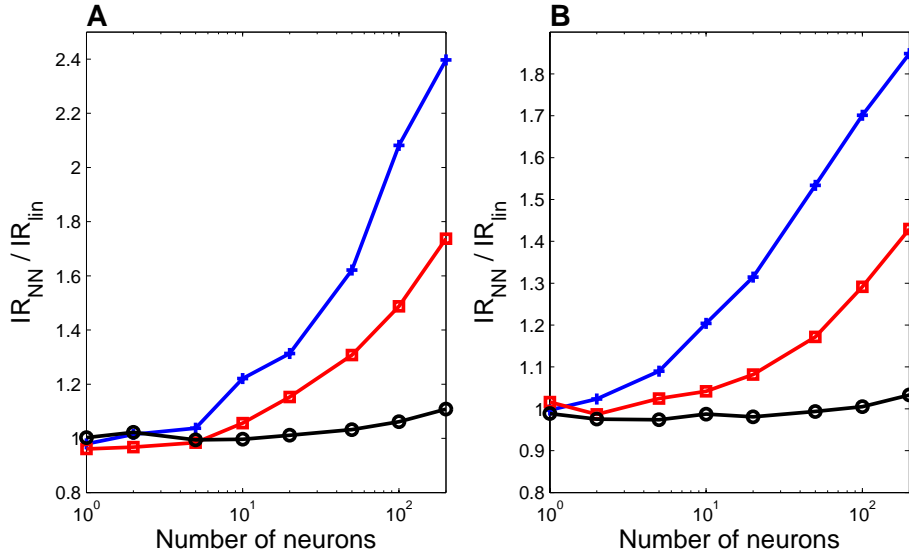


Figure 6.7.: A) Ratio between the information rate estimated by the neural network (I_{nn}) and the linear reconstruction method (I_{lin}) as a function of the number of neurons in the population for the low frequency signal ($f_{stim} \in [0, 20] Hz$). The different curves show the results for $\sigma_V = 2 mV$ (blue cross), $\sigma_V = 3 mV$ (red square), and $\sigma_V = 5 mV$ (black circle). The bias current was set to $I_{bias} = 0.65 nA$. B) Same as in A) but for $I_{bias} = 0.9 nA$. The different curves show the results for $\sigma_V = 1 mV$ (blue cross), $\sigma_V = 2 mV$ (red square), and $\sigma_V = 4 mV$ (black circle). For other simulation parameters see Sec. 6.2.1.

linear (Fig. 6.6A) and the neural network (Fig. 6.6B) method. The noise was defined as the difference between the stimulus and its estimate, which was reconstructed from the population response ($N = 200$) after stimulation with the low frequency signal ($f_{stim} \in [0, 20] Hz$; $I_{bias} = 0.65 nA$ and $\sigma_V = 2 mV$). The noise amplitudes were normalized by mean and standard deviation of the noise at that frequency. The Fig. shows that the noise distribution is well fit by a Gaussian distribution (black dotted curve). A χ^2 -test revealed (Fig. 6.6C) that the null hypothesis of Gaussian distributed noise amplitudes can not be rejected at a significance level of $\alpha = 0.01$. For $\sigma_V < 2 mV$ we find occasionally for both methods χ^2 -values, which are above the threshold value. Thus the deviation between the neural network and the linear estimate is mainly a result of the better reconstruction of the stimulus by the neural network method.

Figure 6.7A shows the ratio between the information rate estimate of the neural network and the linear method as a function of the number of neurons in the population

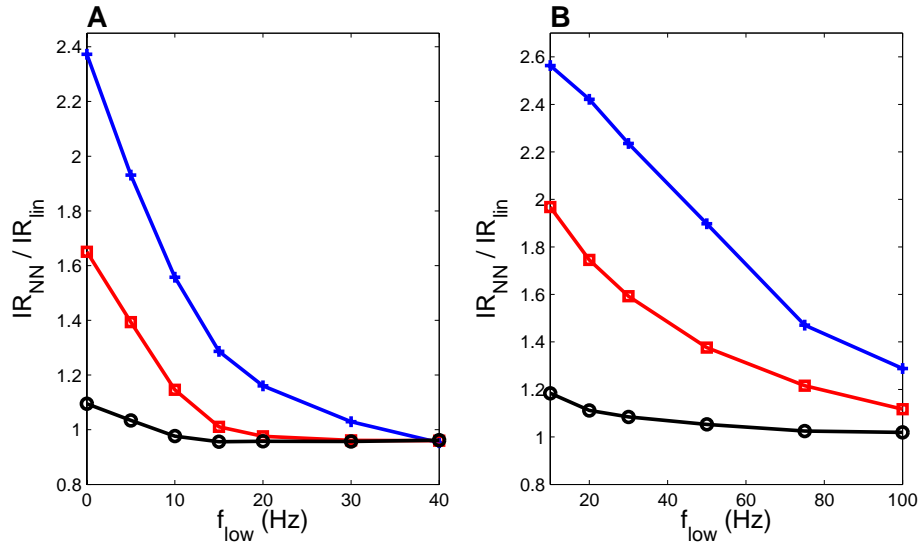


Figure 6.8.: A) Ratio between the information rate estimated by the neural network (I_{nn}) and the linear reconstruction method (I_{lin}) as a function of the lower cut-off frequency f_{low} of the stimulus (bandwidth of the stimulus was 20 Hz). B) Ratio between the information rate estimated by the neural network (I_{nn}) and the linear reconstruction method (I_{lin}) as a function of the bandwidth of the stimulus ($f_{low} = 0\text{ Hz}$). In both Figures, the different curves show the results for $\sigma_V = 2\text{ mV}$ (blue cross), $\sigma_V = 3\text{ mV}$ (red square), and $\sigma_V = 5\text{ mV}$ (black circle). The bias current was set to $I_{bias} = 0.65\text{ nA}$. For other simulation parameters see Sec. 6.2.1.

($f_{stim} \in [0, 20]\text{ Hz}$; $I_{bias} = 0.65\text{ nA}$). At a low standard deviation of the membrane potential (blue cross curve; $\sigma_V = 2\text{ mV}$), the neural population works in a highly nonlinear regime and the neural network method outperforms the linear method even at small population sizes ($\frac{I_{R_{NN}}}{I_{R_{lin}}} > 1.2$ for $N > 10$). Increasing σ_V (red square and black circle curve), however, leads to a decrease of the ratio towards one, which is a result of the linearization of the response characteristic of the neuron (cf. Sec. 6.2.1). For an average membrane potential quite below threshold (Fig. 6.7B; $I_{bias} = 0.9\text{ nA}$), we find the same dependency of the ratio on population size at slightly smaller values of σ_V (see Fig. caption).

Interestingly, we find that the ratio between the information rate estimate of the neural network and the linear method depends more critically on the spectral composition of the input signal. Figure 6.8A shows the ratio as a function of the lower cut-off frequency of the bandpass filtered white noise stimulus for $\sigma_V = 2\text{ mV}$ (blue

cross), $\sigma_V = 3\text{ mV}$ (red square), and $\sigma_V = 5\text{ mV}$ (black circle) as before. During these simulations the bandwidth of the stimulus was kept constant at 20 Hz , but the frequency band was shifted to higher values ($f_{low} \in [0, 40]\text{ Hz}$). The Fig. shows nicely that the neural network method leads to higher information rate estimates only for stimuli with low frequency content. A shift of the frequency band of the stimulus to higher values immediately leads to a reduction of the difference between the linear and the nonlinear method. For stimuli with $f_{low} > 30\text{ Hz}$, the linear method leads approximately to the same information rate estimates as the neural network, even at the highly nonlinear regime (blue cross curve; $\sigma_V = 2\text{ mV}$).

Moreover, the ratio also depends strongly on the stimulus bandwidth. Figure 6.8B shows the ratio between the information rate estimate of the neural network and the linear method as a function of the stimulus bandwidth $B \in [10, 100]\text{ Hz}$ ($f_{low} = 0\text{ Hz}$; $I_{bias} = 0.65\text{ nA}$) for $\sigma_V = 2\text{ mV}$ (blue cross), $\sigma_V = 3\text{ mV}$ (red square), and $\sigma_V = 5\text{ mV}$ (black circle). An increase in bandwidth leads to higher information rate estimates of both methods. The information rate of the linear method, however, increases faster with increasing B than does the neural network method, which leads to the observed decrease of the ratio. The low estimates of the linear method at small values of σ_v are a result of a bad reconstruction of the stimulus, as we will show in the next section. Additional data obtained for even stronger input signals ($std(I_{stim}) = 0.2\text{ nA}$) yielded similar results.

The Linear Reconstruction Filter

Although the firing rates of the LIF neurons in the population are smaller for the high than for the low frequency stimulus, the information rate estimated with the linear method is much higher (Fig. 6.5C,D; $\sigma_V \in [1.5, 6]\text{ mV}$). This unexpected higher efficiency in stimulus encoding (information per spike) is a result of the inability of the linear filter to reconstruct the negative phase of the stimulus well, which leads to an increase of the noise power.

Figure 6.9 shows histograms of the reconstruction error for different σ_V (see Fig. caption). For the low frequency signal (Fig. 6.9A), one obtains a skewed distribution (towards negative values) at small values of σ_V (blue dotted line), which results to an increase in noise power and thus to a lower information rate estimate. The distribution becomes narrower and more symmetric as σ_V is increased. For the high frequency signal (Fig. 6.9B), however, the histogram is less skewed and more narrow for the corresponding values of σ_V , which leads to higher estimates of the information rate. Figures 6.9C and D show the corresponding histograms of the reconstruction error

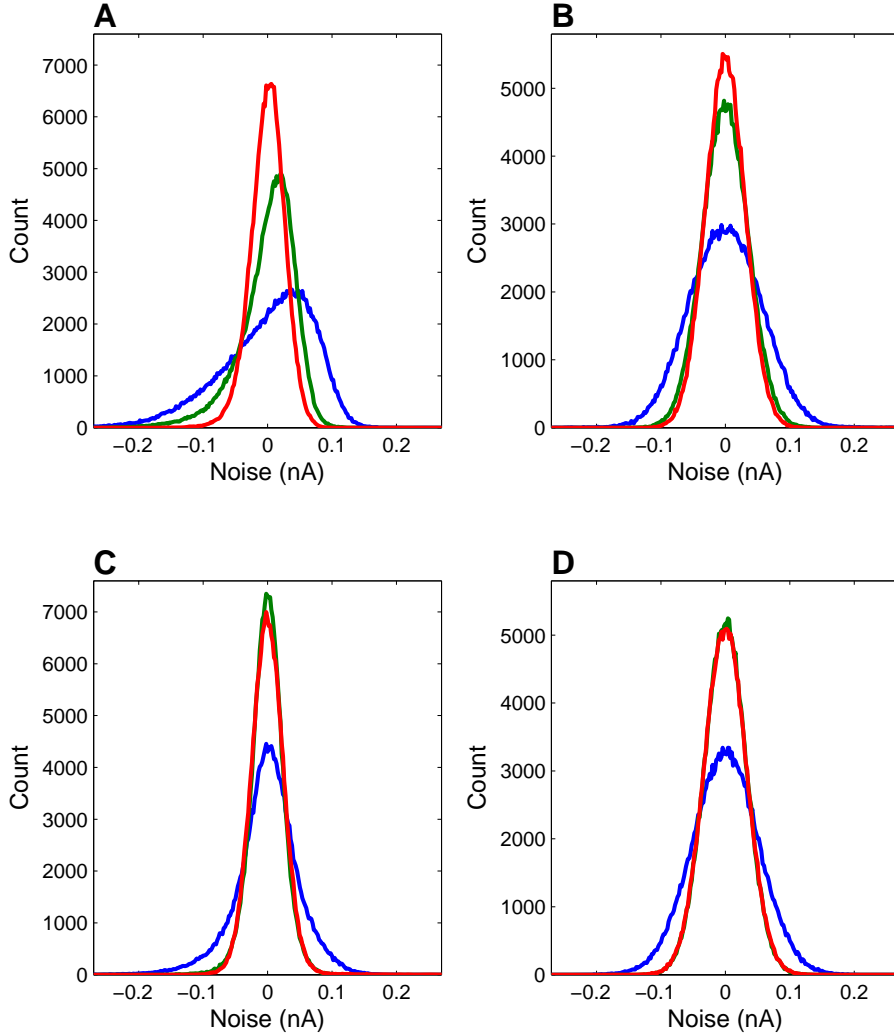


Figure 6.9.: Histograms of the reconstruction error of the linear and the neural network reconstruction methods for $\sigma_V = 2 mV$ (blue dotted line), $\sigma_V = 4 mV$ (black dashed line), and $\sigma_V = 6 mV$ (red solid line). A) Low frequency signal ($f_{stim} \in [0, 20] Hz$) and linear reconstruction. B) High frequency signal ($f_{stim} \in [20, 40] Hz$) and linear reconstruction. C) Low frequency signal ($f_{stim} \in [0, 20] Hz$) and neural network reconstruction. D) High frequency signal ($f_{stim} \in [20, 40] Hz$) and neural network reconstruction. For the other simulation parameters see Sec. 6.2.1.

for the nonlinear method. In comparison with the linear method, the neural network provides a better reconstruction for both stimuli at small values of σ_V , which explains the higher information rate estimates at corresponding values of σ_V . At high values of σ_V (red solid lines), however, the population operates almost in the linear regime, and thus linear reconstruction leads to a slightly lower reconstruction error than does the nonlinear method.

Figure 6.10 shows the reconstruction filter for the low (Fig. 6.10A) and the high (Fig. 6.10B) frequency signal, respectively. The filter obtained from the high frequency signal has a much more pronounced negative component than the filter obtained from the low frequency signal. Hence, when the stimulus is reconstructed and each spike in the response is replaced by a copy of the filter, the negative phase of the input stimulus is better reconstructed for the high frequency signal, which leads to a narrower noise distribution.

The linear filter is determined by the ratio of $P_{SR}(-\omega)$ and $P_{RR}(\omega)$ (cf. Sec. 2.4.2). If the power spectrum of the response $P_{RR}(\omega)$ is flat, then $h(\omega) \sim P_{SR}(-\omega)$, from which it follows that the shape of the linear filter is determined by the cross-correlation function $R_{sr}(\tau)$. Fig. 6.10C and D show the auto-correlation function $R_{ss}(\tau)$ of the stimulus (blue dotted curve), the cross-correlation function $R_{sr}(\tau)$ between the stimulus and the response (black dashed line), and the reconstruction filter normalized to the maximum of $R_{sr}(\tau)$ for the low and high frequency signal, respectively. The bias current was set to $I_{bias} = 0.65 \text{ nA}$ and the σ_V was low (e.g. $\sigma_V = 2 \text{ mV}$). In both Fig., the shape of linear filter is close to the shape of the cross-correlation function $R_{sr}(\tau)$, which indicates that the above assumption of a flat $P_{RR}(\omega)$ holds approximately. In the linear regime, the cross-correlation function is related to the auto-correlation of the stimulus through

$$R_{sr}(\tau) = (g * R_{ss})(-\tau), \tag{6.16}$$

where the symbol $*$ denotes convolution and where g is the linear transfer function of the neural systems, which predicts the instantaneous firing rate f from the stimulus s via the relation $f(t) = (g * s)(t)$. In the nonlinear regime, eg. (6.16) holds up to a constant factor if the stimulus is Gaussian and if the nonlinear relation between the stimulus and the response is well described by a static nonlinear function [Bussgang's theorem; see Koch (1998) for further details]. Thus we conclude that the unbalanced shape of the linear filter is mainly determined by the correlation structure of the stimulus.

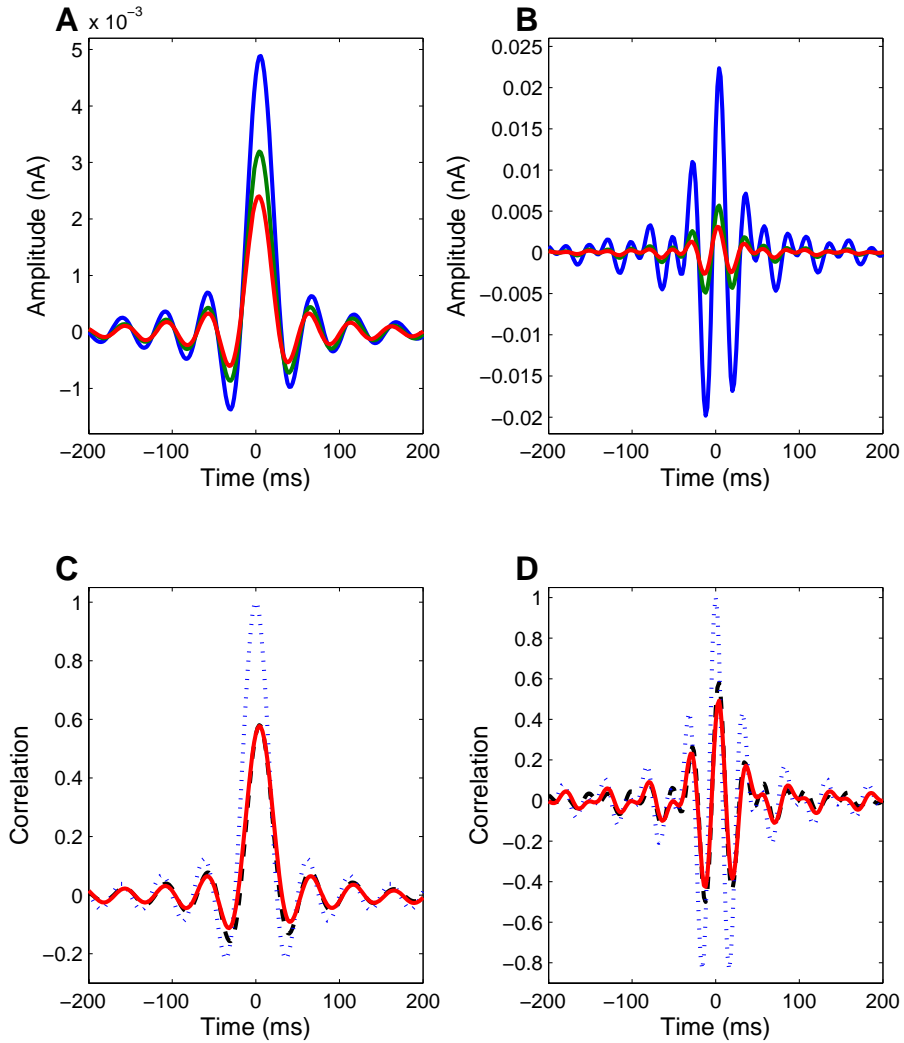


Figure 6.10.: A) Optimal linear reconstruction filters obtained from the pooled response of a population of 200 LIF neurons after stimulation with the low frequency signal ($f \in [0 - 20] \text{ Hz}$) for different background noise levels (blue dotted line: $\sigma_V = 2 \text{ mV}$, black dashed line: $\sigma_V = 3 \text{ mV}$, and red solid line: $\sigma_V = 5 \text{ mV}$). B) Same as in A) but for the high frequency signal ($f \in [20 - 40] \text{ Hz}$). C) Comparison of the linear filter (red solid line) with the auto-correlation function of the stimulus (blue dotted line) and the cross-correlation function between the stimulus and the response (black dashed line) for the low frequency signal ($\sigma_V = 2 \text{ mV}$). D) Same as in C) but for the high frequency signal. In all figures the bias current was set to $I_{bias} = 0.65 \text{ nA}$. For other simulation parameters see Sec. 6.2.1.

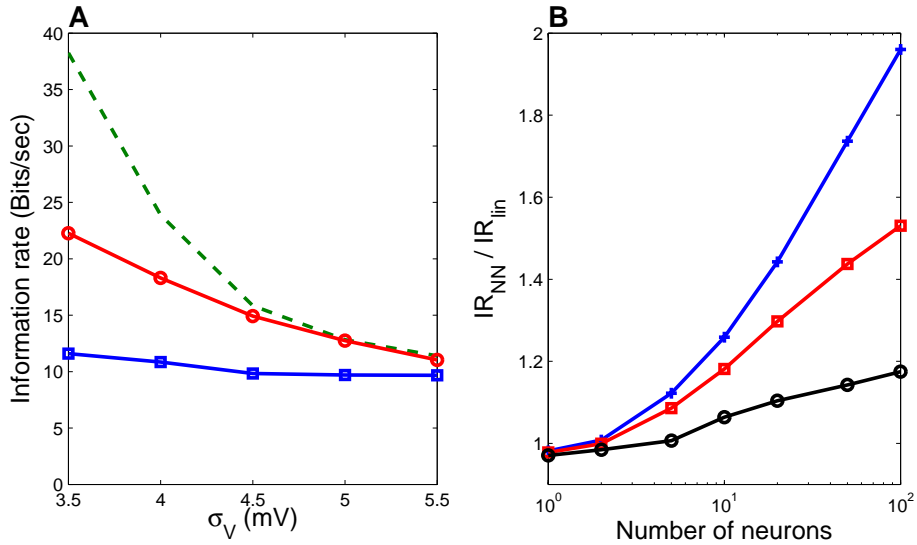


Figure 6.11.: A) Comparison of three different estimation techniques for the information rate for the pooled response of a population of 100 HH neurons. The figures show the information rate as a function of the standard deviation σ_V of the membrane potential for the linear reconstruction method (LM; blue square line), the neural network based estimator (NN; red circle line), and the upper bound method (UB; green dashed line). B) Ratio between the information rate estimated by the neural network (I_{nn}) and the linear reconstruction method (I_{lin}) as a function of the number of neurons in the population for $\langle V_m \rangle = -63$ mV and $\sigma_V = 3.5$ mV (blue cross line), $\sigma_V = 4.5$ mV (red square line), and $\sigma_V = 5.5$ mV (black circle line). For other simulation parameters see Sec. 6.2.2.

6.3.3. Population of Hodgkin-Huxley Neurons

In this section we investigate whether and under what conditions the predictions of the LIF population carry over to the biologically more realistic design of a population (see Sec. 6.2.2). Figure 6.11A shows the information rate as a function of the standard deviation of the membrane potential for a population consisting of 100 Hodgkin-Huxley neurons. As an input signal we used the same aperiodic Gaussian stimulus with bandwidth $f \in [0, 20]$ Hz, but with a slightly increased standard deviation ($std(I) = 0.3$ nA). As before, the Fig. shows the results of the linear method (blue square line), the neural network method (red circle line), and the upper bound method (green dashed line). For small values of σ_V , the neural network method is able to extract

twice as much information from the population response as the linear method. For increasing σ_V , however, the response behavior of the population becomes more linear, as a decrease of the deviation of the linear method to the upper bound indicates, and the performances of the linear method gets closer to that of the neural network.

Figure 6.11B shows how the ratio between the information rate, estimated with the neural network (I_{nn}) and the linear reconstruction method (I_{lin}), scales with the population size for three different values of σ_V (see Fig. caption). At low values of σ_V (blue cross line), the neural network method outperforms the linear method even at small population sizes ($N_{arr} > 5$), whereas at higher values of σ_V the ratio $\frac{I_{nn}}{I_{lin}}$ increases only slowly with population size.

6.4. Discussion

In this work we investigated different methods for information rate estimation from responses of single neurons and neural populations. We find that for a single leaky integrate-and-fire neuron, which was subjected to a weak (mostly sub-threshold) input signal, the linear reconstruction method performs almost optimally despite the neuron's strong nonlinear transfer function. Only at very low background activities ($\sigma_V < 1\text{ mV}$) do we find that the strong rectification of the input signal leads to a non-Gaussian distributed reconstruction error and thus to an underestimation of the information rate (cf. Sec. 2.4.2). Nonlinear reconstruction methods do not help in this case for the same reason. These results are in agreement with experimental findings (Warland et al., 1997), where the responses of retinal ganglion cells to time-dependent visual stimuli were analyzed with a linear filter and a neural network, and both methods lead to indistinguishable results.

However, if a population of LIF neurons is considered and if the information rate is estimated from a pooled response, the neural network based reconstruction consistently outperforms the linear method. The gap in performance between the linear and the nonlinear reconstruction method increases with population size and decreases for increasing values of σ_V . Furthermore, we have shown, that the low estimate of the information rate for the linear method arises from a poor reconstruction of the negative phase of the stimulus, because of the unbalanced shape of the optimal linear filter. The shape of the linear filter is mainly determined by the correlation structure of the stimulus. An increase or shift of the frequency content of the stimulus to higher values leads to a more balanced reconstruction filter and thus immediately reduces the difference in performance between the linear and the nonlinear method.

Additional simulations with a biologically more realistic model of a neural population of Hodgkin-Huxley neurons revealed the same discrepancy between the performance of the linear and the nonlinear reconstruction method. At low standard deviations of the membrane potential ($\sigma_V \sim 3.5 \text{ mV}$), the neural network was able to extract two times as much information from the pooled population response (100 HH neurons) than the linear method. The ratio between the two methods decreased to one with increasing values of σ_V .

Recently, the linear filter method was extended to multiple responses (Warland et al., 1997; Krahe et al., 2002), where the response r_i of neuron i of the population was convolved with an individual filter h_i :

$$S_{est}(t) = \sum_{i=1}^N \int_{-\infty}^{\infty} h_i(s) R_i(t-s) ds. \quad (6.17)$$

In the limiting case of identical tuning and identical response behavior, however, the linear filter of all neurons would be the same, and the above equation would simplify to

$$S_{est}(t) = \int_{-\infty}^{\infty} h_p(s) \sum_{i=1}^N R_i(t-s) ds, \quad (6.18)$$

where the linear filter h_p is obtained from the pooled response of the population. Thus we expect that our result will hold as long as the neurons in the population have similar response behavior and the driving input between neurons does not differ too much. Although these requirements may seem quite restrictive at first, they are also a prerequisite for the task of information transmission with ensembles of weakly correlated neurons. Since the firing of cortical cells is found to be highly irregular (Stevens and Zador, 1998; Buracas et al., 1998), it is likely that populations of neurons are involved to relay information reliably to higher brain areas. Indeed, recent experimental findings (Feldmeyer et al., 1999; Lübke et al., 2000) indicate that information transmission itself can play a major role in neural systems. There it has been suggested that spiny stellate and star pyramidal neurons in layer 4 of the *barrel field* in the rat somatosensory cortex amplify and relay thalamic input to different regions within the cortical column.

The presented results were obtained with white noise stimuli, which are widely used in experimental studies (Reinagel and Reid, 2000; Kim and Rieke, 2001; Krahe et al., 2002). These kind of stimuli differ markedly from natural stimuli, where the stimulus energy decreases for increasing temporal frequencies (Simoncelli and Olshausen, 2001).

However, we expect that such stimuli reveal the same discrepancy between the two methods, as the stimulus energy of the temporal frequency spectrum of natural scenes is mainly concentrated at low frequencies. Thus, a linear reconstruction method may not be appropriate for such stimuli and a nonlinear method should be preferred for the estimation of the information rate from the population response.

The presented results are remarkable with respect to another point. It was recently shown that pooling is an efficient mechanism for decoding stimulus information from population responses (Shadlen et al., 1996; Arabzadeh et al., 2004) - if the pooled neurons are only weakly correlated (Zohary et al.; 1994). In this case, however, our results suggest that an efficient readout system for the incoming spike trains has to be nonlinear at least for a fairly large range of values of the standard deviation of V_m . Recently, Polsky et al. (2004) suggested that pyramidal cells may act as three-layer neural networks. If such a nonlinear readout is indeed realized in a neural system, our results show that neurons can operate close to the optimum of information transmission.

A. The Hodgkin Huxley Neuron

Here we describe the model equations for the Hodgkin Huxley neuron used in chapter 3 and 6 in detail. For both models, the membrane potential is described by the following differential equation:

$$C_m \frac{\partial V}{\partial t} = -g_L(V - E_L) - I_{Na} - I_K - I_M - I_{syn}, \quad (\text{A.1})$$

where C_m is the membrane capacitance, g_L is the leak conductance, E_L is the resting membrane potential, I_{Na} and I_K are the spike generating sodium and potassium currents, I_M is a non-inactivating potassium current for spike frequency adaptation, and I_{syn} is the total synaptic current. The kinetic equations and their parameters were as follows:

Model neuron used in chapter 3

Here we describe the model equations for the conductance-based neuron, which were taken from a Wang and Buzsaki (1996) in detail (cf. chapter 3). They were adapted to bring the firing patterns and rates during stimulation, as well as, the shape of the generated action potentials closer to the experimental data. The membrane capacitance of the model neuron was set $C_m = 1 \mu F/cm^2$, the leak conductance was set to $g_L = 0.05 mS/cm^2$ and the resting membrane potential was set to $E_L = -75 mV$. The kinetic parameters of the voltage-dependent currents were as follows:

Voltage-dependent sodium current, I_{Na} :

$$\begin{aligned} I_{Na} &= \bar{g}_{Na} m_\infty^3 h (V - E_{Na}) \\ m_\infty &= \frac{\alpha_m(V)}{\alpha_m(V) + \beta_m(V)} \\ \frac{dh}{dt} &= \alpha_h(V) (1 - h) - \beta_h(V) h \end{aligned}$$

A. The Hodgkin Huxley Neuron

$$\begin{aligned}
 \alpha_m(V) &= \frac{-0.25(V + 41)}{\exp(-0.25[V + 41]) - 1} \\
 \beta_m(V) &= 4 \exp(-[V + 60]/18) \\
 \alpha_h(V) &= 0.07 \exp(-[V + 58]/20) \\
 \beta_h(V) &= \frac{1}{1 + \exp(-0.1[V + 28])}.
 \end{aligned}$$

Model parameters: $\bar{g}_{Na} = 25 \text{ mS/cm}^2$ and $E_{Na} = 55 \text{ mV}$.

Delayed-rectifier potassium current, I_K :

$$\begin{aligned}
 I_K &= \bar{g}_K n^4 (V - E_K) \\
 \frac{dn}{dt} &= \alpha_n(V) (1 - n) - \beta_n(V) n \\
 \alpha_n(V) &= \frac{-0.01(V + 54)}{\exp(-0.3[V + 54]) - 1} \\
 \beta_n(V) &= 0.15 \exp(-[V + 28]/30).
 \end{aligned}$$

Model parameters: $\bar{g}_K = 4 \text{ mS/cm}^2$ and $E_K = -90 \text{ mV}$.

Noninactivating potassium current, I_M :

$$\begin{aligned}
 I_M &= \bar{g}_M p (V - E_K) \\
 \tau_p \frac{dp}{dt} &= p_\infty(V) - p \\
 \tau_p(V) &= \frac{1000}{3.3 (\exp([V + 35]/40) + \exp(-[V + 35]/20)) T_{adj}} \\
 p_\infty(V) &= \frac{1}{1 + \exp(-[V + 35]/10)}.
 \end{aligned}$$

Model parameters: $\bar{g}_M = 1.2 \text{ mS/cm}^2$, $T_{adj} = 4.6555$, and $E_K = -90 \text{ mV}$.

Model neuron used in chapter 6

The membrane capacitance was set $C_m = 1 \mu F/cm^2$, the leak conductance was set to $g_L = 0.045 mS/cm^2$ and the resting membrane potential was set to $E_L = -80 mV$. The kinetic parameters of the sodium (I_{Na}) and the potassium currents ($-I_K, I_M$) were taken from a model of a cortical pyramidal cell, developed by Destexhe et al. (2001), and were as follows:

The voltage-dependent sodium current, I_{Na} :

$$\begin{aligned}
 I_{Na} &= \bar{g}_{Na} m^3 h (V - E_{Na}) \\
 \frac{dm}{dt} &= \alpha_m(V) (1 - m) - \beta_m(V) m \\
 \frac{dh}{dt} &= \alpha_h(V) (1 - h) - \beta_h(V) h \\
 \alpha_m(V) &= \frac{-0.32(V - V_T - 13)}{\exp[-(V - V_T - 13)/4] - 1} \\
 \beta_m(V) &= \frac{0.28(V - V_T - 40)}{\exp[-(V - V_T - 40)/5] - 1} \\
 \alpha_h(V) &= 0.128 \exp[-(V - V_T - V_S - 17)/18] \\
 \beta_h(V) &= \frac{4}{1 + \exp[-(V - V_T - V_S - 40)/5]}.
 \end{aligned}$$

Model parameters: $\bar{g}_{Na} = 36.1 mS/cm^2$, $V_T = -58 mV$ and $V_S = -10 mV$, $E_{Na} = 50 mV$.

Delayed-rectifier potassium current, I_K :

$$\begin{aligned}
 I_K &= \bar{g}_K n^4 (V - E_K) \\
 \frac{dn}{dt} &= \alpha_n(V) (1 - n) - \beta_n(V) n \\
 \alpha_n(V) &= \frac{-0.032(V - V_T - 15)}{\exp[-(V - V_T - 15)/5] - 1} \\
 \beta_n(V) &= 0.5 \exp[-(V - V_T - 10)/40].
 \end{aligned}$$

Model parameters: $\bar{g}_K = 7 mS/cm^2$ and $V_T = -58 mV$, $E_K = -90 mV$.

Noninactivating potassium current, I_M :

$$\begin{aligned}I_M &= \bar{g}_M p (V - E_K) \\ \frac{dp}{dt} &= \alpha_p(V) (1 - p) - \beta_p(V) p \\ \alpha_p(V) &= \frac{0.0001(V + 30)}{1 - \exp[-(V + 30)/9]} \\ \beta_p(V) &= \frac{-0.0001(V + 30)}{1 - \exp[(V + 30)/9]}.\end{aligned}$$

Model parameters: $\bar{g}_M = 0.5 \text{ mS/cm}^2$.

B. Two-state kinetic synapse model

In chapter 6 we generated the background activity using *AMPA* and *GABA_A* synapses. They were modeled as follows:

Model of the *AMPA*-synapses:

$$g_e(t) = \bar{g}_A \sum_{k=0}^{N_e} x_k(t)$$
$$\frac{dx_k(t)}{dt} = \alpha_A [T] (1 - x_k(t)) - \beta_A x_k(t).$$

Model parameters *AMPA*: $\bar{g}_A = 8.8 \text{ nS}$, $\alpha_A = 1.1 \frac{\text{mM}}{\text{ms}}$, $\beta_A = 0.67 \text{ ms}^{-1}$.

Model of the *GABA_A*-synapses:

$$g_i(t) = \bar{g}_G \sum_{k=0}^{N_i} y_k(t)$$
$$\frac{dy_k(t)}{dt} = \alpha_G [T] (1 - y_k(t)) - \beta_G y_k(t).$$

Model parameters *GABA_A*: $\bar{g}_G = 4.2 \text{ nS}$, $\alpha_G = 5 \frac{\text{mM}}{\text{ms}}$, $\beta_G = 0.18 \text{ ms}^{-1}$.

Kinetic parameters were taken from (Destexhe et al., 1994). The transmitter concentration $[T]$ was set to 1 mM at spike onset for a duration of 1 ms (rising phase), and 0 mM otherwise. The conductance of the synapse was adjusted such that a spike leads to an excitatory and inhibitory post synaptic potential of approximately 1.3 mV and -0.8 mV at a membrane potential of $V_m = 60 \text{ mV}$ (without synaptic background activity), respectively. The conductance values were chosen according to recent experimental findings (Markram et al., 1997; Tarczy-Hornoch et al., 1998).

C. Adjustment of synaptic background activity

The effect of the synaptic background activity on the membrane potential is usually described by the use of a synaptic current (cf. Sec. 2.3. In chapter 3 and 5 we used a more complex model of the synaptic background activity in order to include the effects of shot noise on the membrane potential distribution (cf. chapter 5) or to be able to adjust the spectral composition of the membrane potential to experimental data (cf. chapter 3).

Model of the synaptic background activity used in chapter 3

In chapter 3, the synaptic current described the synaptic input evoked by the visual stimulation as well as the background activity. The total synaptic current I_{syn} is given by

$$I_{syn}(t) = g_e(t)(V(t) - E_e) + g_i(t)(V(t) - E_i), \quad (\text{C.1})$$

where $E_e = 0 \text{ mV}$ and $E_i = -75 \text{ mV}$ are the reversal potentials of the excitatory and inhibitory currents.

The excitatory and inhibitory conductance traces consisted of a constant mean conductance \bar{G}_e and \bar{G}_i and a time dependent part $g_{e0}(t)$ and $g_{i0}(t)$. Visual stimulation was simulated by adding a sinusoidal conductance with amplitude g_s to the total excitatory conductance. The total excitatory and inhibitory synaptic conductance, $g_e(t)$ and $g_i(t)$, are then given by:

$$g_e(t) = \bar{G}_e + g_s \sin(2\pi ft) + g_{e0}(t), \quad (\text{C.2})$$

$$g_i(t) = \bar{G}_i + g_{i0}(t), \quad (\text{C.3})$$

where g_s determines the strength of the stimulation by a grating with a given temporal frequency (for example, $f = 3 \text{ Hz}$).

C. Adjustment of synaptic background activity

	Excitatory		Inhibitory		
	Optimal	Non-optimal	Optimal	Non-optimal	
g_s	0.079	0.018	-	-	mS/cm^2
\bar{G}	0.096	0.090	0.035	0.020	mS/cm^2
a_1	1.08	0.87	-	-	
a_2	0.31	0.24	0.15	0.15	
a_3	0.127	0.085	0.1	0.1	
b_1	400	200	-	-	ms
b_2	50	50	50	50	ms
b_3	2.2	2	2	2	ms

Table C.1.: Stimulus conductance g_s as well as the mean background conductance \bar{G} and parameters of $f(\omega)$ for the excitatory and inhibitory conductances $g_e(t)$ and $g_i(t)$. The parameters were used to reproduce the membrane potential of the neuron shown in Fig. 3.1A-F.

The time-dependent excitatory and inhibitory conductance traces, $g_{e0}(t)$ and $g_{i0}(t)$, were derived from a Gaussian white noise, which was filtered in Fourier space by multiplying the transferred conductance trace component-wise with a function $f(\omega)$:

$$f(\omega) = a_1 \exp(-\tau_1\omega) + a_2 \exp(-\tau_2\omega) + a_3 \exp(-\tau_3\omega), \quad (C.4)$$

in order to obtain a spectral composition of the membrane potential fluctuations similar to the experimental data.

Table C.1 lists the model parameters which were used to reproduce the spectral composition of the membrane potential shown in Fig. 3.1A-F. The table lists the stimulus conductance g_s as well as the mean background conductance and the parameters of the filter function $f(\omega)$ of $g_e(t)$ and $g_i(t)$ for optimal and non-optimal orientation. For all other orientations, the mean background conductance and the parameters for $f(\omega)$ were linearly interpolated between the listed parameters according to the value of the stimulus conductance g_s at that specific orientation. The stimulus conductance itself was adjusted such that the stimulus-power of the simulated voltage trace matched to the experimentally observed values.

Table C.2 lists the model parameters which were used to reproduce the average values of our experimental data sample (see Table 3.2). The alteration in stimulus or γ -power in the range of plus-minus one standard deviation of the experimentally observed values were achieved by either varying the stimulus conductance g_s (stimulus-

C. Adjustment of synaptic background activity

	Excitatory		Inhibitory		
	Optimal	Non-optimal	Optimal	Non-optimal	
g_s	0.067	0.014	-	-	mS/cm^2
\bar{G}	0.113	0.1	0.035	0.020	mS/cm^2
a_1	1.41	1.43	0	0	
a_2	0.24	0.18	0.15	0.15	
a_3	0.091	0.054	0.1	0.1	
b_1	220	220	0	0	ms
b_2	50	50	50	50	ms
b_3	1.5	1.2	2	2	ms

Table C.2.: Stimulus conductance g_s as well as the mean background conductance \bar{G} and parameters of $f(\omega)$ for the excitatory and inhibitory conductances $g_e(t)$ and $g_i(t)$. The parameters were used to reproduce the average values of our experimental data sample (see Table 3.2)

power) or the parameter α in eq. (3.8) (γ -power). The simulation time step was set to $dt = 0.05 ms$.

Model of the synaptic background activity used in chapter 5

In chapter 5, where we investigated how the detection performance of a population of LIF neurons depends on the statistical parameters of the membrane potential, we adapted the parameters of the excitatory and inhibitory synaptic conductances in order to alter mean, standard deviation and temporal correlation of the membrane potential in a biologically meaningful range.

The total synaptic current I_{syn} is given by:

$$I_{syn}(t) = g_e(t)(V_m(t) - E_e) + g_i(t)(V_m(t) - E_i), \quad (C.5)$$

where $g_e(t)$ and $g_i(t)$ are two fluctuating conductances driven by a Poisson process:

$$\tau_e \frac{dg_e}{dt} = -g_e + a_e \tau_e \sum_{t_{k_e}} \delta(t - t_{k_e}), \quad (C.6)$$

$$\tau_i \frac{dg_i}{dt} = -g_i + a_i \tau_i \sum_{t_{k_i}} \delta(t - t_{k_i}), \quad (C.7)$$

C. Adjustment of synaptic background activity

where τ_e and τ_i are the synaptic time constants, a_e and a_i are the quantal conductance amplitudes, t_{k_e} and t_{k_i} are the Poisson-distributed arrival times of the spikes generated by the background activity with rate f_e and f_i . Model parameters were: $g_{e0} = 12.6 \text{ nS}$, $g_{i0} = 50.3 \text{ nS}$, $\sigma_{e0} = 10.6 \text{ nS}$, $\sigma_{i0} = 23.2 \text{ nS}$, $\tau_{e0} = 2.7 \text{ ms}$, and $\tau_{i0} = 10.5 \text{ ms}$.

The excitatory and inhibitory background firing rate f_e and f_i as well as the quantal conductance amplitudes a_e and a_i were obtained by solving the following equations:

$$\langle g_e \rangle = a_e \tau_e f_e, \quad \sigma_e = a_e \sqrt{\frac{\tau_e f_e}{2}}, \quad (\text{C.8})$$

$$\langle g_i \rangle = a_i \tau_i f_i, \quad \sigma_i = a_i \sqrt{\frac{\tau_i f_i}{2}}. \quad (\text{C.9})$$

The values listed above lead to a fluctuating membrane potential with mean of $\langle V_m \rangle = -65.8 \text{ mV}$ and standard deviation of $\sigma_V = 4.5 \text{ mV}$ after spike removal. Different combinations of mean and standard deviation of the membrane potential were adjusted by varying $\bar{g}_e = \alpha g_{e0}$ ($\alpha \in [0.4, 4.9]$), $\sigma_e = \beta \sigma_{e0}$, and $\sigma_i = \beta \sigma_{i0}$ ($\beta \in [0.5, 3.2]$). To get the corresponding parameters α and β for a certain combination of $\langle V_m \rangle$ and σ_V , we first obtained $\langle V_m \rangle$ and σ_V for points in the two dimensional parameter space defined by α and β . After that, we derived the isoclines for the desired values of $\langle V_m \rangle$ and σ_V . The corresponding values for α and β can then be obtained from the intersection of the isoclines. Note that for each investigated combination of $\langle V_m \rangle$ and σ_V we only found one corresponding combination of α and β in the above stated range.

References

- Abeles M (1991) *Corticonics: neural circuits of the cerebral cortex*. Cambridge University Press.
- Alonso JM, Usrey WM and Reid RC (1996) Precisely correlated firing of cells in the lateral geniculate nucleus. *Nature* 383: 815-819.
- Anderson JS, Lampl L, Gillespie D, Ferster D (2000a) The contribution of noise to contrast invariance of orientation tuning in cat visual cortex. *Science* 290: 1968-1971.
- Anderson JS, Lampl I, Reichova I, Carandini M, Ferster D (2000b) Stimulus dependence of two-state fluctuations of membrane potential in cat visual cortex. *Nat. Neurosci.* 3(6): 617-621.
- Anderson JS, Carandini M, Ferster D (2000c) Orientation Tuning of Input Conductance, Excitation, and Inhibition in Cat Primary Visual Cortex. *J. Neurophysiol.* 84: 909-926.
- Arabzadeh E, Panzeri S, Diamond ME (2004) Whisker Vibration Information Carried by Rat Barrel Cortex Neurons. *J. Neurosci.* 24: 6011-6020.
- Attwell D, Laughlin SB (2001) An energy budget for signaling in the grey matter of the brain. *J. Cereb. Blood Flow Metab.* 21: 1133-1145.
- Averbeck BB, Lee D (2004) Coding and transmission of information by neural ensembles. *TRENDS Neurosci.* 27: 225-230.
- Azouz R, Gray CM (2003) Adaptive Coincidence Detection and Dynamic Gain Control in Visual Cortical Neurons *In Vivo*. *Neuron* 37: 513-523.
- Azouz R, Gray CM (2000) Dynamic spike threshold reveals a mechanism for synaptic coincidence detection in cortical neurons *in vivo*. *Proc. Nat. Acad. Sci.* 97: 8110-8115.
- Balasubramanian V, Kimber D, Berry MJ, 2nd (2001) Metabolically efficient information processing. *Neural Comput.* 13: 799-815.

- Benzi R, Suter A, Vulpiani A (1981) The mechanism of stochastic resonance. *J. Phys. A* 14: L453-L457.
- Bialek W, Rieke F, de Ruyter van Steveninck RR, Warland D (1991) Reading a neural code. *Science* 252: 1854-1857.
- Borg-Graham LJ, Monier C, Frenac Y (1998) Visual input evokes transient and strong shunting inhibition in visual cortical neurons. *Nature*, 393: 369-373.
- Borst A, Theunissen FE (1999) Information theory and neural coding. *Nat. Neurosci.* 2: 947-957.
- Braitenberg V, Schüz A (1991) *Anatomy of the cortex. Statistics and geometry.* Springer, Berlin.
- Bringuier V, Fregnac Y, Baranyi A, Debanne D, Shulz DE (1997) Synaptic origin and stimulus dependency of neuronal oscillatory activity in the primary visual cortex of the cat. *J. Physiol. (Lond.)* 500: 751-774.
- Bulsara A, Jacobs EW, Zhou T, Moss F, Kiss L (1991) Stochastic resonance in a single neuron model: Theory and analog simulation. *J. Theor. Biol.* 152: 531-555.
- Buracas GT, Zador AM, DeWeese MR, Albright TD (1998) Efficient discrimination of temporal patterns by motion-sensitive neurons in primate visual cortex. *Neuron* 20: 959-969.
- Carandini M, Ferster D (2000) Membrane potential and firing rate in cat primary visual cortex. *J. Neurosci.* 20: 470-484.
- Chance FS, Abbott LF, Reyes AD (2002) Gain Modulation from Background Synaptic Input. *Neuron* 35: 773-782.
- Collins JJ, Chow CC, Imhoff T (1995) Stochastic Resonance Without Tuning. *Nature* 376: 236-238.
- Collins JJ, Imhoff T, Grigg P (1996) Noise-enhanced information transmission in rat SA1 cutaneous mechanoreceptors via aperiodic stochastic resonance. *J. Neurophysiol.* 76: 642-645.
- Connors BW, Gutnick MJ (1990) Intrinsic firing patterns of diverse neocortical neurons. *TINS* 13: 99-104.
- Contreras D, Destexhe A, Steriade M (1997) Intracellular and computational characterization of the intracortical inhibitory control of synchronized thalamic inputs in vivo. *J. Neurophysiol.* 78: 335-350.

- Cover T, Thomas J (1991) Elements of Information Theory, John Wiley and Sons, New York, NY.
- Dayan P, Abbott LF (2001) Theoretical Neuroscience: Computational and Mathematical Modeling of Neural Systems. MIT Press, Cambridge.
- Dean AF, Tolhurst DJ (1983) On the distinctness of simple and complex cells in the visual cortex of the cat. *J. Physiol. (Lond.)* 344: 305-325.
- Destexhe A, Mainen ZF and Sejnowski TJ (1994) An efficient method for computing synaptic conductances based on a kinetic model of receptor binding. *Neural Comput.* 6: 14-18.
- Destexhe A, Paré D (1999) Impact of network activity on the integrative properties of neocortical pyramidal neurons in vivo. *J. Neurophysiol.* 81: 1531-1547.
- Destexhe A, Rudolph M, Fellous J-M, Sejnowski TJ (2001) Fluctuating synaptic conductances recreate in-vivo like activity in neocortical neurons. *Neuroscience* 107: 13-24.
- Destexhe A, Rudolph M, Paré D (2003) The high-conductance state of neocortical neurons. *Nat. Rev. Neurosci.* 4: 739-751.
- Diba K, Lester HA, Koch C (2004) Intrinsic Noise in Cultured Hippocampal Neurons: Experiment and Modeling *J. Neurosci.* 24: 9723-9733.
- Diesmann M, Gewaltig M-O, Aertsen A (1999) Stable propagation of synchronous spiking in cortical neural networks. *Nature*, 402: 529-533.
- Douglass JK, Wilkens LA, Pantazidou E, Moss F (1993) Stochastic resonance: Noise-enhanced information transfer in crayfish mechanoreceptors. *Nature* 365: 337-340.
- Eckhorn R, Bauer R, Jordan W, Brosch M, Kruse W, Munk M, Reiboeck HJ (1988) Coherent oscillations: A mechanism of feature linking in the visual cortex?, *Biol. Cybern.* 60: 121-130.
- Engel AK, Fries P, Singer W (2001) Dynamic Predictions: Oscillations and Synchrony in Top-Down Processing. *Nat. Rev. Neurosci.* 2: 704-716.
- Feldmeyer D, Egger V, Lübke J, Sakmann B (1999) Reliable synaptic connections between pairs of excitatory layer 4 neurones within a single *barrel* of developing rat somatosensory cortex, *J. Physiol.* 521: 169-190.
- Fellous JM, Rudolph M, Destexhe A, Sejnowski TJ (2003) Synaptic Background Noise Controls the Input/Output Characteristics of Single Cells in an *In Vitro* Model of *In Vivo* Activity. *Neuroscience* 122: 811-829.

- Fourcaud-Trocmé N, Hansel D, van Vreeswijk C, Brunel N (2003) How Spike Generation Mechanisms Determine the Neuronal Response to Fluctuating Inputs. *J. Neurosci.* 23: 11628-11640.
- Gabbiani F (1996) Coding of time-varying signals in spike trains of linear and half-wave rectifying neurons, *Network-Comput. Neural Syst.* 7:61-85.
- Gammaitoni L, Hänggi P, Jung P, Marchesoni F (1998) Stochastic resonance. *Rev. Mod. Phys.* 70: 223-287.
- Gerstein GL, Mandelbrot B (1964) Random walk models for the spike activity of a single neuron. *Biophys. J.* 71: 41-68.
- Gillespie D (1996) Exact numerical simulation of the Ornstein-Uhlenbeck process and its integral. *Phys. Rev. E* 54: 2084-2091.
- Gray CM, Singer W (1989) Stimulus-specific neuronal oscillations in orientation columns of cat visual cortex. *Proc. Natl. Acad. Sci. USA* 86: 1698-1702.
- Gray CM, McCormick DA (1996) Chattering cells - superficial pyramidal neurons contributing to the generation of synchronous oscillations in the visual cortex. *Science* 274: 109-113.
- Gutfreund Y, Yarom Y, Segev I (1995) Subthreshold oscillations and resonant frequency in guinea-pig cortical neurons: physiology and modelling. *J. Physiol.* 483.3: 621-640.
- Haag J, Borst A (1998) Active Membrane Properties and Signal Encoding in Graded Potential Neurons, *J. Neurosci.* 18: 7972-7986.
- Häusser M, Spruston N, Stuart GJ (2000) Diversity and Dynamics of Dendritic Signaling. *Science* 290: 739-744.
- Harsch A, Robinson HPC (2000) Postsynaptic Variability of Firing in Rat Cortical Neurons: The Roles of Input Synchronization and Synaptic NMDA Receptor Conductance. *J. Neurosci.* 20: 6181-6192.
- Hatsopoulos N, Joshi J, O'Leary JG (2004) Decoding Continuous and Discrete Motor Behaviors Using Motor and Premotor Cortical Ensembles. *J. Neurophysiol.* 92: 1165-1174.
- Hellwig B, Schüz A, Aertsen A (1994) Synapses on axon collaterals of pyramidal cells are spaced at random intervals: a Golgy study in the mouse cerebral cortex. *Biol. Cybern.* 71: 1-12.

- Henze DA, Buzsaki G (2001) Action potential threshold of hippocampal pyramidal cells in vivo is increased by recent spiking activity. *Neuroscience* 105: 121-130.
- Hines ML, Carnevale NT (1997) The NEURON simulation environment, *Neural Comput.* 9: 1179-1209.
- Hirsch JA, Alonso JM, Reid RC, Martinez LM (1998) Synaptic integration in striate cortical simple cells. *J. Neurosci.* 18: 9517-9528.
- Ho N, Destexhe A (2000) Synaptic Background Activity enhances the responsiveness of neocortical pyramidal neurons. *J. Neurophysiol.* 84: 1488-1496.
- Hoch T, Wenning G, Obermayer K (2003) Optimal noise-aided signal transmission through populations of neurons. *Phys. Rev. E* 68: 011911.
- Hoch T, Volgushev M, Obermayer K (2006a) Modulation of the amplitude of γ -band activity by stimulus phase enhances signal encoding. Submitted.
- Hoch T, Obermayer K (2006b) The Necessity to Use a Nonlinear Decoding Method When Estimating the Information Rate from Pooled Population Responses. Submitted.
- Hodgkin AL, Huxley AF (1952) A Quantitative Description of Membrane Current and its Application to Conduction and Excitation in Nerve. *J. Physiol.* 117: 500-544.
- Huguenard JR, Prince DA (1992) A novel T-type current underlies prolonged calcium-dependent burst firing in GABAergic neurons of rat thalamic reticular nucleus. *J. Neurosci.* 12: 3804-3817.
- Hutcheon B, Miura RM, Pail E (1996) Subthreshold membrane resonance in neocortical neurons. *J. Neurophysiol.* 76: 683-697.
- Izhikevich EM (2004) Which Model to Use for Cortical Spiking Neurons? *IEEE Trans. Neural Netw.* 15: 1063-1070.
- Jacobs RA, Jordan MI, Nowlan S, Hinton GE (1991) Adaptive mixtures of local experts, *Neural Comput.* 3: 1-12.
- Jagadeesh B, Gray CM, Ferster D (1992) Visually evoked oscillations of membrane potential in cells of cat visual cortex. *Science* 257: 552-554.
- Jahnsen H, Karnup S (1994) A spectral analysis of the integration of artificial synaptic potentials in mammalian central neurons. *Brain Research* 666: 9-20.
- Johansson RS, Birznieks I (2004) First spikes in ensembles of human tactile afferents code complex spatial fingertip events. *Nature Neurosci.* 7: 170-177.

- Kim KJ, Rieke F (2001) Temporal contrast adaptation in the input and output signals of salamander retinal ganglion cells. *J. Neurosci.* 21: 287-99.
- Koch C (1998) *Biophysics of Computation: Information Processing in Single Neurons.* Oxford University Press, Oxford.
- Krahe R, Kreiman G, Gabbiani F, Koch C, Metzner W (2002) Stimulus Encoding and Feature Extraction by Multiple Sensory Neurons. *J. Neurosci.* 22: 2374-2382.
- Kuhn A, Aertsen A, Rotter S (2003) Higher-Order Statistics of Input Ensembles and the Response of Simple Model Neurons. *Neural Comput.* 15: 67-101.
- Kuhn A, Aertsen A, Rotter S (2004) Neuronal Integration of Synaptic Input in the Fluctuation-Driven Regime. *J. Neurosci.* 24: 2345-2356.
- Lamp I, Yarom Y (1993) Subthreshold oscillations of the membrane potential: a functional synchronizing and timing device. *J. Neurophysiol.* 70: 2181-2186.
- Lamp I, Reichova I, Ferster D (1999) Synchronous membrane potential fluctuations in neurons of the cat visual cortex. *Neuron* 22: 361-374.
- Lapicque L (1907) Recherches quantitatives sur l'excitation électrique des nerfs traitée comme une polarisation. *J. Physiol. Pathol. Gen* 9: 620-635.
- Lau B, Stanley GB, Dan Y (2002) Computational subunits of visual cortical neurons revealed by artificial neural networks. *PNAS* 13: 8974-8979.
- Laughlin SB, de Ruyter van Steveninck RR, Anderson JC (1998) The metabolic cost of neural information. *Nature Neurosci.* 1: 36-41.
- Lennie P (2003) The cost of cortical computation. *Curr. Biol.* 13: 493-497.
- Levy WB, Baxter RA (1996) Energy efficient neural codes. *Neural Comput.* 8: 531-543.
- Lindner B, Schimansky-Geier L (2001) Transmission of noise coded versus additive signals through a neuronal ensemble. *Phys. Rev. Lett.* 86: 2934-2937.
- London M, Schreiber A, Hausser M, Larkum ME, Segev I (2002) The information efficacy of a synapse. *Nat. Neurosci.* 5: 332-340
- Longtin A (1993) Stochastic resonance in neuron models. *J. Stat. Phys.* 70: 309-327.
- Lübke J, Egger V, Sakmann B, Feldmeyer D (2000) Columnar organization of dendrites and axons of single and synaptically coupled neurons in layer 4 of the rat barrel cortex. *J. Neurosci.* 20: 5300-5311.

- Mainen ZF, Sejnowsky TJ (1995) Reliability of spike timing in neocortical neurons. *Science* 268: 1503-1506.
- Mainen ZF, Sejnowsky TJ (1996) Influence of dendritic structure on firing pattern in model neocortical neurons. *Nature* 382: 363-366.
- Markram H, Lübke J, Frotscher M, Roth A, Sakmann B (1997) Physiology and anatomy of synaptic connections between thick tufted pyramidal neurones in the developing rat neocortex. *J. Physiol.* 500: 409-440.
- Marquardt D (1963) An Algorithm for Least-Squares Estimation of Nonlinear Parameters. *SIAM J. Appl. Math.* 11: 431-441.
- Mazurek ME, Shadlen MN (2002) Limits to the temporal fidelity of cortical spike rate signals. *Nat. Neurosci.* 5: 463-471.
- Moss F, Ward LM, Sannita WG (2004) Stochastic resonance and sensory information processing: A tutorial and review of applications. *Clinical Neurophysiol.* 115: 267-281.
- Mukovski M, Chauvette S, Timofeev I, Volgushev M (2006) Detection of active and silent states in neocortical neurons from the field potential signal during slow wave sleep. *Cerebr. Cortex*, in press.
- Naundorf B, Geisel T, Wolf F (2005) Action Potential Onset Dynamics and the Response Speed of Neuronal Populations. *J. Comput. Neurosci.* 18: 297-309.
- Naundorf B, Wolf F, Volgushev M (2006) Unique features of action potential initiation in cortical neurons. *Nature* 440: 1060-1063.
- Nicolis C (1982) Stochastic aspects of climatic transitions - response to a periodic forcing. *Tellus* 34: 1-9.
- Nowak LG, Sanchez-Vives MV, McCormick DA (1997) Influence of low and high frequency inputs on spike timing in visual cortical neurons. *Cerebr. Cortex* 7: 487-501.
- Olshausen BA, Field DJ (2005) How close are we to understand V1?. *Neural Comput.* 17: 1665-1699.
- Panzeri S, Petroni F, Petersen RS, Diamond ME (2003) Decoding Neuronal Population Activity in Rat Somatosensory Cortex: Role of Columnar Organization. *Cerebral Cortex* 13: 45-52.
- Paré D, Shink E, Gaudreau H, Destexhe A, Lang EJ (1998) Impact of Spontaneous Synaptic Activity on the Resting Properties of Cat Neocortical Pyramidal Neurons In Vivo. *J. Neurophysiol.* 79: 1450-1460.

- de Polavieja GG (2002) Errors drive the evolution of biological signalling to costly codes. *J. Theor. Biol.* 214: 657-664.
- Papoulis A (1991) *Probability, Random Variables and Stochastic Processes*. McGraw-Hill, New York.
- Polsky A, Mel BW, Schiller J (2004) Computational subunits in thin dendrites of pyramidal cells. *Nat. Neurosci.* 7: 621-627.
- Pouget A, Dayan P, Zemel R (2000) Information processing with population codes. *Nat. Rev. Neurosci.* 1: 125-132.
- Rauch A, La Camera G, Luscher HR, Senn W, Fusi S (2003) Neocortical pyramidal cells respond as integrate-and-fire neurons to in vivo-like input currents. *J. Neurophysiol.* 90:1598-1612.
- Reich DS, Mechler F, Victor JD (2001) Temporal coding of contrast in primary visual cortex: when, what, and why? *J. Neurophysiol.* 85: 1039-1050.
- Reinagel P, Reid C (2000) Temporal Coding of Visual Information in the Thalamus. *J. Neurosci.* 20: 5392-5400.
- Reyes AD (2001) Influence of dendritic conductances on the input-output properties of neurons. *Ann. Rev. Neurosci.* 24: 653-675.
- Ricciardi LM (1977) *Diffusion Processes and Related Topics in Biology*. Lecture Notes in Biomathematics 14. Springer-Verlag, Berlin.
- Richardson M, Gerstner W (2005) Synaptic shot noise and conductance fluctuations affect the membrane voltage with equal significance. *Neural Comput.* 17: 923-947.
- Rieke F, Warland D, de Ruyter van Steveninck RR, Bialek W (1997) *Spikes: Exploring the Neural Code*. MIT Press, Cambridge.
- Rudolph M, Destexhe A (2001) Do neocortical pyramidal neurons display stochastic resonance? *J. Comput. Neurosci.* 11: 19-42.
- Russell DF, Wilkens LA, Moss F (1999) Use of behavioural stochastic resonance by paddle fish for feeding. *Nature* 402: 291-294.
- Salinas E, Sejnowski TJ (2000) Impact of correlated synaptic input on output firing rate and variability in simple neuronal models. *J. Neurosci.* 20: 6193-6209.
- Silberberg G, Bethge M, Markram H, Pawelzik K, Tsodyks M (2004) Dynamics of population rate codes in ensembles of neocortical neurons. *J. Neurophysiol.* 91: 704-709.

- Simoncelli EP, Olshausen BA (2001) Natural Image Statistics and Neural Representation. *Annu. Rev. Neurosci.* 24: 1193-1216.
- Simonotto E, Riani M, Seife C, Roberts M, Twitty J, Moss F (1997) Visual perception of stochastic resonance. *Phys. Rev. Lett.* 78: 1186-1189.
- Singer W (1993) Synchronization of cortical activity and its putative role in information processing and learning. *Annu. Rev. Psychol.* 55: 349-374.
- Singer W (1999) Neuronal synchrony: A versatile code for the definition of relations? *Neuron* 24: 49-65.
- Shadlen MN, Britten KH, Newsome WT, Movshon JA (1996) A computational analysis of the relationship between neuronal and behavioral responses to visual motion. *J. Neurosci.* 16: 1486-1510.
- Shadlen MN, Newsome WT (1998) The Variable Discharge of Cortical Neurons: Implications for Connectivity, Computation, and Information Coding. *J. Neurosci.* 18: 3870-3896.
- Skottun BC, Valois RL, Groszfeld DH, Movshon JA, Albrecht DG, Bonds AB (1991) Classifying simple and complex cells on the basis of response modulation. *Vision Res.* 31: 1079-1086.
- Softky WR, Koch C (1993) The highly irregular firing of cortical cells is inconsistent with temporal integration of random EPSPs. *J. Neurosci.* 13: 334-350.
- Stacey WC, Durand DM (2001) Synaptic noise improves detection of subthreshold signals in hippocampal CA1 neurons. *J. Neurophysiol.* 86: 1104-1112.
- Stein RB (1965) A Theoretical Analysis of Neuronal Variability. *Biophys. J.* 91: 173-194.
- Stein RB, Gossen ER, Jones KE (2005) Neuronal Variability: Noise or part of the Signal? *Nat. Rev. Neurosci.* 6: 389-397.
- Steinmetz PN, Roy A, Fitzgerald PJ, Hsiao SS, Johnson KO, Niebur E (2000) Attention modulates synchronized neuronal firing in primate somatosensory cortex. *Nature* 404: 131-133.
- Steriade M, Contreras D, Amzica F, Timofeev I (1996) Synchronization of fast (30-40 Hz) spontaneous oscillations in intrathalamic and thalamocortical networks. *J. Neurosci.* 16: 2788-2808.
- Steriade M (2001) Impact of Network Activities on Neuronal Properties in Corticothalamic Systems. *J. Neurophysiol.* 86: 1-39.

- Steriade M, Timofeev I, Grenier F (2001) Natural waking and sleep states: A view from inside neocortical neurons. *J. Neurophysiol.* 85: 1969-1985.
- Stevens CF, Zador AM (1998) Input synchrony and the irregular firing in cortical neurons. *Nat. Neurosci.* 1: 210-216.
- Strong SP, Koberle R, de Ruyter van Steveninck RR, Bialek W (1998) Entropy and Information in Neural Spike Trains. *Phys. Rev. Lett.* 80: 197-200.
- Tarczy-Hornoch K, Martin KAC, Jack JJB, Stratford KJ (1998) Synaptic interactions between smooth and spiny neurons in layer 4 of cat visual cortex in vitro. *J. Physiol.* 508: 351-363.
- Tougaard J (2000) Stochastic resonance and signal detection in an energy detector - implications for biological receptor systems. *Biol. Cybern.* 83: 471-480.
- Tsodyks M, Sejnowski T (1995) Rapid switching in balanced cortical network models. *Network: Comput. Neural Syst.* 6: 111-124.
- Tuckwell HC (1988) Introduction to theoretical neurobiology: Vol. 2. Cambridge University Press, Cambridge.
- Usrey WM, Reid RC (1999) Synchronous Activity in the Visual System. *Ann. Rev. Physiol.* 61: 435-456.
- Volgushev M, Chistiakova M, Singer W (1998) Modification of discharge patterns of neo-cortical neurons by induced oscillations of the membrane potential. *Neuroscience* 83: 15-25.
- Volgushev M, Eysel UT (2000) Noise makes sense in neuronal computing. *Science* 290: 1908-1909.
- Volgushev M, Pernberg J, Eysel UT (2000) Comparison of the selectivity of postsynaptic potentials and spike responses in cat visual cortex, *Europ. J. Neurosci.* 12: 257-263.
- Volgushev M, Pernberg J, Eysel UT (2002) A novel mechanism of response selectivity of neurons in cat visual cortex. *J. Physiol. (Lond.)* 540.1: 307-320.
- Volgushev M, Pernberg J, Eysel UT (2003) γ -Frequency fluctuations of the membrane potential and response selectivity in visual cortical neurons, *Europ. J. Neurosci.* 17: 1768-1776.
- Volgushev M, Pernberg J, Eysel UT (2004) Response selectivity and gamma-frequency fluctuations of the membrane potential in visual cortical neurons. *Neurocomputing* 58-60: 957-963.

- Wang XJ, Buzsaki G (1996) Gamma oscillation by synaptic inhibition in a hippocampal interneuronal network model. *J. Neurosci.* 16: 6402-6413.
- Warland DK, Reinagel P, Meister M (1997) Decoding visual information from a population of retinal ganglion cells. *J. Neurophysiol.* 78: 2336-2350.
- Wenning G, Obermayer K (2003) Activity driven adaptive stochastic resonance. *Phys. Rev. Lett.* 90:120602.
- Wenning G, Hoch T, Obermayer K (2005) Detection of pulses in a colored noise setting. *Phys. Rev. E* 71: 021902.
- White JA, Rubinstein JT, Kay AR (2000) Channel noise in neurons. *Trends Neurosci.* 23: 131-137.
- Wiesenfeld K, Moss F (1995) Stochastic resonance and the benefits of noise: from ice ages to crayfish and SQUIDS. *Nature* 373: 33-36.
- Wilson HR (1999) Simplified Dynamics of Human and Mammalian Neocortical Neurons. *J. Theor. Biol.* 200: 375-388.
- Zohary E, Shadlen MN, Newsome WT (1994) Correlated neuronal discharge rate and its implications for psychophysical performance. *Nature* 370: 140-143.